Doctoral Dissertation

Transformation Mechanism of Pb/Sn Perovskites and Exploration of Bi/Sb-Based Semiconductors as an Alternative

(Pb/Sn ペロブスカイトの変性機構の解明と
代替材料としての Bi/Sb 系半導体の探索)

Ryosuke Nishikubo

January 2021

Department of Applied Chemistry,
Graduate School of Engineering,
Osaka University

Preface

The studies presented in this dissertation were carried out under the supervision of Prof. Dr. Akinori Saeki at Department of Applied Chemistry, Graduate School of Engineering, Osaka University.

The contents of this dissertation provide the insight into the transformation mechanism of lead and tin halide perovskites with air exposure and the specific thermoresponsive emission behavior, and the fundamental optoelectronic properties and device characteristics of bismuth and antimony-based semiconducting materials for a substitution of halide perovskites. The author hopes these findings will contribute to the development of lead/tin halide perovskites and bismuth/antimony-based semiconductors for optical and optoelectronic applications.

Ryosuke Nishikubo

Department of Applied Chemistry
Graduate School of Engineering
Osaka University, Japan
January 2021

Contents

Chapter 1: General Introduction

The development of renewable energy production system as an alternative to fossil fuels is one of the most important tasks for future human lives. Although a large part of global electricity supply is dependent on fossil fuels, these resources is going on depletion along with the environment destroy. In this viewpoint, the use of solar energy with photovoltaic (PV) cells is expectable. The literature shows the great potential of PV, where calculated annual solar energy potential is 1575–49837 exa Joules, 2.6–82 fold larger than the global energy consumption in 2015.[1,2] With the demand for renewable energy resources, PV technologies are widely developed, and expected to occupy 30% of energy supply in 2100 (Figure 1-1).[1] In fact, conventional crystalline silicon PV achieves power conversion efficiencies more than 20% and 26% in the commercial and lab scale, respectively.[3] Meanwhile, their high energy production cost and the inconveniences due to their rigid and heavy property retards the growth of PV electricity supply. To breakout this issue, the development of thin film PV produced by inexpensive ways such as solution process is needed. In terms of stability, inorganic or organic/inorganic hybrid devices appear to be promising. In this chapter, the recent progress, principle, and underlying problems of hybrid thin film solar cells are reviewed.

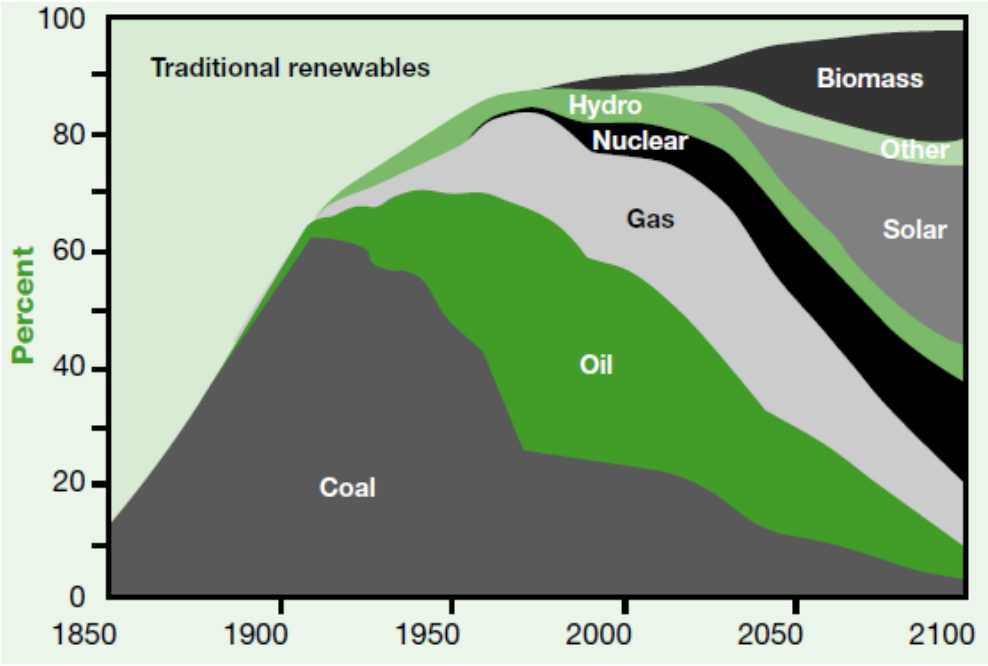

Figure 1-1. One of future scenario of global energy supply reported in World Energy Assessment.[1]

1-1. Hybrid thin film solar cells

Organic/inorganic hybrid thin film solar cells (HSCs) have shown much interest owing to their rapid growth of power conversion efficiency (PCE). The beginning point of HSCs development turns back to the reports of the first organic solar cells demonstrated by C. W. Tang (1%, in 1986)[4] and the outperforming dye-sensitized solar cell (DSSC) demonstrated by M. Grätzel, *et al.* (7.9%, in 1991)[5]. Thereafter, the use of inorganic quantum dots (QDs) as a sensitizer allowed to convert DSSC using electrolyte into all solid HSCs. Conjugated molecules were used instead of an electrolyte to extract photogenerated holes.[6] In 2009, T. Miyasaka, *et al.* firstly reported lead halide perovskite (LHP)-based DSSC with the PCE of 3.8%.[7] Afterward, Park, *et al.* succeeded to fabricate an all solid perovskite solar cell, significantly promoted further investigation of perovskite solar cells.[8] In 2020, HSCs such as perovskite solar cells and QDs (PbS) solar cells achieved exceptionally high PCE over 25% and 11.5%, respectively (Figure 1-2.).[3,9]

Although all inorganic and organic PVs are also notable, HSCs have some superior points. Because solution process is available in the production, HSCs is expected to be less expensive than inorganic PVs. As for air stability, organic PVs suffer from oxidation, which significantly quenches the photogenerated exciton.[10] Whereas in HSCs, organic materials such as conjugated polymers are mostly used to extract holes from light absorbing layer, where oxidation induces *p*-type doping increasing hole mobility.[11–13] These properties further enhance the possibility of HSCs (especially perovskite) as next generation solar cells.

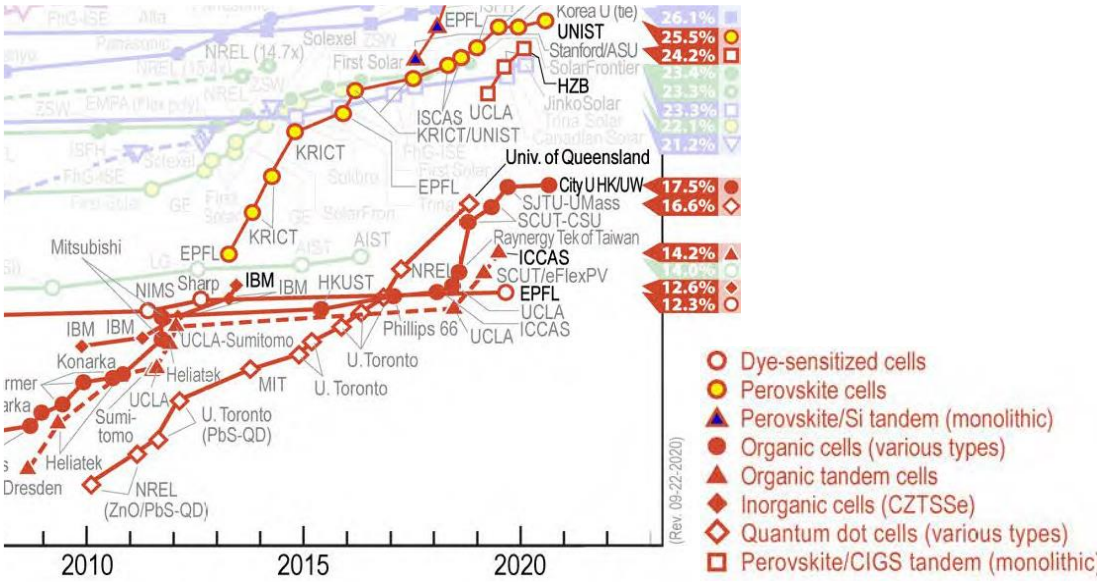

Figure 1-2. Recent progress of emerging thin film solar cells.[3]

1-2. Fundamental of solar cells

1-2-1. Photoelectric conversion principle

The *n-i-p* structure is the most common architecture of HSCs (Figure 1-3a),[14–18] in which a light absorber (*i* layer) is sandwiched by electron transport material (ETM; *n* layer) and hole transport material (HTM; *p* layer), with electrodes as bottom and top electric contact layer. A transparent electrode, located at the bottom, such as indium tin oxide (ITO) and fluorine-doped tin oxide (FTO) is used to introduce light into a device. Upon the light irradiation, electrons are excited in the *i* layer to form excitons. When inorganic material or hybrid perovskite is used as the *i* layer, the excitons immediately separate into free electrons and holes at room temperature.[19,20] The free electrons and holes are transported to ETM and HTM respectively, and then captured by the electrodes. For an efficient electron transfer to ETM, the conduction band minimum (CBM) of the *i* layer should be shallower than that of ETM (Figure 1-3b). Mesoporous ETM such as TiO_2 (mp-TiO_2) is commonly used in regular cells to enhance electron extraction.[21–23] Of course, the valence band maxima (VBM) of *i* layer should be deeper than that of HTM for proper hole extraction.

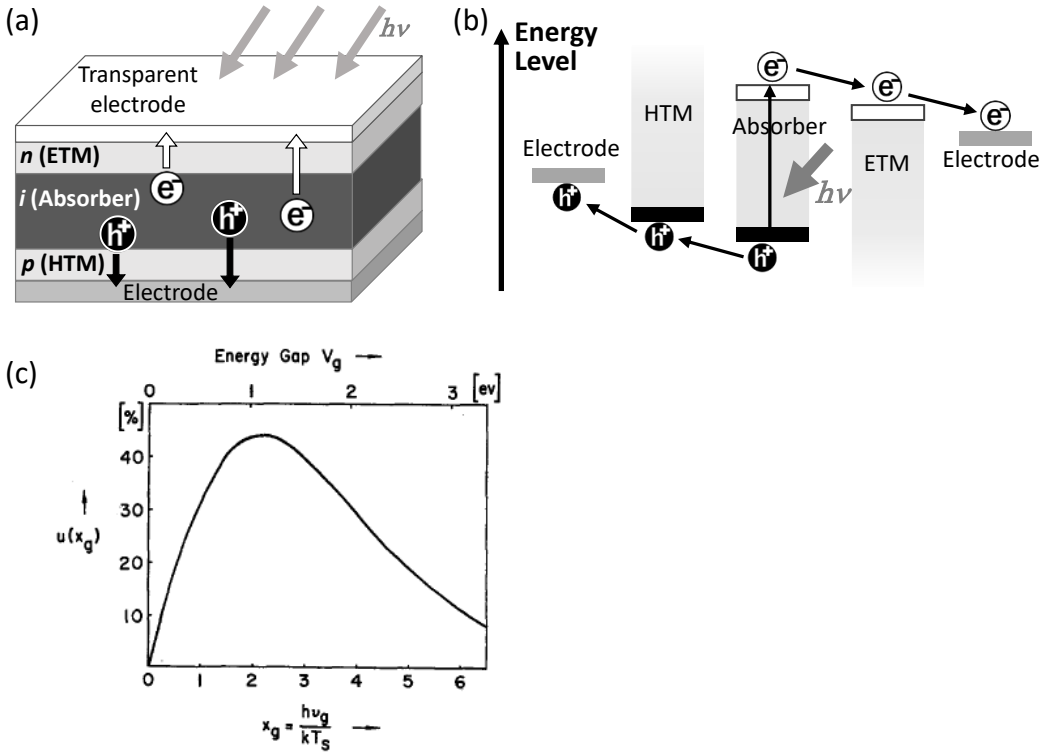

Figure 1-3. (a) Schematic image of the structure of *n-i-p* thin film solar cell. (b) Energy diagram of *n-i-p* solar cells. (c) Shockley-Queisser limit for the PCE of a solar cell obtained from approximated solar spectrum.[24]

The selection of light absorber with optimal bandgap is of critical importance in development of efficient solar cells. Because the photoelectric output power is the product of current and voltage, where these are in a trade-off relation in terms of bandgap, the moderate bandgap is required. According to Schockley-Queisser limit, 1.34 eV of bandgap is the most optimal under AM1.5G[24] (Figure 1-3c). Other important factors such as charge separation are mentioned later.

1-2-2. How to evaluate solar cells

Current-voltage (*JV*) characteristics of a solar cell is evaluated by plotting the measured current density under the pseudo sunlight (AM1.5G) as a function of applied voltage. Digital multi meter is used to measure the electrical output from a solar cell along with scanning the value of applied voltage. When the bias is scanned from a low to high voltage, it is called as forward scan. On the other hand, the bias scan from high to low voltage is called as reverse scan. The *JV* curve as represented in Figure 1-4a is obtained after the scanning. The performance parameters found from the *JV* curve are the short circuit current (J_{SC}), open circuit voltage (V_{OC}), and fill factor (FF), where J_{SC} and V_{OC} are the current density and voltage at 0 output obtained from the crossing points of *JV* curve and the two axes, FF is the maximum output power ($J_{Max} \times V_{Max}$) divided by $J_{SC} \times V_{OC}$. The details of each parameter will be discussed in the following section. The power conversion efficiency (PCE) is obtained as the product of these parameters (PCE = $J_{Max} \times V_{Max} = J_{SC} \times V_{OC} \times$ FF).

The *JV* curve is rationally represented via following Shockley diode equation:

$$J_d = J_0\{\exp\left(\frac{eV_d}{nkT}\right) - 1\} \qquad (1\text{-}1)$$

$$J = J_{SC} - V_d/R_{sh} - J_d \qquad (1\text{-}2)$$

$$V = V_d + JR_S \qquad (1\text{-}3)$$

, where J_0 is the saturation current, e is the elemental charge, J_d and V_d are the current density and voltage across the diode, n is the ideal factor, k is Boltzmann constant, T is temperature, R_{sh} and R_s are the shunt and series resistance of device, as represented in Figure 1-4b. R_{sh} and R_s are also approximately calculated as $(-dJ/dV)^{-1}$ at $V = 0$ and V_{OC}, respectively. The fitting parameters n, R_{sh}, and R_s are of use in the detailed discussion of *JV* characteristics along with J_{SC}, V_{OC}, and FF.

The external quantum efficiency (EQE) spectra is also obtained from solar cells by plotting the current density as a function of irradiated light wavelength. The integration of current density with respect to the wavelength generally coincides with the J_{SC} obtained in *JV* measurement.

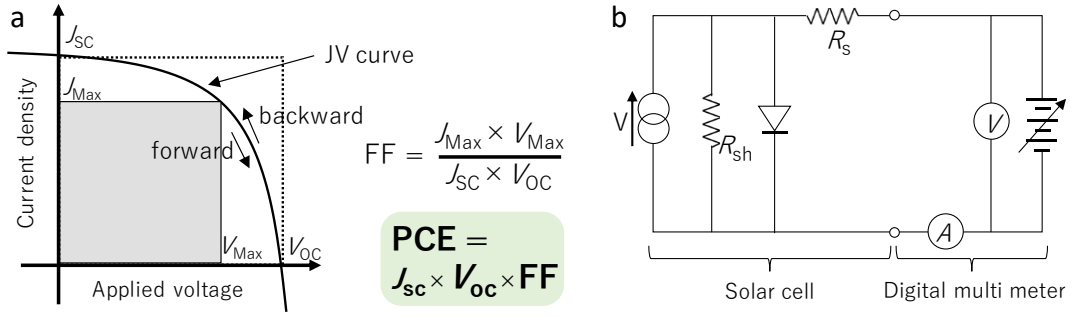

Figure 1-4. (a) Schematic image of *JV* curve and calculation of PCE. (b) Equivalent circuit of the measurement system of solar cells.

1-2-3. Physical meaning of the parameters

Here, the physical sense of *JV* characteristic parameters, J_{SC}, V_{OC}, FF, R_{sh}, R_s, and n are discussed. J_{SC} is basically represented as the product of absorbed photon density, charge separation efficiency, and charge extraction efficiency. Thus, narrow bandgap and high absorption coefficient affords a high J_{SC} value. For an efficient charge separation, quantum confined structure is not preferred. For an efficient charge extraction, a long charge diffusion length and smooth interfacial charge transport is required. V_{OC} is determined by the bandgap of absorber and the energy losses, which are attributed to bulk and interfacial recombination. To distinguish the bulk and interfacial effect, temperature-dependent V_{OC} measurement could be one of ways.[25,26] FF is directly affected by R_{sh} and R_s, where both increment of R_{sh} value and decrement of R_s value enhance FF. The small R_{sh} represents high recombination rate or existence of leak current due to poor coverage of certain layer in PV device,[27,28] meanwhile the large R_s represents the high resistance for photogenerated electrons and holes. Low charge mobility and high interfacial resistance induce the increase of R_s.[27,29] n (ideal factor) value, usually between 1 and 2, is related with charge recombination mode. n = 1 indicates a band-to-band recombination dominated mode, whereas n = 2 indicates a gap state assisted recombination dominated mode.[28]

1-3. Lead Halide Perovskites (LHPs)

1-3-1. Photovoltaic performance of LHPs

LHPs consisting of A-site cation (Cs^+, $CH_3NH_3^+$ (MA^+), and $HC(NH_2)^+$ (FA^+)), B-site metal (Pb), and X-site halogen (I, Br, and Cl) (Figure 1-5a) have almost ideal physical characters, such as large absorption coefficient throughout visible region,[30] low exciton binding energy,[31] high electron and hole mobilities,[32,33] and polaron formation preventing recombination.[34] The PCE of perovskite solar cells have been dramatically increased from 3.8% in 2009 (first report by T. Miyasaka, *et al.*) to 25.5% in 2020, near to the best PCE of single crystalline Si solar cells.[3,7] In addition, their production cost is expected much lower than those of crystalline Si solar cells owing to the solution process. LHP thin films are fabricated by facial spin-coating of the precursor solution including AX and PbX_2, followed by thermal annealing. Besides, the high emission property of Br-exchanged perovskite such as methylammonium lead bromide ($MAPbBr_3$) is beneficial in photonic applications such as laser and light emitting diode (LED).[35,36]

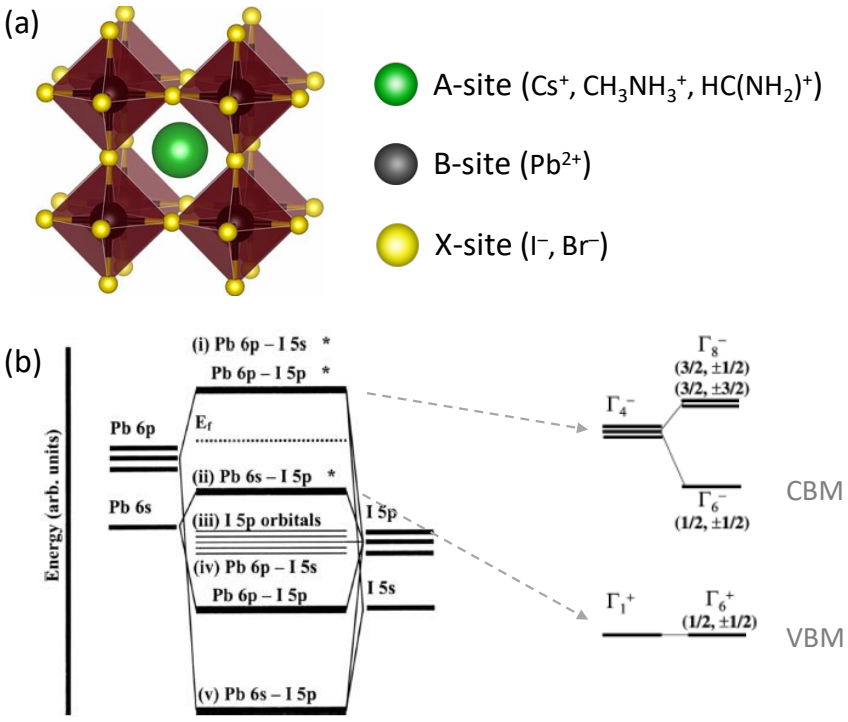

Figure 1-5. (a) The image of crystal structure of ABX_3 LHPs, and (b) the electronic structure of $MAPbI_3$

The outstanding performance of perovskite solar cells is originated from their electronic structure. As shown in Figure 1-5b, the CBM of $MAPbI_3$ is the hybrid of Pb 6p, I 5s, and I 5p, whereas the VBM is consists of Pb 6s and I 5p.[37–39] This configuration affords spherically symmetric wave function of CBM and VBM with the inverted parity each other, resulting in isotropic charge transfer and strong absorption. Furthermore, the anti-bonding nature of VBM inhibits the generation of deep defect level inside the gap.[40] This is a notable superiority of LHPs to inorganic QDs, considering their intrinsically numerous surface defect due to a huge surface area.

1-3-2. Stability and toxicity of LHPs

The stability of LHPs in humid condition is much lower than typical inorganic semiconductors such as Si. LHPs easily adsorb H_2O molecules, and dissociate into PbI_2 and AI (A = Cs, MA, FA) or transform into the complex of LHPs and water.[41–43] The degradation can be detected by the changing in the thin film color into PbI_2-originated yellow color appeared after air exposure (Figure 1-6). Their thermal stability is also in concern.[44,45] Organic components in LHPs such as MA and FA gradually sublimate or dissociate into other molecules at high temperature. Thus, the long-term stability of LHPs remains a matter of ongoing investigation.

The high toxicity of LHPs along with their high solubility in water is also seriously concerned.[46] It is not only environmental but also economic disadvantage, requiring proper regulation throughout their product life. In Europe, the use of lead in electronic devices are strictly limited by RoHS compliant. The rules to limit harmful materials appear to become further rigorous. In this viewpoint, the development of Pb-free perovskites or analogous semiconductors has great potential to make a leap in the production of ideal solar cell.

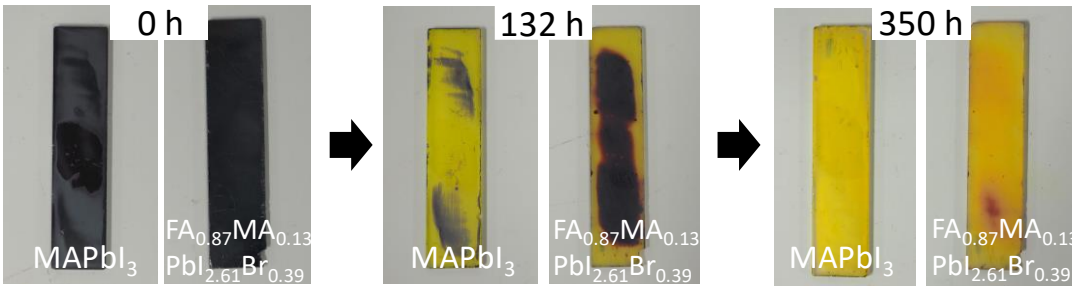

Figure 1-6. The pictures of LHP thin films with air exposure time.

1-3-3. Tin halide perovskites (THPs)

THPs have been emerged as environmental friendly Pb-free perovskites.[47–49] They have a relatively narrow bandgap compared to LHPs, close to the Shockley-Queisser optimal bandgap.[50] Theoretical calculation implies that hole effective masses in THPs is intrinsically smaller than those of LHPs.[51] However, Sn^{2+} ions in THPs suffers from significant oxidation to yield Sn^{4+}, forming a deep electron trap level.[52–57] The instability of Sn^{2+} ion is intrinsically originated from the lack in inert pair electron effect. Due to the weak stabilization of the $5s^2$ unshared electron pair in Sn(II), the electron pair is easily lost, yielding Sn(IV). The contamination of oxidized species is considered to occur throughout the all processes including row material production, device fabrication, and device evaluation. The dark carrier density of THPs (10^{17}–10^{19} cm^{-3}) inherently doped by conversion from Sn^{2+} to Sn^{4+} is many orders of magnitude higher than that of $MAPbI_3$ (10^{9}–10^{11} cm^{-3}),[58,59] which causes charge recombination, shorting of the diode circuit, and deterioration of the open-circuit voltage.[60–62] Due to these natures, the reported best PCE of THP solar cell (~13%, in 2020) is much lower than that of LHP,[63] even be measured in N_2 atmosphere.

1-4. Bi- and Sb-based semiconducting materials

1-4-1. Various Bi- and Sb-based materials

Another choice for Pb-free solar cells is the use of bismuth (Bi) and antimony (Sb) instead of Sn.[64–68] The electronic configurations of Bi^{3+} and Sb^{3+} ion of $6s^26p^0$ and $5s^25p^0$, which are analogous to those of Pb^{2+} and Sn^{2+}, would yield similar optoelectronic characters with LHPs such as high absorption coefficient, high charge mobility, and inhibited defect level. The heavy atom effect, which promotes efficient absorption,[66] is also expected. In addition, elementally abundant, non-toxic Bi and Sb are advantageous over commercialized inorganic solar cells[69] such as CdTe[70] and CIGS (Cu-In-Ga-S/Se)[71], as well as emerging LHP solar cells.[3]

Meanwhile, unlike Sn, 3-valent cationic nature of Bi and Sb disenable the straightforward substitution of Pb^{2+} ion in LHPs. Thus, alternative crystal structures instead of ABX_3 need to be explored. The representative structures of Bi- and Sb-based semiconducting materials are summarized in Figure 1-7. $A_3B_2X_9$ (A = Cs[72] MA,[72] FA,[73] B = Bi,[72] Sb,[74,75] X = I,[72] Br[76]) type materials with 0-dimensional dimeric or 2-dimensional layered structure are widely studied (Figure 1-7a). These are easily fabricated through the simple spin-coating of the solution of AX and BX_3 dissolved in dimethyl sulfoxide (DMSO) or dimethyl formamide (DMF). The silver-bismuth-iodide $Ag_xBi_{(1-x)}I_{(3-2x)}$ with cubic and layered structures (Figure 1-7b),[77–79] where the structure type (cubic or layered) is controlled by Ag:Bi ratio and the 3-dimensional double perovskite (DP), where Ag and Bi are alternately locating in B-site (Figure 1-7c)[80–82] have been also emerged as solution-processable Bi and Sb halide semiconductors.

Besides, chalcogenides such as Bi_2Te_3, Bi_2S_3, Sb_2S_3, $AgBiS_2$ and $CuBi(Sb)S_2$ are known as typical semiconducting materials (Figure 1-7d).[83–90] Photodetectors using Bi_2Te_3[87-89] show notable photosensitivity, and Bi_2S_3 including elementally-abundant sulfur instead of tellurium is used as the photoabsorber of QDs solar cell with the PCE of 0.46%. Sb_2S_3 have been widely studied owing to their particularly high PCE (~7.5%).[90] The chalcohalides including both chalcogen and halogen such as SbSeI and $MASbSI_2$ are also notable candidates (Figure 1-7e, f).[91,92] For instance, Nie *et al.* reported a PCE of over 3% for $MASbSI_2$ and SbSI solar cell.[92,93] Quantum chemical calculation predicted the light effective masses of the hole and electron in $MASbSI_2$.[94] The reported PCEs of solar cells using these materials are summarized in Table 1-1. The PCEs are varying from 0.012% to 7.1% depending on the active layer.

The confusing matter is the way to select the plausible one from these numerous candidates without any overlooking. The device evaluation definitely includes the contact

issues at the semiconductor/electrode interfaces, precluding the direct observation of charge carrier dynamics. For proper material exploration, it is essential to investigate materials from viewpoints of their fundamental optoelectronic properties such as energy level of VBM and CBM, charge diffusion, and interfacial transport property.

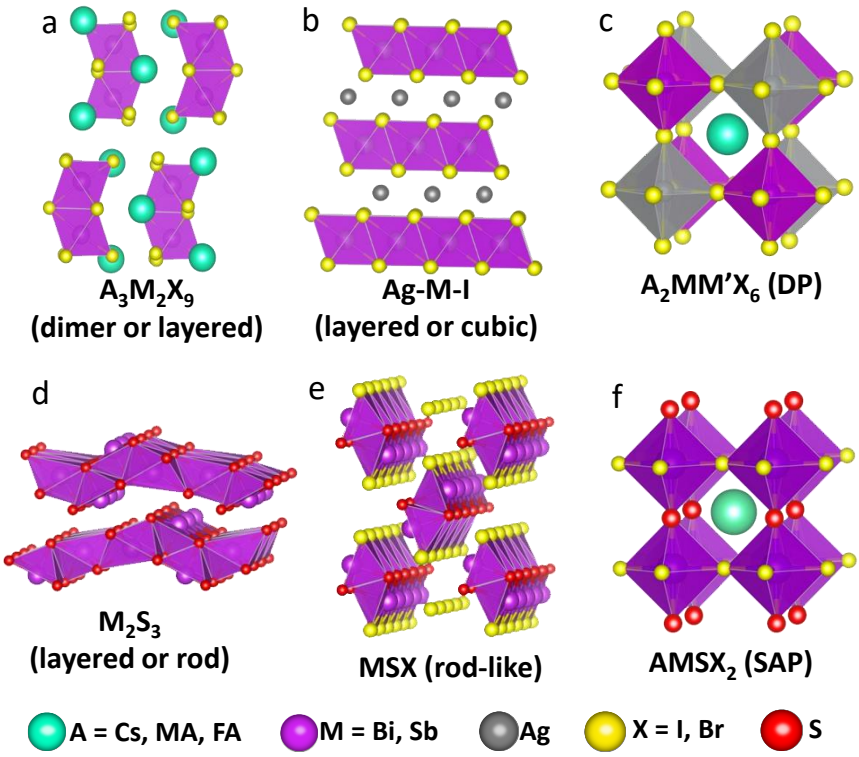

Figure 1-7. Crystal structures of Bi- and Sb-based solar absorbers: (a) $A_3M_2X_9$ (dimer or layered), (b) $Ag_xBi_{(1-x)}I_{(3-2x)}$ (layered or rod), (c) $A_2MM'X_6$ (double perovskite: DP), (d) M_2S_3 (layered), (e) MSX (rod-like), and (f) $AMSX_2$ (split anion perovskite: SAP).

Table 1-1. Summary of reported PCEs or the solar cells using Bi- and Sb-based materials.

absorber	device structure	PCE (%)	Ref
$Cs_3Bi_2I_9$	FTO/cTiO_2/mpTiO_2/$Cs_3Bi_2I_9$/Spiro-OMeTAD/Au	1.09	72
$MA_3Bi_2I_9$	FTO/cTiO_2/mpTiO_2/$MA_3Bi_2I_9$/Polyindenofluoren-8-triarylamine/Au	0.71	95
BiOI	FTO/TiO_2/BiOI (photoanode), Pt/FTO (cathode), I_3^-/I^- (redox electrolyte)	1.03	96
BiSI	FTO/BiSI/CuSCN/Pt,FTO	0.012	97
Bi_2S_3	ITO/Bi_2S_3/P3HT/Ag	0.46	98
AgI,BiI_3	FTO/TiO_2/AgI,BiI_3(AgI:BiI_3=2:1)/P3HT/Au	2.1	78
$AgBiI_4$	ITO/SnO_2/$AgBiI_4$/PTAA/Au	2.8	99
$Cs_2AgBiBr_6$	FTO/cTiO_2/mpTiO_2/$Cs_2AgBiBr_6$/PTAA/Au	1.26	100
$AgBiS_2$	ITO/ZnO/$AgBiS_2$ QDs/PTB7/MoO_X/Ag	6.3	101
$Cs_3Sb_2I_9$	ITO/PEDOT:PSS/$Cs_3Sb_2I_9$/PCBM/C60,BCP/Au	0.84	74
$MA_3Sb_2I_9$	ITO/PEDOT:PSS/$MA_3Sb_2I_9$/PCBM/C60,BCP/Au	2.04	74
SbSI	FTO/cTiO_2/mpTiO_2/SbSI/PCPDTBT/PEDOT:PSS/Au	3.05	93
Sb_2S_3	FTO/cTiO_2/mpTiO_2/Sb_2S_3/Spiro-OMeTAD/Au	7.5	90
$MASbSI_2$	FTO/cTiO_2/mpTiO_2/$MASbSI_2$/PCPDTBT/PEDOT:PSS/Au	3.08	92

1-4-2. Thin film preparation process

On one hand, halide materials such as $A_3B_2X_9$, AgBiI, and $A_2BB'X_6$ are prepared by facial spin-coating of precursor solution and subsequent thermal annealing. On the other hand, such a simple process is not applicable for the preparation of chalcogenide and chalcohalide thin films due to their limited solubility in organic solvent. The typical deposition processes of chalcogenide thin films are chemical bath deposition (CBD),[102] nanoparticles (NP) deposition,[98,101] successive-ionic-layer-adsorption-reaction (SILAR),[96,103] and spray pyrolysis (SP)[104]. The CBD is a way to gradually deposit metal chalcogenide film onto the substrate through the reaction of metal cation and chalcogen anion (Figure 1-8a). The repeated spin-coating of colloidal NPs suspension, followed by ligand exchange is a typical NPs deposition way (Figure 1-8b). In the successive-ionic-layer-adsorption-reaction (SILAR), thin films are made by immersing a substrate into the solution of metal cation and chalcogen anion alternately (Figure 1-8c). The SP is conducted by spraying precursor solution including metal and sulfur source onto a heated substrate to induce thermal decomposition (Figure 1-8d). These methods mostly afford smooth films, though with relatively small grain size compared to those of LHPs (0.5~1 μm). The small grain size is detrimental to charge separation and transport, due to the strong confinement effect and the formation of extensive grain boundaries. Furthermore, recent studies exploited facile methods consisting of the spin-coating of precursor solution including metal and sulfur source, followed by thermal decomposition (Figure 1-8e). Metal-salts/thiourea complex and metal-ethylxanthate were mostly used as the precursors.[84,105,106] In Bi_2S_3 film preparation, the use of metal-ethylxanthate yields large grain size of ~0.5μm, comparable to those of LHPs.[105] The remaining issues to be overcame are generation of film roughness with numerous pin-holes.[105,106]

The preparation methods of chalcohalide films were recently reported. Sfaelou, *et al.* demonstrated the preparation of BiOI thin film by the SILAR method.[95] Nie, *et al.* reported that 2-step fabrication of SbSI consisting of Sb_2S_3 deposition by CBD and following repeated spin-coating of SbI_3 solution followed by thermal annealing afforded improvement of PCE up to 3% (Figure 1-8f).[93] Meanwhile, Hahn, *et al.* successfully prepared a BiSI film by facile 1-step method including the spin-coating of precursor solution containing $Bi(NO_3)$, NH_4I, and thiourea, followed by thermal decomposition.[97] The development of 1-step preparation method for outperforming Sb-based chalcohalides is definitely one of the ways to improve lead free solar cells.

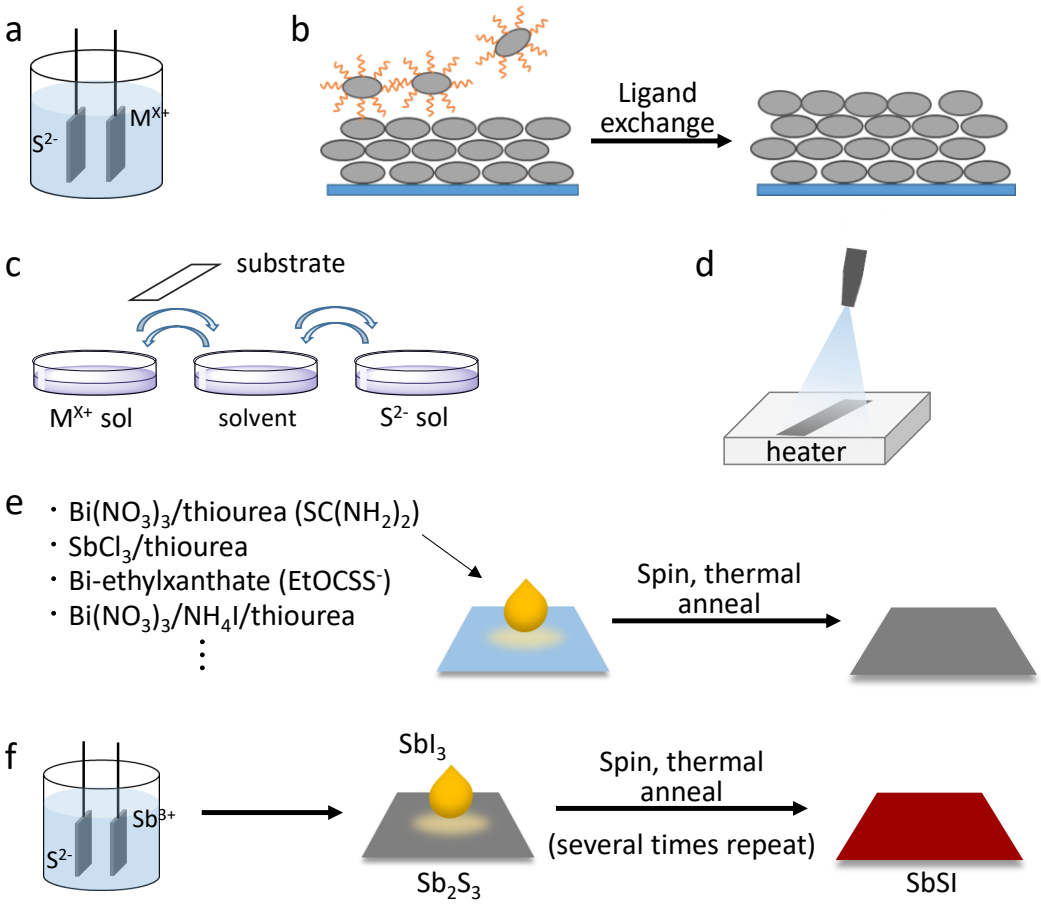

Figure 1-8. The schematics of Bi and Sb chalcogenide and chalcohalide thin film preparation methods; (a) CBD, (b) NPs deposition, (c) SILAR, (d) spray pyrolysis, (e) thermal decomposition of precursor, and (f) 2-step coating method of SbSI via CBD and SbI_3 spin-coating.[93]

1-5. Time-Resolved Microwave Conductivity (TRMC)

Existence of the contact issue makes the direct observation of charge carrier dynamics such as mobility, lifetime, and charge transport to adjacent layer quite unreliable in device evaluation. Thus, contact-free measuring technique is desired. Time-resolved microwave conductivity (TRMC) measurement is a powerful way to measure transient conductivity ($\Delta\sigma$) upon pulse light irradiation because detection by microwave in TRMC can exclude undesired contact resistance and capacitance. Also, the use of alternated electric field induces local vibration of charge carriers. This enables intrinsic evaluation of charge carrier dynamics suppressing the trapping effect, which mostly appears in contacted measurement.

In the measurement, film samples deposited on a quartz substrate or powder attached on quartz with tape are set in a resonant cavity to irradiate microwave and pulsed light. Under the resonant state, $\Delta\sigma$ is obtained via following equation:

$$\Delta\sigma = \frac{1}{A}\frac{\Delta P_r}{P_r} \qquad (1\text{-}4)$$

, where A is the sensitivity factor, P_r is the reflected microwave from the sample, ΔP_r is the transient P_r value with pulse irradiation. $\Delta\sigma$ is also described as follows:

$$\Delta\sigma = en\Sigma\mu = eF\phi\Sigma\mu \qquad (1\text{-}5)$$

, where e is the elementary charge, n is the density of photogenerated charge carriers, $\Sigma\mu$ is the sum of charge carrier mobilities, F is the correction factor that includes the absorbed photon density, and ϕ is the quantum efficiency of the charge carrier generation. When a laser is used as the light source, $\phi\Sigma\mu$ is mostly used instead of $\Delta\sigma$.

Here, the important features of TRMC is as follows: i) Intrinsic charge carrier dynamics is evaluated by excluding the effects of contact and significant trapping effect. ii) Owing to the rapidness of sample preparation and measurement, large scale screening is possible. iii) It is possible to reveal the charge transfer between two layers via the measurement of multilayered samples. Given these properties, numerous Bi- and Sb-based materials were investigated by TRMC.

1-6. Outline of This Work

In this dissertation, the author presents new insights into the molecule-induced transformation properties of LHPs and THPs, and the optoelectronic properties of Bi- and Sb-based semiconductors as alternative absorber. It has been known that metal halide perovskites are degraded in ambient condition through the deformation of crystal structure and chemical doping. However, the detailed understanding of how their optoelectronic nature change is still an ongoing mater. The next chapter reveals the oxidation effect on the physical properties of THPs and the anomalous thermoresponsive emission behavior of LHPs nanoparticles.

The following chapters are regarding the exploration of Bi- and Sb-based materials. Motivated by the instability and toxicity of LHPs and THPs, the author focused on Bi, and subsequently on Sb. Although there are several reports on Bi- and Sb-based materials, comprehensive evaluation of these materials are still lacking. Besides, the development of solution-based thin film fabrication process is also a remaining task. In Chapter 3, invention of a new fabrication process of Bi_2S_3 thin film is presented, which increases charge mobility with low dark current. The works described in Chapter 4 and 5 are comprehensive investigation of Bi- and Sb-based materials having various structures. The contents of each chapter are outlined as follows.

In *Chapter 2*, the transformation properties of THPs and LHPs induced by molecular adsorption are presented. Firstly, the effect of air exposure on THPs were studied using TRMC and photoelectron yield spectroscopy (PYS). Time-dependent measurement with minute-scale interval elucidated the changing of photoconductivity and energy level as a function of air exposure time. The effect of the composition of THPs and additives are also revealed. Secondly, the new temperature-dependent luminescence property of LHPs nanoparticles (NPs) was discovered. The addition of methylamine (CH_3NH_2) on NPs colloidal solution induced lowest solution critical temperature (LCST) behavior, where NPs dissolves in solution at low temperature, whereas they appear at high temperature. Lastly, based on optical and structural analysis, the mechanism of the phenomena was successfully provided.

In *Chapter 3*, the development of a new fabrication process of Bi_2S_3 thin film with high charge mobility is described. Among TRMC screening of inorganic semiconductors, Bi_2S_3 powder was found to show extremely high photoconductivity. However, Bi_2S_3 thin films prepared by previous methods such as NPs deposition, CBD, etc. showed

significantly low photoconductivity or large dark current, resulting in small light/dark current ratio. By focusing on crystal growth, the author established the new process for preparation of Bi_2S_3 film with large crystal grain and high purity. The obtained film exhibited 460 of light/dark current ratio under AM 1.5G, 6~420-fold larger than those of the films prepared by previous methods.

In *Chapter 4*, the comparative study of the charge carrier dynamics of Bi-based halide dimer $A_3Bi_2I_9$ (A = Cs, MA, FA) and double perovskite $Cs_2AgBiBr_6$ based on TRMC evaluation were presented. The evaluation of single layer of absorber and multilayer such as ETM/Absorber provides the insights into interlayer charge transport. Although $Cs_2AgBiBr_6$ afforded superior charge transport, the charge extraction is assumed to be still insufficient, due probably to low charge separation efficiency. This is considered as the origin of the limited current density of $A_3Bi_2I_9$ and $Cs_2AgBiBr_6$ solar cells.

In *Chapter 5*, it is described that comprehensive evaluation of Bi- and Sb-based materials with 44 compositions were performed. The crystal structure formation, energy level, photoconductivity, and interlayer transport property were revealed by XRD, PYS, photoabsorption spectroscopy, and TRMC. Interestingly, several Sb-based materials such as SbSI, Sb_2S_3, $AgSbI_4$, and $MASbSI_2$ showed remarkable increase in photoconductivity by combining with TiO_2. This is considered as a result of efficient electron transfer. It was also revealed that the inclusion of thiophene unit in HTM affords highly improved interlayer hole transport. Finally, SbSI-based solar cells showed the highest PCE of 2.91% under AM 1.5G, which is notably high among solution processed Bi- and Sb-based solar cells.

1-7. Reference

[1] World Energy Assessment. United Nations Department of Economic and Social Affairs, World Energy Council, New York.

[2] International Energy Outlook 2017. U.S. Energy Information Administration, 2017.

[3] Best Research Cell Efficiencies Chart. National Renewable Energy Laboratory (NREL), https://www.nrel.gov/pv/cell-efficiency.html

[4] Tang, C. W. *Appl. Phys. Lett.* **1986**, *48*, 183–185.

[5] O'Regan, B.; Grätzel, M. *Nature* **1991**, *353*, 737–740.

[6] Plass, R.; Pelet, S.; Krueger, J.; Grätzel, M. *J. Phys. Chem. B* **2002**, *106*, 7578–7580.

[7] Kojima, A.; Teshima, K.; Shirai, Y.; Miyasaka, T. *J. Am. Chem. Soc.* **2009,** *131*, 6050–6051.

[8] Kim, H. –S.; Lee, C. –R.; Im, J. –H.; Lee K. –B.; Moehl, T.; Marchioro, A.; Moon, S. –J.; Humphry–Baker, R.; Yum. J. –H.; Moser, J. E.; Grätzel, M.; Park. N. –G. *Sci. Rep.* **2012**, *2*, 591/1–7.

[9] Mubarok, M. A.; Aqoma, H.; Wibowo, F. T. A.; Lee, w.; Kim, H. M.; Ryu, D. Y.; Jeon, J.–W.; Jang, S.–Y. *Adv. Energy Mater.* **2020**, *10*, 1902933/1–9.

[10] Madogni, V. I.; Kounouhéwa, B.; Akpo, A.; Agbomahéna, M.; Hounkpatin, S. A.; Awanou, C. N. *Chem. Phys. Lett.* **2015**, *640*, 201–214.

[11] Yin, X.; Song, Z.; Li, Z.; Tang, W. *Energy Environ. Sci.* **2020**, 13 4057–4086.

[12] Hawash, Z.; Ono, L. K.; Qi, Y. *Adv. Mater. Interfaces* **2016**, *3*, 1–6.

[13] Nguyen, W. H.; Bailie, C. D.; Unger, E. L.; Mcgehee, M. D. *J. Am. Chem. Soc.* **2014**, *136*, 10996–11001.

[14] Cai, N.; Moon, S. J.; Cevey-Ha, L.; Moehl, T.; Humphry-Baker, R.; Wang, P.; Zakeeruddin, S. M.; Grätzel, M. *Nano Lett.* **2011**, *11*, 1452–1456.

[15] Chang, J. A.; Rhee, J. H.; Im, S. H.; Lee, Y. H.; Kim, H. J.; Seok, S. Il; Nazeeruddin, M. K.; Gratzel, M. *Nano Lett. 2010*, *10*, 2609–2612.

[16] Wang, L.; Zhao, D.; Su, Z.; Shen, D. *Nanoscale Res. Lett.* **2012**, *7*, 2–7.

[17] Saliba, M.; Correa-Baena, J. P.; Wolff, C. M.; Stolterfoht, M.; Phung, N.; Albrecht, S.; Neher, D.; Abate, A. *Chem. Mater.* **2018**, *30*, 4193–4201.

[18] Konstantakou, M.; Stergiopoulos, T. *J. Mater. Chem. A* **2017**, *5*, 11518–11549.

[19] Alcocer, M. J. P.; Leijtens, T.; Herz, L. M.; Petrozza, A.; Snaith, H. J. *Science* **2013**, *342*, 341–344.

[20] Wehrenfennig, C.; Eperon, G. E.; Johnston, M. B.; Snaith, H. J.; Herz, L. M. *Adv. Mater.* **2014**, *26*, 1584–1589.

[21] Yang, W. S.; Park, B. –W.; Jung, E. H.; Jeon, N. J.; Kim, Y. C.; Lee, D. U.; Shin, S. S.; Seo, J.; Kim, E. K.; Noh, J. H.; Seok, S. I. *Science* **2017**, *356*, 1376–1379.

[22] Lee, M. M.; Teuschere, J.; Miyasaka, T.; Murakami, T. N.; Snaith, H. J. *Science* **2012**, *338*, 643–647.

[23] Jeon, N. J.; Noh, J. H.; Kim, Y. C.; Yang, W. S.; Ryu, S.; Seok, S. I. *Nat. Mater.* **2014**, *13*, 897–903.

[24] Shockley, W.; Queisser, H. J. *J. Appl. Phys.* **1961**, *32*, 510–519.

[25] Kim, H. D.; Miyamoto, Y.; Kubota, H.; Yamanari, T.; Ohkita, H. *Chem. Lett.* **2017**, *46*, 253–256.

[26] Kim, H. D.; Yanagawa, N.; Shimazaki, A.; Endo, M.; Wakamiya, A.; Ohkita, H.; Benten, H.; Ito, S. *ACS Appl. Mater. Interfaces* **2017**, *9*, 19988–19997.

[27] Docampo, P.; Ball, J. M.; Darwich, M.; Eperon, G. E.; Snaith, H. J. *Nat. Commun.* **2013**, *4*, 2761/1–6.

[28] Chen, Q.; Chen, L.; Ye, F.; Zhao, T.; Tang, F.; Rajagopal, A.; Jiang, Z.; Jiang, S.; Jen, A. K. Y.; Xie, Y.; Cai, J.; Chen, L. *Nano Lett.* **2017**, *17*, 3231–3237.

[29] Meng, L.; Sun, C.; Wang, R.; Huang, W.; Zhao, Z.; Sun, P.; Huang, T.; Xue, J.; Lee, J. W.; Zhu, C.; Huang, Y.; Li, Y.; Yang, Y. *J. Am. Chem. Soc.* **2018**, *140*, 17255–17262.

[30] Löper, P.; Stuckelberger, M.; Niesen, B.; Werner, J.; Filipič, M.; Moon, S. J.; Yum, J. H.; Topič, M.; De Wolf, S.; Ballif, C. *J. Phys. Chem. Lett.* **2015**, *6*, 66–71.

[31] Yamada, Y.; Nakamura, T.; Endo, M.; Wakamiya, A.; Kanemitsu, Y. *J. Am. Chem. Soc.* **2014**, *136*, 11610–11613.

[32] Oga, H.; Saeki, A.; Ogomi, Y.; Hayase, S.; Seki, S. *J. Am. Chem. Soc.* **2014**, *136*, 13818–13825.

[33] Kim, D. H.; Park, J.; Li, Z.; Yang, M.; Park, J. S.; Park, I. J.; Kim, J. Y.; Berry, J. J.; Rumbles, G.; Zhu, K. *Adv. Mater.* **2017**, *29*, 1606831/1–8.

[34] Miyata, K.; Zhu, X. Y. *Nat. Mater.* **2018**, *17*, 379–381.

[35] Xing, J.; Yan, F.; Zhao, Y.; Chen, S.; Yu, H.; Zhang, Q.; Zeng, R.; Demir, H. V.; Sun, X.; Huan, A.; Xiong, Q. *ACS Nano* **2016**, *10*, 6623–6630.

[36] Chen, J.; Du, W.; Shi, J.; Li, M.; Wang, Y.; Zhang, Q.; Liu, X. *InfoMat.* **2020**, *2*, 170–183.

[37] Umebayashi, T.; Asai, K. *Phys. Rev.* **2003**, 2–7.

[38] Tanaka, K.; Takahashi, T.; Ban, T.; Kondo, T.; Uchida, K.; Miura, N. **2003**, *127*, 619–623.

[39] Yin, W. J.; Yang, J. H.; Kang, J.; Yan, Y.; Wei, S. H. *J. Mater. Chem. A* **2015**, *3*, 8926–8942.

[40] Kanemitsu, Y.; Handa, T. *Jpn. J. Appl. Phys.* **2018**, *57*, 090101/1–17.

[41] Christians, J. A.; Miranda Herrera, P. A.; Kamat, P. V. *J. Am. Chem. Soc.* **2015**, *137*, 1530–1538.

[42] Seth, C.; Khushalani, D. *RSC Adv.* **2016**, *6*, 101846–101852.

[43] Li, B.; Fei, C.; Zheng, K.; Qu, X.; Pullerits, T.; Cao, G.; Tian, J. *J. Mater. Chem. A* **2016**, *4*, 17018–17024.

[44] Liang, J.; Zhao, P.; Wang, C.; Wang, Y.; Hu, Y.; Zhu, G.; Ma, L.; Liu, J.; Jin, Z. *J. Am. Chem. Soc.* **2017**, *139*, 14009–14012.

[45] Liang, J.; Wang, C.; Wang, Y.; Xu, Z.; Lu, Z.; Ma, Y.; Zhu, H.; Hu, Y.; Xiao, C.; Yi, X.; Zhu, G.; Lv, H.; Ma, L.; Chen, T.; Tie, Z.; Jin, Z.; Liu, J. *J. Am. Chem. Soc.* **2016**, *138*, 15829–

15832.
[46] Dedecker, K.; Grancini, G. *Adv. Energy Mater.* **2020**, *10*, 2001471/1–8.
[47] Hao, F.; Stoumpos, C. C.; Cao, D. H.; Chang, R. P. H.; Kanatzidis, M. G. *Nat. Photonics* **2014**, *8*, 489–494.
[48] Hao, F.; Stoumpos, C. C.; Chang, R. P. H.; Kanatzidis, M. G. *J. Am. Chem. Soc.* **2014**, *136*, 8094–8099.
[49] Konstantakou, M.; Stergiopoulos, T. A *J. Mater. Chem. A* **2017**, *5*, 11518–11549.
[50] Song, T.; Yokoyama, T.; Aramaki, S.; Kanatzidis, M. G. **2017**, 2, 897–903.
[51] Umari, P.; Mosconi, E.; De Angelis, F. *Sci. Rep.* **2014**, *4*, 4467/1–7.
[52] Hao, R.; Stoumpos, C.C.; Guo, P.; Zhou, N.; Marks, T. J.; Chang, R. P. H.; Kanatzidis, M. G. *J. Am. Chem. Soc.* **2015**, *137*, 11445−11452.
[53] Noel, N. K.; Stranks, S. D.; Abate, A.; Wehrenfennig, C.; Guarnera, S.; Haghighirad, A. –A.; Sadhanala, A.; Eperon, G. E.; Pathak, S. K.; Johnston, M. B. Petrozza, A.; Herz, L. M.; Snaith H. J. *Energy Environ. Sci.* **2014**, *7*, 3061–3068.
[54] Koh, T. M.; Krishnamoorthy, T.; Yantara, N.; Shi, C.; Leong, W. L.; Boix, P. P.; Grimsdale, A. C.; Mhaisalkar, S. G.; Mathews, N. *J. Mater. Chem. A* **2015**, *3*, 14996–15000.
[55] Kumar, M. H.; Dharani, S.; Leong, W. L.; Boix, P. P.; Prabhakar, R. R.; Baikie, T.; Shi, C.; Ding, H.; Ramesh, R.; Asta, M.; Graetzel, M.; Mhaisalkar, S. G; Mathews, N. *Adv. Mater.* **2014**, 26, 7122–7127.
[56] Kim, H. D.; Miyamoto, Y.; Kubota, H.; Yamanari, T.; Ohkita, H. *Chem. Lett.* **2017**, *46*, 253–256.
[57] Xu, P.; Chen, S.; Xiang, H. –J.; Gong, X. –G.; Wei, S. –H. *Chem. Mater.* **2014**, *26*, 6068−6072.
[58] Liao, W.; Zhao, D.; Yu, Y.; Grice, C. R.; Wang, C.; Cimaroli, A. J.; Schulz, P.; Meng, W.; Zhu, K.; Xiong, R. –G.; Yan, Y. *Adv. Mater.* **2016**, *28*, 9333–9340.
[59] Hao, R.; Stoumpos, C.C.; Guo, P.; Zhou, N.; Marks, T. J.; Chang, R. P. H.; Kanatzidis, M. G. *J. Am. Chem. Soc.* **2015**, *137*, 11445−11452.
[60] Noel, N. K.; Stranks, S. D.; Abate, A.; Wehrenfennig, C.; Guarnera, S.; Haghighirad, A. –A.; Sadhanala, A.; Eperon, G. E.; Pathak, S. K.; Johnston, M. B.; Petrozza, A.; Herz, L. M.; Snaith, H. J. *Energy Environ. Sci.* **2014**, *7*, 3061–3068.
[61] Koh, T. M.; Krishnamoorthy, T.; Yantara, N.; Shi, C.; Leong, W. L.; Boix, P. P.; Grimsdale, A. C.; Mhaisalkar, S. G.; Mathews, N. *J. Mater. Chem. A* **2015**, *3*, 14996–15000.
[62] Sabba, D.; Mulmudi, H. K.; Prabhakar, R. R.; Krishnamoorthy, T.; Baikie, T.; Boix, P. P.; Mhaisalkar, S.; Mathews, N. *J. Phys. Chem. C* **2015**, *119*, 1763−1767.
[63] Nishimura, K.; Kamarudin, M. A.; Hirotani, D.; Hamada, K.; Shen, Q.; Iikubo, S.; Minemoto, T.; Yoshino, K.; Hayase, S. *Nano Energy* **2020**, *74*, 104858/1−10.
[64] Yang, S.; Fu, W.; Zhang, Z.; Chen, H.; Li, C.-Z. *J. Mater. Chem. A* **2017**, *5*, 11462–11482.
[65] Shi, Z.; Guo, J.; Chen, Y.; Li, Q.; Pan, Y.; Zhang, H.; Xia, Y.; Huang, W. *Adv. Mater.* **2017**, *29*. 1605005/1–28.

[66] Ran, Z.; Wang, X.; Li, Y.; Yang, D.; Zhao, X. G.; Biswas, K.; Singh, D. J.; Zhang, L. *npj Comput. Mater.* **2018**, *4*, 14/1–7.

[67] Xiao, Z.; Song, Z.; Yan, Y. *Adv. Mater.* **2019**, *31*, 1803792/1–22.

[68] Jin, Z.; Zhang, Z.; Xiu, J.; Song, H.; Gatti, T.; He, Z. *J. Mater. Chem. A* **2020**, *8*, 16166–16188.

[69] Green, M. A.; Hishikawa, Y.; Dunlop, E. D.; Levi, D. H.; Hohl-Ebinger, J.; Ho-Baillie, A. W. Y. *Prog. Photovolt. Res. Appl.* **2018**, *26*, 3–12.

[70] Kurley, J. M.; Panthani, M. G.; Crisp, R. W.; Nanayakkara, S. U.; Pach, G. F.; Reese, M. O.; Hudson, M. H.; Dolzhnikov, D. S.; Tanygin, V.; Luther, J. M.; Talapin, D. V. *ACS Energy Lett.* **2017**, *2*, 270−278.

[71] Azimi, H.; Hou, Y.; Brabec, C. J. *Energy Environ. Sci.* **2014**, *7*, 1829–1849.

[72] Park, B. W.; Philippe, B.; Zhang, X.; Rensmo, H.; Boschloo, G.; Johansson, E. M. J. *Adv. Mater.* **2015**, *27*, 6806–6813.

[73] Shin, S. S.; Baena, J. P. C.; Kurchin, R. C.; Polizzotti, A.; Yoo, J. J.; Wieghold, S.; Bawendi, M. G.; Buonassisi, T. *Chem. Mater.* **2018**, *30*, 336–343.

[74] Boopathi, K. M.; Karuppuswamy, P.; Singh, A.; Hanmandlu, C.; Lin, L.; Abbas, S. A.; Chang, C. C.; Wang, P. C.; Li, G.; Chu, C. W. *J. Mater. Chem. A* **2017**, *5*, 20843–20850.

[75] Szklarz, P.; Jakubas, R.; Gagor, A.; Bator, G.; Cichos, J.; Karbowiak, M. *Inorg. Chem. Front.* **2020**, *7*, 1780–1789.

[76] Leng, M.; Chen, Z.; Yang, Y.; Li, Z.; Zeng, K.; Li, K.; Niu, G.; He, Y.; Zhou, Q.; Tang, J. *Angew. Chem. Int. Ed.* **2016**, *55*, 15012–15016.

[77] Kim, Y.; Yang, Z.; Jain, A.; Voznyy, O.; Kim, G. H.; Liu, M.; Quan, L. N.; García de Arquer, F. P.; Comin, R.; Fan, J. Z.; Sargent, E. H. *Angew. Chem. Int. Ed.* **2016**, *55*, 9586–9590.

[78] Zhu, H.; Pan, M.; Johansson, M. B.; Johansson, E. M. J. *ChemSusChem* **2017**, *10*, 2592–2596.

[79] Sansom, H. C.; Whitehead, G. F. S.; Dyer, M. S.; Zanella, M.; Manning, T. D.; Pitcher, M. J.; Whittles, T. J.; Dhanak, V. R.; Alaria, J.; Claridge, J. B.; Rosseinsky, M. J. *Chem. Mater.* **2017**, *29*, 1538–1549.

[80] Slavney, A. H.; Hu, T.; Lindenberg, A. M.; Karunadasa, H. I. *J. Am. Chem. Soc.* **2016**, *138*, 2138–2141.

[81] Steele, J. A.; Puech, P.; Keshavarz, M.; Yang, R.; Banerjee, S.; Debroye, E.; Kim, C. W.; Yuan, H.; Heo, N. H.; Vanacken, J.; Walsh, A.; Hofkens, J.; Roeffaers, M. B. J. *ACS Nano* **2018**, *12*, 8081–8090.

[82] Gao, W.; Ran, C.; Xi, J.; Jiao, B.; Zhang, W.; Wu, M.; Hou, X.; Wu, Z. *ChemPhysChem* **2018**, *19*, 1696–1700.

[83] Martinez, L.; Bernechea, M.; De Arquer, F. P. G.; Konstantatos, G. *Adv. Energy Mater.* **2011**, *1*, 1029–1035.

[84] Choi, Y. C.; Seok, S. I. *Adv. Funct. Mater.* **2015**, *25*, 2892–2898.

[85] Guin, S. N.; Biswas, K. *Chem. Mater.* **2013**, *25*, 3225–3231.
[86] Kumar, M.; Persson, C. *Energy Procedia* **2014**, *44*, 176–183.
[87] Yao, J.; Shao, J.; Wang, Y.; Zhao, Z.; Yang, G. *Nanoscale* **2015**, *7*, 12535–12541.
[88] Yao, J.; Zheng, Z.; Yang, G. *Adv. Funct. Mater.* **2017**, *27*, 1701823/1–10.
[89] Yao, J.; Yang, G. *Small* **2018**, *14*, 1704524/1–8.
[90] Choi, Y. C.; Lee, D. U.; Noh, J. H.; Kim, E. K.; Seok, S. I. *Adv. Funct. Mater.* **2014**, *24*, 3587–3592.
[91] Peng, B.; Xu, K.; Zhang, H.; Ning, Z.; Shao, H.; Ni, G.; Li, J.; Zhu, Y.; Zhu, H.; Soukoulis, C. M. *Adv. Theory Simulations* **2018**, *1*, 1700005/1–7.
[92] Nie, R; Mehta, A.; Park, B.; Kwon, H. –W.; Im, J.; Seok, S. I. *J. Am. Chem. Soc.* **2018**, *140*, 872–875.
[93] Nie, R.; Yun, H. S.; Paik, M. J.; Mehta, A.; Park, B. W.; Choi, Y. C.; Seok, S. I. *Adv. Energy Mater.* **2018**, *8*, 1701901/1–7.
[94] Li, T.; Wang, X.; Yan, Y.; Mitzi, D. B. *J. Phys. Chem. Lett.* **2018**, *9*, 3829–3833.
[95] Shin, S. S.; Correa Baena, J. P.; Kurchin, R. C.; Polizzotti, A.; Yoo, J. J.; Wieghold, S.; Bawendi, M. G.; Buonassisi, T. *Chem. Mater.* **2018**, *30*, 336–343.
[96] Sfaelou, S.; Raptis, D.; Dracopoulos, V.; Lianos, P. *RSC Adv.* **2015**, *5*, 95813–95816.
[97] Hahn, N. T.; Rettie, A. J. E.; Beal, S. K.; Fullon, R. R.; Mullins, C. B. *J. Phys. Chem. C* **2012**, *116*, 24878–24886.
[98] Martinez, L.; Bernechea, M.; De Arquer, F. P. G.; Konstantatos, G. *Adv. Energy Mater.* **2011**, *1*, 1029–1035.
[99] Zhang, Q.; Wu, C.; Qi, X.; Lv, F.; Zhang, Z.; Liu, Y.; Wang, S.; Qu, B.; Chen, Z.; Xiao, L. *ACS Appl. Energy Mater.* **2019**, *2*, 3651–3656.
[100] Pantaler, M.; Cho, K. T.; Queloz, V. I. E.; Fettkenhauer, C.; Anusca, I.; Nazeeruddin, M. K.; Lupascu, D. C.; Grancini, G. *ACS Energy Lett.* **2018**, *3*, 1781–1786.
[101] Bernechea, M.; Miller, N. C.; Xercavins, G.; So, D.; Stavrinadis, A.; Konstantatos, G. *Nat. Photonics* **2016**, *10*, 521–525.
[102] Sonawane, P. S.; Patil, L. A. *Mater. Chem. Phys.* **2007**, *105*, 157–161.
[103] Raut, S. S.; Dhobale, J. A.; Sankapal, B. R. *Physica E* **2017**, *87*, 209–212.
[104] Khadraout, M.; Benramdane, N.; Miloua, R.; Mathieu, C.; Bo *Optoelectron. Adv. Mater.* **2015**, *9*, 1167–1170.
[105] MacLachlan, A. J.; O'Mahony, F. T. F.; Sudlow, A. L.; Hill, M. S.; Molloy, K. C.; Nelson, J.; Haque, S. A. *ChemPhysChem* **2014**, *15*, 1019–1023.
[106] Gu, E.; Lin, X.; Tang, X.; Matt, G. J.; Osvet, A.; Hou, y.; Jäger, S.; Xie, C.; Karl, A.; Hock, R.; Brabec, C. J. *J. Mater, Chem. C* **2018**, *6*, 7642–7651.

Chapter 2: Transformation Mechanism of Pb and Sn Perovskite via Molecular Adsorption and Evolution for PL Switching

2-1. Introduction

The problem lying on both of LHPs and THPs is their instability in the air. It has been known that methyl ammonium lead iodide ($MAPbI_3$) suffers gradual deterioration within a few days in humidity.[1] Meanwhile, the oxygen-induced degradation in THPs is more serious. Because the addition of SnF_2 to $CsSnI_3$ was found to mitigate the initial *p*-doping,[2] a relatively large amount of SnF_2 (10−20 mol %) is mixed with $MASnI_3$ or formamidinium-cation- [$HC(NH_2)^{2+}$-, FA-) based $FASnI_3$, exhibiting PCEs of 2−6%.[3,4−8] However, the dark carrier density is still high even after SnF_2 addition (~10^{17} cm^{-3}),[4,9] and the mechanism remains poorly understood.

In the first half of this chapter, the author presents the electrochemical and optoelectronic properties of $MASnI_3$ and $FASnI_3$ with/without SnF_2 additive. These properties were systematically evaluated using the photoelectron yield spectroscopy (PYS)[10] and laser flash-photolysis time-resolved microwave conductivity (TRMC),[11,12] particularly regarding the effect of air exposure. With the use of PYS and TRMC, the change in the valence band maxima (VBM) level and the transient conductivity is evaluated. PYS is a type of ultraviolet photoelectron spectroscopy (UPS) that records the photocurrent extracted under a relatively high extraction voltage (10−100 V) upon UV irradiation (shorter than 310 nm). Consequently, it allows for the evaluation of a wide range of samples including thick films and powders in a vacuum and even in air. The author performed PYS and TRMC measurements of powder samples instead of thin film samples to retard degradation process. The observed shift in VBM (PYS) and decrease of transient conductivity (TRMC) are important when designing the device structure of a THP solar cells and in deepening the understanding of the degradation process.

As for LHPs, the high humidity induces the irreversible formation of LHPs-H_2O complex, resulting in the degradation. Meanwhile, the phase transition induced by methylammonium (CH_3NH_2) gas is reversibly occurred in room temperature.[13] Given the specific interaction between LHP and CH_3NH_2, the latter half of this chapter regards to an unprecedented lower critical solution temperature (LCST) for methylammonium lead bromide ($MAPbBr_3$) nanoparticle (NP) colloidal solution with the presence of CH_3NH_2. This implies the possibility of controlling the crystal structure and chemical compositions

through external stimulation such as temperature, which may enable reversible switching of emission property. On the other hand, aqueous polymer solutions represented by poly(N-isopropylacrylamide) (PNIPA) are known to exhibit a temperature-triggered coil–globule transition, which leads to a lower critical solution temperature (LCST).[14] Through dipole–dipole and hydrogen-bonding interactions in water, PNIPA is hydrated below a cloud point ($T_C \approx 32$ °C), but becomes shrunken and precipitates through the liberation of hydrated water molecules above this temperature.[15,16] It is the low dissolution entropy of the polymer that is responsible for this reversible conformational change, thus making similar behavior a rarity in molecular or inorganic materials due to the fact that a high entropy at high temperatures tends to favor dissolution. Particularly, a luminescent LCST system that is truly made of "molecules" or "ions" has never yet been achieved.

In this chapter, it is presented what is believed to be the first example of LCST behavior in LHP NPs that not only involves a transition between solution and suspension but also photoemission switching between blue (430 nm) and green (525 nm). A reversible LCST has been achieved by adding a few amounts of CH_3NH_2 found to facilitate the formation and decomposition of perovskite NPs at the desired temperature (30−80 °C). These compounds are neutral/ionic molecules (e.g., $CH_3NH_3^+$) and metal/halogen ions (Pb^{2+}, Br^-) that have atomic (molecular) weights of less than three hundred. The self-organization of organic–inorganic species in nonpolar solvent, which is mediated by an intermediate 1D crystal, was also found to have a marked effect on the thermoresponsive phenomenon, thus making it distinctly different to conventional LCST mechanisms based on the hydration and dehydration of polymers or molecules.

2-2. Results and Discussion

2-2-1. Energetics of THPs Studied Using PYS

The PYS spectra of $MASnI_3$ without air exposure exhibit a distinct rise of the form (yield)1/n, where the onset positions are mostly unchanged by the addition of 20 mol % SnF_2 (Figure 2-1a). Generally, n = 3 is used for semiconductors,[17,18] whereas n = 2 is used for metals.[19] This empirical power law is inferred from the results of vibrational transition probabilities and surface transmission probabilities.[20] In the present analysis, n = 3 was used, which affords a good linear fitting for the base and the increase to calculate the onset that corresponds to the VBM. (The use of n = 2 deepens the VBM by approximately 0.05 eV.) With increasing air exposure time, the yields gradually decrease, and the onsets become unclear. The degradations of the PYS spectra are almost the same between $MASnI_3$ and $FASnI_3$ (Figure 2-1b).

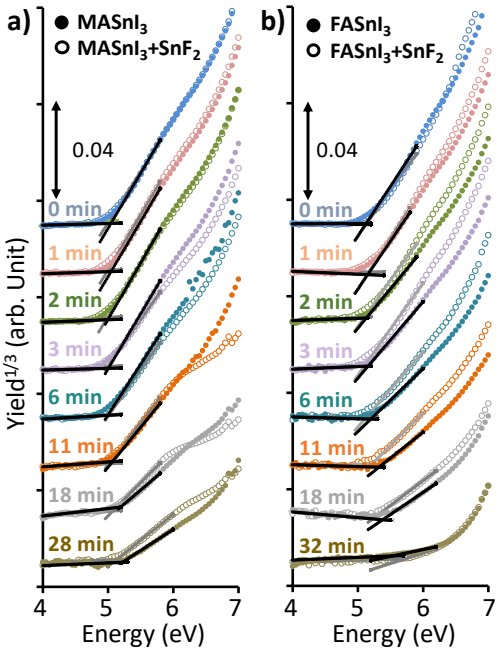

Figure 2-1. PYS spectra of (a) $MASnI_3$ (solid circles) and $MASnI_3$ + SnF_2 (open circles), and (b) $FASnI_3$ (solid circles) and $FASnI_3$ + SnF_2 (open circles). Solid lines are linear fittings without (black) and with (gray) 20 mol% SnF_2. Each line was determined as the pair of a base and a rise to calculate an onset (= VBM).

The VBMs of the THPs are plotted as functions of the air exposure time (Figure 2-2a). The VBM of $MASnI_3$ is −5.02 ± 0.03 eV, as averaged among the short air exposure times. The value is unlikely to be affected by the addition of SnF_2 (−5.00 ± 0.03 eV), whereas the downward shift of the VBM (e.g., −5.17 ± 0.04 eV at 18 min) owing to the degradation in air is slightly moderated by SnF_2 (−5.08 ± 0.03 eV at 18 min). The shift is accompanied by a decrease of the rise slope (Figure 2-2b), which makes the onset unclear after longer than 20 min. The VBM of lead-based $MAPbI_3$ powder evaluated using the same instrument is −5.45 ± 0.05 eV, which is consistent with those of other studies (from −5.40 to −5.50 eV).[21–24] However, the obtained VBM of $MASnI_3$ lies between the reported values of −4.75[25–27] and −5.47[28,29] eV. According to the results of air exposure

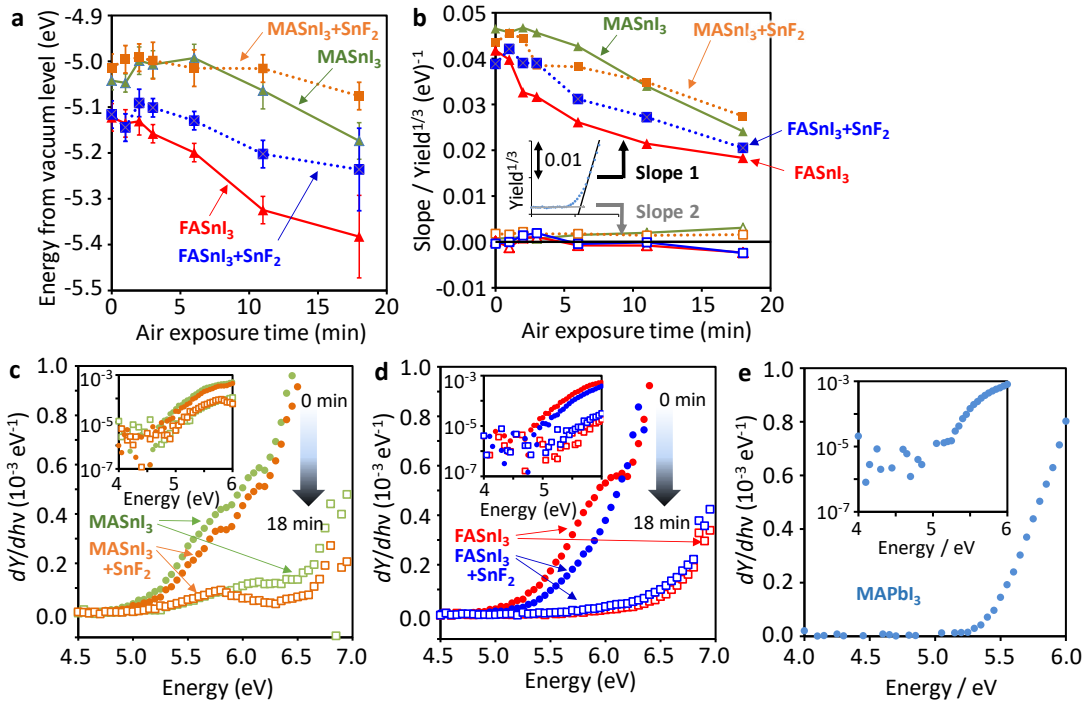

Figure 2-2. (a) Dependence of the VBMs of $MASnI_3$ and $FASnI_3$ with/without SnF_2 on air exposure time. (b) Slopes of the rise (slope 1, solid symbols) and the base (slope 2, open symbols) obtained from the fitting of the PYS spectra in Figure 2-1. (c,d,e) Derivatives of the PYS spectra of (c) $MASnI_3$ and $MASnI_3$ + SnF_2, (d) $FASnI_3$ and $FASnI_3$ + SnF_2, and (e) $MAPbI_3$. Solid circles and open squares represent air exposure times of 0 and 18 min, respectively. Insets are semilogarithmic plots of dY/dhv vs hv, which is indicative of the onset from −4.7 to −4.8 eV for the fresh (0-min) samples.

effects, degradation might be involved in the reported deep VBM (approximately −5.5 eV). This could be further linked to the formations of low-dimensional perovskite (MA_2SnI_6, analogous to Cs_2SnI_6)[30,31] having a deep VBM (vide infra) or O_2/H_2O adducts.[32] Indeed, the VBM of $MASnI_3$ at 28 min is deepened by 0.2 eV to −5.22 eV. In addition, the deformed curves cause an uncertainty of the onset (between −5.2 and −5.5 eV) that depends on the fitting range. $FASnI_3$ shows a similar behavior with respect to the shift of the VBM and the effect of SnF_2. The initial VBMs of $FASnI_3$ without and with SnF_2 are mostly identical (−5.13 ± 0.03 and −5.12 ± 0.03 eV, respectively). They were shifted by approximately 0.2 eV to −5.38 eV (without SnF_2) and −5.24 eV (with SnF_2) at 18 min. The degradation is partly suppressed by SnF_2, whereas the deformation of the curve of $FASnI_3$ is more obvious than that of $MASnI_3$ at 32 min. The VBM of $FASnI_3$ is also in the middle of the previously reported values (−4.7[6,26] and −5.96[3] eV).

The excessively low-lying VBM (−5.96 eV)[3] is possibly explained by degradation as well. However, degradation alone is unable to account for the difference between the reported shallow VBM (−4.7 eV) and that of the fresh samples measured by the author (−5.0 eV).

For detailed discussion of electronic structures near the onsets of the PYS spectra, the author calculated the derivative of the photoelectron yield *dY*/*dhv* (*hv* is the photon energy in electronvolts), which is proportional to the effective density of the filled electronic states (density of states, DOS) near the band edge.[33] *dY*/*dhv* for $MASnI_3$ indicates a steep slope in the high-energy region (higher than 6.2 eV) and a less structured shoulder at 4.7−6.2 eV (Figure 2-2c). The shoulders (at 5.80 and 6.15 eV) are similar to those of $BaTiO_3$ and rubrene single crystals, the origins of which are the defect levels[34] and oxygen-related gap states,[35] respectively. The intensity of the shoulder was impeded by 20−30% upon the addition of SnF_2, but the spectral features remained mostly unchanged. *dY*/*dhv* was drastically decreased by air exposure, together with an increase in the shoulder intensity relative to the high-energy region. The results imply that the addition of SnF_2 to $MASnI_3$ initially decreases the defect-related DOS to some extent, but that the electronic states are significantly altered by air exposure regardless of the presence of SnF_2. After the oxidation, the shoulder became unclear, because it merged with the decreased main slope of the high-energy region.

Similarly, *dY*/*dhv* of $FASnI_3$ exhibited a clear shoulder with a single peak at ~6.15 eV; however, it disappeared upon mixing with SnF_2 (Figure 2-2d). This indicates that the initial defect-related DOS in $FASnI_3$ + SnF_2 is suppressed more effectively than that in $MASnI_3$ + SnF_2, which is consistent with the superior PCE of the state-of-the-art $FASnI_3$ solar cell.[4,6–8] Notably, such a shoulder is also not observed for the outperforming $MAPbI_3$ (Figure 2-2e). Interestingly, the semilogarithmic plot of *dY*/*dhv* versus *hv* (insets in Figure 2-2c, d) gives an onset between −4.7 and −4.8 eV, which coincides with the reported VBMs of $MASnI_3$ (−4.75 eV)[26,27] and $FASnI_3$ (−4.70 eV).[6,26]

Figure 2-3a shows the XRD patterns of $MASnI_3$ and $FASnI_3$ with/without SnF_2, which are identical to those of previous reports.[3,4,32] After 1 day of aging, the intensities were decreased for all of the samples, accompanying marginal shifts [e.g., ±0.15° for the (101) peak at $2\theta \approx 14.2°$; Figure 2-3b]. Note that the XRD measurements were performed in the air and that one scan took about 20 min, so that minute-scale degradation could not be evaluated. The changes in the XRD patterns are insignificant in comparison with those of previously reported spin-coated $MA(FA)SnI_3$ films, which exhibit the distinct formations of MA_2SnI_6, a yellow polymorph of $FASnI_3$, and oxygen-combined black $FASnI_3$ after 12 h of aging.[32] The difference could be due to the fact that these samples were powders, which retarded the diffusion of O_2/H_2O into the bulk.

Conjugated molecules and polymers such as 2,2′,7,7′-tetrakis(N,N-di-p-methoxyphenyl-amine)9,9′-spirobifluorene (spiro-OMeTAD) and poly(triarylamine) (PTAA) are often used as hole-transporting materials (HTMs) for perovskite solar cells. The highest occupied molecular orbital (HOMO) levels of these HTMs are between −5.1 and −5.2 eV,[23,24] which fit the VBM of $MAPbI_3$ (−5.5 eV) and render efficient hole transfer by virtue of a sufficient offset energy (0.3−0.4 eV).[12,27] However, the VBMs of $MASnI_3$ and $FASnI_3$ are close to the typical HOMO levels of HTMs, suggesting the importance of developing a new HTM suitable for THPs. By adding the reported optical band gaps (1.26 eV for $MASnI_3$ and 1.40 eV for $FASnI_3$)[6,27] to the VBMs, the conduction-band minima (CBMs) were calculated to be −3.76 and −3.73 eV for $MASnI_3$ and $FASnI_3$, respectively. These CBMs are moderate for efficient electron transfer to common electron-transporting materials (ETMs) including TiO_2, perylene diimide, and fullerenes.[36–38]

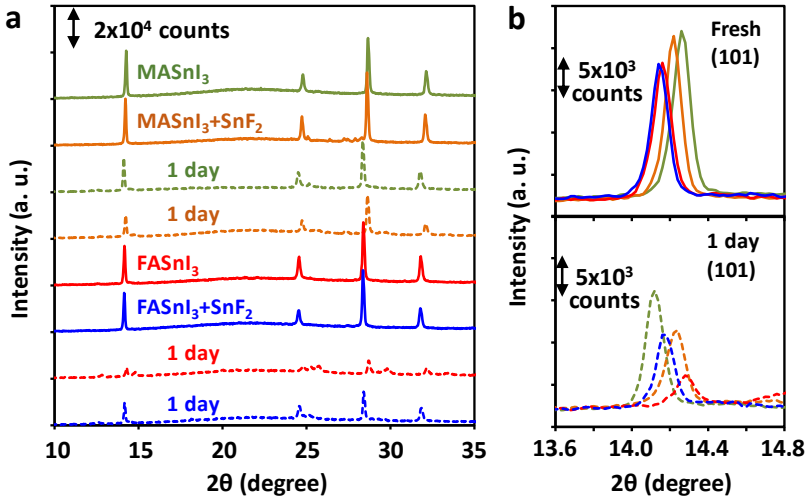

Figure 2-3. (a) Powder XRD patterns of $MASnI_3$ and $FASnI_3$ with/without SnF_2. The solid and dotted lines indicate fresh samples and 1-day-aged samples, respectively. Note that the XRD measurements were performed in the air and typically took 20 min for one scan. Therefore, fresh samples are not relevant to 0-min samples of PYS and TRMC. (b) Magnified (101) peaks at $2\theta \approx 14.2°$ for the fresh (top) and 1-day-aged (bottom) samples.

2-2-2. Degradation of Optoelectronics of THPs

To examine the electronic degradation of THPs upon exposure to air, $\phi\Sigma\mu$ transients (see eq. 1-5 in Chapter 1) were evaluated using TRMC (Figure 2-4a–d). As shown in Figure 2-4e, $FASnI_3 + SnF_2$ exhibits a progressive decrease of the $\phi\Sigma\mu$ maximum ($\phi\Sigma\mu_{max}$) on the minute scale. $\phi\Sigma\mu_{max}$ of $FASnI_3$ is 5.3×10^{-4} cm^2 V^{-1} s^{-1} without air exposure and

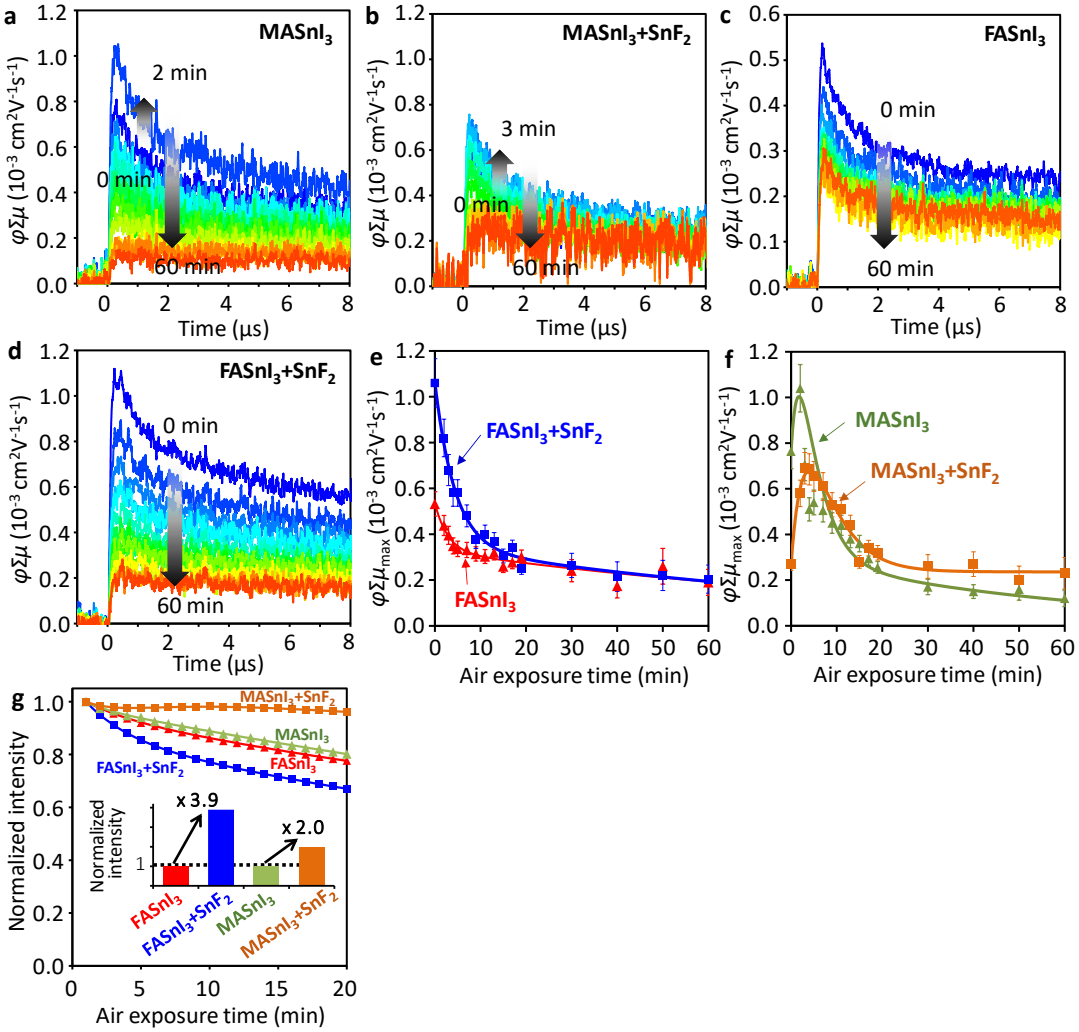

Figure 2-4. TRMC transients of (a) $MASnI_3$, (b) $MASnI_3 + SnF_2$, (c) $FASnI_3$, and (d) $FASnI_3 + SnF_2$. Colors indicate the total time of air exposure [from 0 min to 60 min]. (e) $\phi\Sigma\mu_{max}$ of $FASnI_3$ (triangles) and $FASnI_3 + SnF_2$ (squares) plotted against air exposure time. Solid lines are double exponential fittings. (f) $\phi\Sigma\mu_{max}$ values of $MASnI_3$ (triangles) and $MASnI_3 + SnF_2$ (squares) plotted against air exposure time. Solid lines represent triple-exponential fittings. (g) Normalized intensity of photoemission at 900 nm as a function of air exposure time. The inset shows the relative increase in the PL intensity by mixing SnF_2 into $FASnI_3$ or $MASnI_3$ after 1 min air exposure.

exponentially decreases to less than half that at 60 min.

The addition of SnF_2 to $FASnI_3$ results in an almost 2-fold enhancement in $\phi\Sigma\mu_{max}$ (1.1×10^{-3} cm^2 V^{-1} s^{-1}), whereas the degradation is accelerated. This leads to a merging of the $\phi\Sigma\mu_{max}$ values of $FASnI_3$ and $FASnI_3$ + SnF_2 into the same curve beyond 20 min. The enhancement of $\phi\Sigma\mu_{max}$ by SnF_2 is relevant to the decrease of the dark carrier density[4,9,39] and the disappearance of the shoulder-shaped DOS in the PYS spectra. Therefore, the addition of SnF_2 is supposed to improve the initial electronic quality of $FASnI_3$ perovskite, but not to prevent the successive degradation caused by air exposure.

The $\phi\Sigma\mu_{max}$ dependence of $MASnI_3$ on the air exposure time is somewhat strange in comparison with that of $FASnI_3$ (Figure 2-4f). The $\phi\Sigma\mu_{max}$ values of $MASnI_3$ and $MASnI_3$ + SnF_2 at 0 min are 7.6×10^{-4} and 2.7×10^{-4} cm^2 V^{-1} s^{-1}, respectively, which are slightly lower than that of $FASnI_3$. Notably, they exhibit a rapid rise at 2−4 min by 35−150% and an exponential decrease afterward.

Photoemission provides an aspect of the electronic quality of THP. The time evolutions of the photoemission intensities of the THPs are shown in Figure 2-4g. Upon the addition of SnF_2, the intensity at the initial time (~1 min) is considerably recovered (3.9-fold for $FASnI_3$ and 2.0-fold for $MASnI_3$), in qualitative agreement with the effect of SnF_2 observed in PYS and TRMC. The decrease of the photoemission intensity is slightly faster for $FASnI_3$ + SnF_2 than for $FASnI_3$. Conversely, the decrease for $MASnI_3$ is moderated by the addition of SnF_2. These results are consistent with the minute-scale degradation found in the $\phi\Sigma\mu_{max}$ of TRMC (Figure 2-4a−f). Note that the photoemission intensities themselves are higher for the SnF_2-added $MA(FA)SnI_3$ samples than for the non-added ones even after air exposure, reiterating the improvement of the initial electronic quality of the THP upon SnF_2 addition. Because no distinct rise in photoemission is observed on the minute scale, the reason for the initial rise in TRMC cannot be inferred from the photoemission.

The decrease of $\phi\Sigma\mu_{max}$ found in both air-exposed $MASnI_3$ and $FASnI_3$ is presumably due to the decomposition of 3-dimensional perovskite into SnI_2 or its H_2O complex,[32] in analogy with the degradation mechanism of $MAPbI_3$.[1,40] This degradation should cause only a decrease of $\phi\Sigma\mu_{max}$. Thus, another factor must be considered to explain the anomalous increase observed in $\phi\Sigma\mu_{max}$ of $MASnI_3$. The author hypothesize the formation of a low-dimensional perovskite MA_2SnI_6 that is a pseudo-double-perovskite of $MA_2Sn_2I_6$, in which two Sn(II) ions are replaced with one oxidized form of Sn(IV). The VBM of MA_2SnI_6 was found to be as deep as -6.35 ± 0.05 eV and remained almost constant up to 60 min of air exposure (Figure 2-5a). The PYS spectra underwent no deformation, indicating the good stability of MA_2SnI_6.

TRMC evaluation reveals a $\phi\Sigma\mu_{max}$ value of 1.7×10^{-3} cm^2 V^{-1} s^{-1} at 0 min and a mostly unchanged value of 2.0×10^{-3} cm^2 V^{-1} s^{-1} from 1 to 60 min (Figure 2-5b). These $\phi\Sigma\mu_{max}$ are about twice those of $FASnI_3$ + SnF_2 and $MASnI_3$, and the decay speed is greatly reduced. Therefore, MA_2SnI_6 exhibits good optoelectronic properties, although it is still far inferior to the lead-based $MAPbI_3$. A deep defect level in the band gap suggested by first-principles calculations is also noted.[41]

The XRD profile of MA_2SnI_6 powder is shown in Figure 2-5c, together with those of the 1-day-aged $MASnI_3$ + SnF_2. MA_2SnI_6 sample indicates a pattern similar to that of the reconstructed Cs_2SnI_6 with concurrent negative shifts due to the larger size of the MA cation compared to Cs. Notably, the aged $MASnI_3$ exhibits weak shoulders at 2θ = 12.8°, 14.8°, 25.7°, and 29.8° attributed to the intense peaks of MA_2SnI_6. The appearance of the MA_2SnI_6 peaks is more pronounced in the previously reported spin-coated $MASnI_3$ film

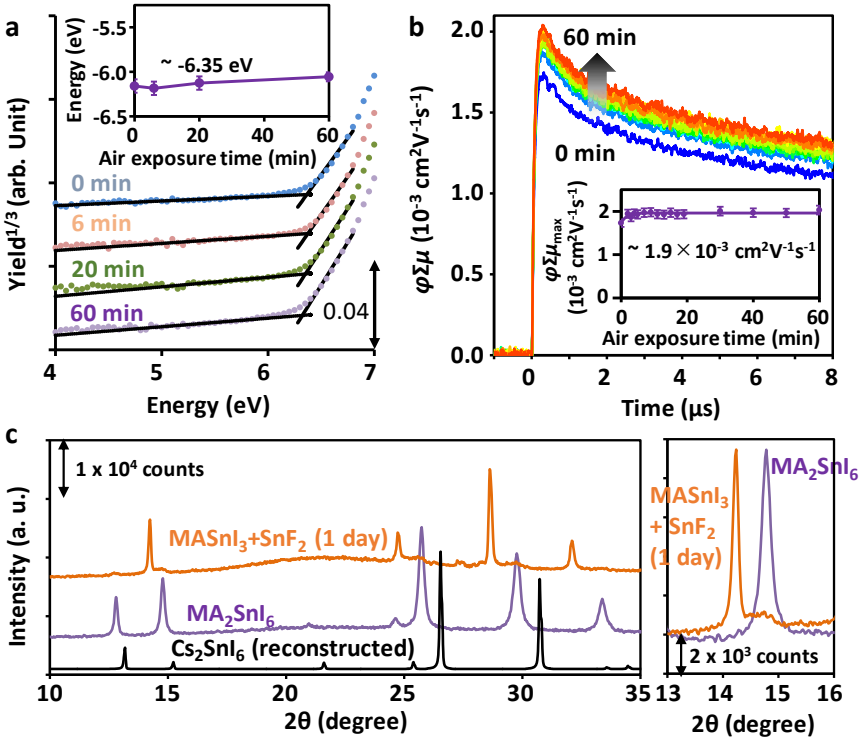

Figure 2-5. (a) PYS spectra of MA_2SnI_6. The corresponding air exposure time is appended in the figure. Solid black lines are linear fittings of a base and a rise to calculate an onset (= VBM). The inset shows the VBM dependence on the air exposure time. (b) TRMC transients of MA_2SnI_6. The inset shows $\phi\Sigma\mu_{max}$ plotted against the air exposure time. (c) Powder XRD profiles of 1-day-aged $MASnI_3$ + SnF_2, MA_2SnI_6, and Cs_2SnI_6 reconstructed from the crystallographic data of ref 42. The right panel shows a magnification at 2θ = 13−16°.

after 12 h of aging.[32] Accordingly, the formation of MA_2SnI_6 in powder sample is evident from the XRD results.

With the results in mind, the rapid (2−4-min) increase in $\phi\Sigma\mu_{max}$ found for $MASnI_3$ is assumed to be a result of the formation of MA_2SnI_6, in particular, on the surface of the powder. Unfortunately, the low-lying VBM and CBM are incompatible with common HTMs and ETMs. However, control of the formation of MA_2SnI_6 might serve as an alternative approach for improving the stability of THPs. Notably, the inclusion of low-dimensional perovskite through the addition of phenylethylammonium (PEA) to $FASnI_3$ (+10% SnF_2) was reported to afford a greatly enhanced stability and markedly improved PCE (5.94%)[8] in which the low-dimensional perovskite formed with PEA acts as the organic separating interlayer to block the inlet from oxygen and moisture. In the present study, addition of SnF_2 was found to improve the initial electronic quality (defect and photoconductivity maxima) of $FASnI_3$, although the degradation was rather accelerated. The degradation is assumed to be caused by oxygen and moisture in analogy with that of $MAPbI_3$,[1,40,42] and thus, the diffusion process of these reactants plays an important role,[42] which should be carefully examined for films with precisely controlled thicknesses, grain sizes, and compositions. The recent work on high-quality mixed-cation THP (8.12% PCE) is relevant to the further investigation of their degradation mechanism.[43]

2-2-3. Temperature-dependence of optical properties in LHP nanoparticles with methylammonium addition

Generally, the stability of LHPs in air is much higher than that of THPs because of the higher stability of Pb(II). However, the exposure to certain gas such as methylammonium (CH_3NH_2) induce rapid and reversible transformation between LHP black film state and transparent state (Figure 2-6). Inspired by this behavior, the author

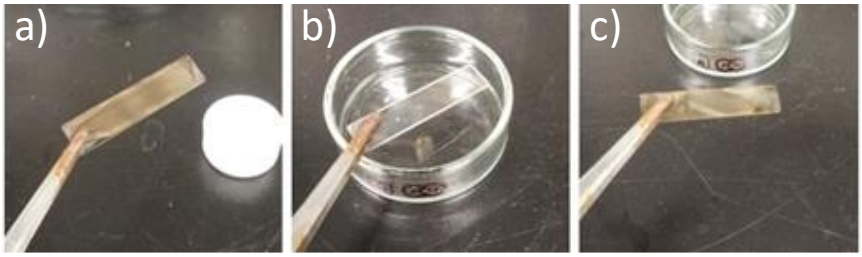

Figure 2-6. Pictures of $MAPbI_3$ thin films (a) before, (b) during, and (c) after CH_3NH_2 gas exposure. CH_3NH_2 gas was extracted from CH_3NH_2 solution dissolved in methanol (40 wt%).

investigated the interaction between LHP nanoparticles and CH_3NH_2.

The $MAPbBr_3$ NPs were synthesized using the ligand-assisted reprecipitation method.[44] In this way, NPs were readily formed even in air by dropping a dimethylformamide (DMF) solution of CH_3NH_3Br:$PbBr_2$:*n*-octylamine:oleic acid (1:1.25:0.75:9.9 by molar fraction) into vigorously stirred toluene (Figure 2-7a). The n-octylamine acts as a capping agent for the NPs, while the oleic acid prevents their

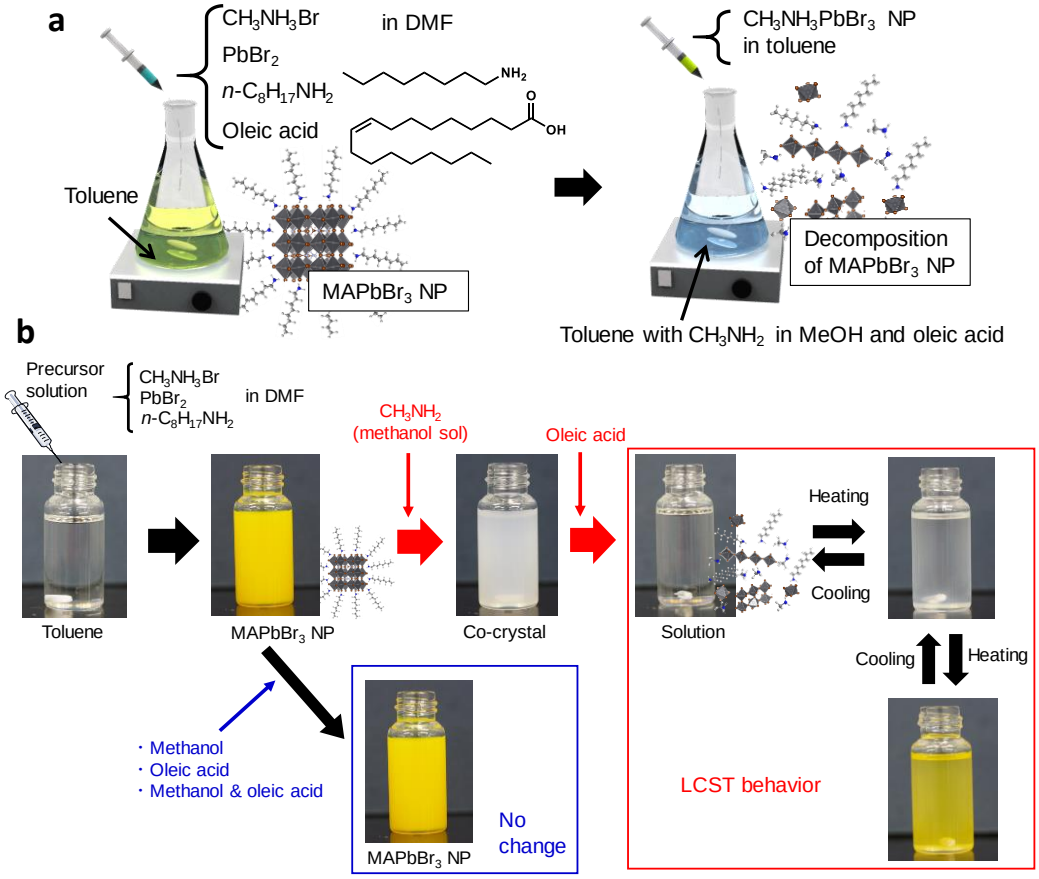

Figure 2-7. (a) Illustration of preparation procedure for $MAPbBr_3$ NP (left) and subsequent LCST system of NP+CH_3NH_2 (right). (b) Examination on the roles of involved chemicals (CH_3NH_2, oleic acid, and methanol). The upper panel shows the sequential addition of a methanol solution of CH_3NH_2 and oleic acid, which leads to LCST behavior. Meanwhile, addition of methanol, oleic acid, or methanol and oleic acid did not cause any changes, indicating that CH_3NH_2 plays a key role in the observed phenomena. This demonstrates that oleic acid fragmentizes the intermediate co-crystal into soluble $PbBr_2$ wire and prevents excessive NP growth. The white object at the bottom of the vial is a stirring bar.

excessive growth.[44] This NP suspension was subsequently added dropwise into 2 mL of toluene in the presence of a small amount of methylamine (10 μL of 40 wt% CH_3NH_2 in methanol), which caused the yellowish NP suspensions to immediately decompose and create a transparent solution. The addition of methanol and/or oleic acid without CH_3NH_2 did not cause any change in the NP suspension, thus confirming the need for CH_3NH_2 to decompose the NPs (Figure 2-7b). This idea came from the observation that a dark brown $MAPbI_3$ film is quickly and reversibly changed to a translucent film by exposing it to CH_3NH_2 vapor (Figure 2-6). The author has since examined other vapors such as NH_3, dimetylamine, n-propylamine, n-octylamine, DMSO (dimethyl sulfoxide), DMF, acetone, methanol, and ethanol, but of these, a clear reversible change is only found with NH_3 and CH_3NH_2. The use of NH_3 vapor induces a transition to a white film,[45] but excessive exposure results in an irreversible change, i.e., it only returned to perovskite when the film was thermally annealed at ≈110 °C. Using a methanol solution of NH_3 in place of CH_3NH_2 also produced decomposition of the NPs, but the suspension of white crystals remained insoluble. Similarly, although efficient and complete dissolution of the white crystals was possible with n-propylamine, no change was observed upon heating to 80 °C. Based on this, CH_3NH_2 was considered to be the most appropriate agent for creating a thermoresponsive function at moderate temperature, which may be associated with its ability to heal defects in collapsed $MAPbI_3$ crystals.[46] The versatile nature of CH_3NH_2 is also evident from the transformation of 2D $HPbI_3$ to 3D $MAPbI_3$ perovskite upon exposure to CH_3NH_2 gas, which delivers a high-quality LHP film and efficient solar cell.[13] The unique LCST behavior is also linked to the inverse solubility of $MAPbI_3$ in γ-butyrolactone.[47,48]

As shown in Figure 2-8a, increasing the solution temperature from 20 to 60 °C causes the photoabsorption tail at 600–900 nm to continuously raise due to light scattering by the NPs formed, which is accompanied by the evolution of the excitonic peak of MAPbBr3 at ≈525 nm.[49] On heating, the transparent solution turned yellowish, which was accompanied by a drastic shift in photoemission from blue (430 nm) to green (525 nm) (Figure 2-8b). Remarkably, the decomposition and formation of $MAPbBr_3$ NPs is fully reversible as long as CH_3NH_2 remains in solution (five cycles were tested, Figure 2-8c), but the transition speed of around 10–20 s is limited by the heat exchange between the solution and heat source.

Figure 2-9a represents the temperature dependence of photoabsorption at 700 and 800 nm, in which a sigmoidal increase in light scattering intensity can be observed that follows a similar trend to the LCST transition of PNIPA.[14–16] This is in sharp contrast to the $MAPbBr_3$ NPs without CH_3NH_2, which exhibit a flat dependence on temperature.

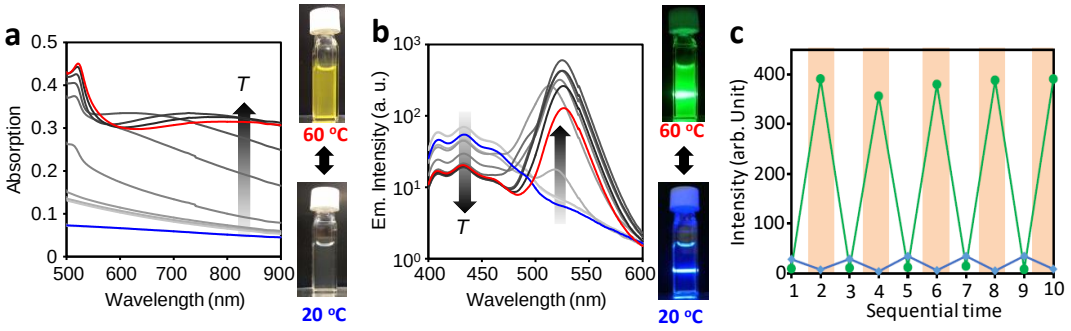

Figure 2-8. (a) photoabsorption and (b) photoemission (λ_{ex} = 350 nm) of NP+CH_3NH_2 solution on heating from 20 °C to 60 °C. The gray lines are the intermediate temperatures (white at low temperature to dark at high temperature). The insets show photographs of solution at 20 °C (lower) and suspension at 60 °C (upper) with (a) room lighting and (b) exposure to a CW laser (λ_{ex} = 375 nm) in darkness. (c) Plots of intensities at ~ 525 nm (green) and ~430 nm (blue) with the sequential number (even numbers divided by two represent the numbers of cycle).

Importantly, the T_c is determined by the concentration of CH_3NH_2 and oleic acid, i.e., NP+CH_3NH_2 (A) has a T_c of ≈40 °C that is increased to ≈50 °C with 3.7-fold increase in CH_3NH_2 and 1.5-fold increase in oleic acid in NP+CH_3NH_2 (B) (solid and open circles in Figure 2-9a, respectively). Note that an increase in either CH_3NH_2 or oleic acid can shift the sigmoidal curve to a higher temperature, but this deforms the curve in a different way (Figure 2-9b, c). Specifically, an increase in oleic acid simply produces a sharper transition at higher T_c, whereas CH_3NH_2 leads to the appearance of two distinct stepwise transitions at ≈40 and ≈55 °C. This suggests that each compound plays a different role in the multiple phase transition behind the LCST phenomenon.

Changing the relative molar concentration of $PbBr_2$ was used to create an LCST-type phase diagram (Figure 2-9d), the minimum point of which is at ≈55 °C. Phase transition is more manifest in the photoemissions presented in Figure 2-9e, wherein blue emission at 430 nm decreases with temperature and a green emission at 525 nm simultaneously emerges. These emissions crossover in terms of intensity in the early stage of phase transition, because the small $MAPbBr_3$ NPs that were initially formed are highly green emissive. Due to the same reason, the onset temperature of 525 nm emission intensity (≈35 °C) is slightly lower than the T_c observed in the photoabsorption (≈40 °C). During the formation and growth of NPs between 40 and 45 °C, a red-shift of ≈10 nm is observed along with an increase in intensity that can be ascribed to the quantum size effect[50] (Figures 2-9f). Even after the complete formation of NPs (>48 °C), a small red-

shift of 3–5 nm still occurs in both the absorption and photoemission peaks, which in turn reduces the photoemission intensity. This can be linked to the formation of nonradiative charge trapping sites in NPs, which are regarded as the cause of photocurrent loss in $MAPbI_3$ solar cells.[51,52] Electron–phonon coupling that reduces the optical bandgap of semiconductor could also be a possible mechanism for the red-shift, which has been

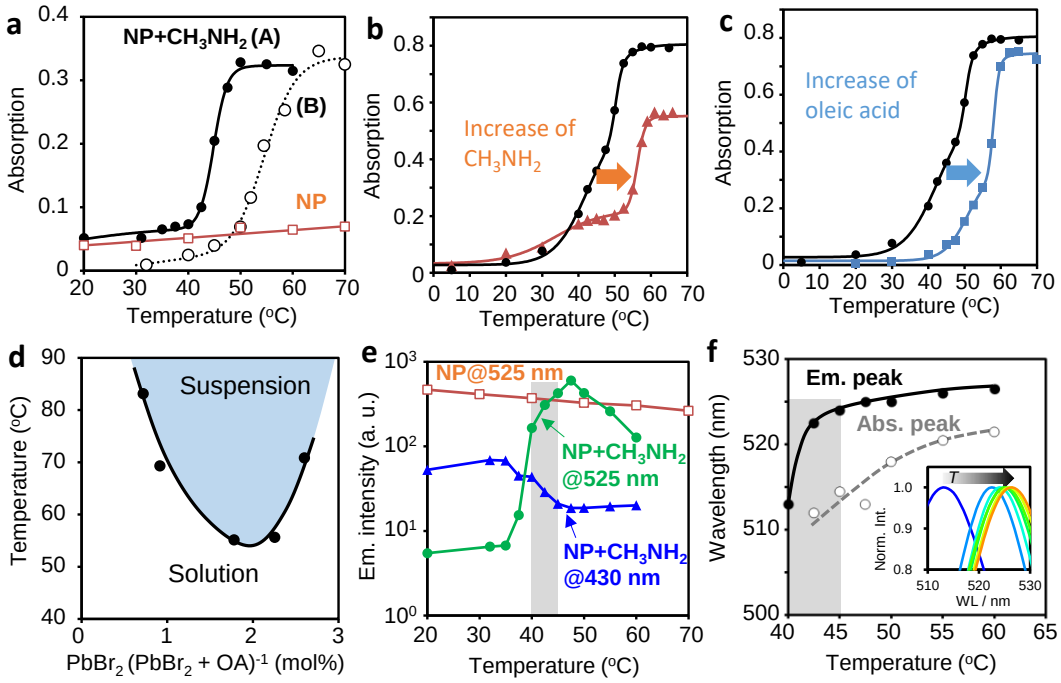

Figure 2-9. LCST transition on heating and phase diagram of $MAPbBr_3$ NP + CH_3NH_2. (a) Change in photoabsorption of LCST system A (closed circles at 800 nm) and B (open circles at 700 nm). Black solid and dotted lines are least-mean-square fits of three-state model (see the text). Open squares are control experiments of $MAPbBr_3$ NP with methanol and without CH_3NH_2 (the fitting line is linear fit). Photoabsorption change with increased (b) CH_3NH_2 concentration by 1.5-fold and (c) oleic acid concentration by 1.5-fold. (d) Phase diagram of NP+CH_3NH_2. Solid line is an eye-guide and OA is oleic acid. (e) Evolution of photoemission intensity at 525 nm (circles) and 430 nm (triangles) of NP+CH_3NH_2 (A). The open squares are control experiments of NP without CH_3NH_2 (λ_{ex} = 350 nm). (f) Spectral shift in photoemission peak (closed circles) and absorption peak (open circles) of NP+CH_3NH_2. The inset shows photoemission spectral change with increasing temperature from 40 °C to 60 °C. Solid lines are eye-guides. Gray areas in panels (e) and (f) correspond to regions of interest due to their large shift in photoemission.

observed in temperature- and pH-dependent aggregation-induced emission of 2D perovskite [$(C_nH_{2n+1}NH_3)_2PbI_4$].[53]

2-2-4. The mechanism of LCST behavior of LHPs nanoparticles

To provide structural and mechanistic insight into the LCST behavior observed, the $MAPbBr_3$ NPs and their complex with amines were subjected to X-ray diffraction (XRD) analysis. A spin-coated film of $MAPbBr_3$ NPs on quartz was found to produce an indices-assigned XRD spectrum identical to that presented in a previous report[54] (Figure 2-10a). However, a dropcasted film of transparent NP+CH_3NH_2 solution had the same spectrum as the original $MAPbBr_3$ NPs, because the CH_3NH_2 immediately evaporated.

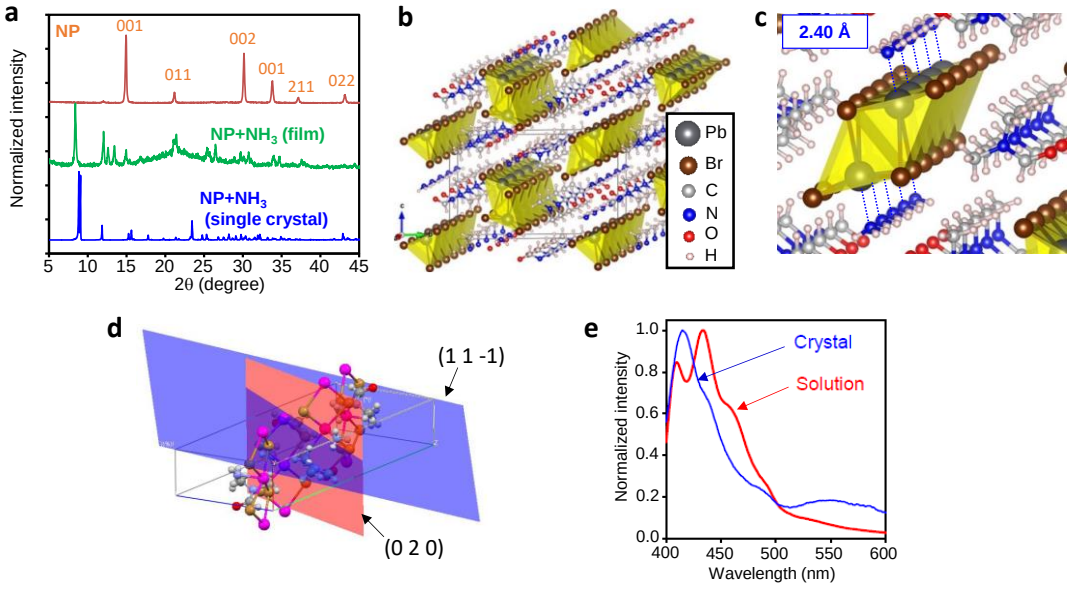

Figure 2-10. XRD results and LCST mechanism. (a) XRD spectra (λ = 1.54 Å) of $MAPbBr_3$ NP film, NP film treated with NH_3 vapor, and NP+NH_3 reconstructed from single-crystal XRD. (b) Crystal structure of $NH_3 \cdot PbBr_2 \cdot DMF$ determined by single crystal XRD (λ = 0.71 Å). (c) Magnified view of (b), wherein the coordination of $NH_3 \cdots Pb$ is connected by a dotted line. A pair of cofaced $PbBr_2$ networks is represented by a rhombic area. Pb and two Br atoms of cofaced $PbBr_2$ network are connected to form a polygon. (d) (1 1 −1) and (0 2 0) planes of $NH_3 \cdot PbBr_2 \cdot DMF$ crystal determined by using single crystal XRD. (e) Normalized photoemission spectra of solution state of NP + CH_3NH_2 at 20 °C (red, λex = 350 nm) and $NH_3 \cdot PbBr_2 \cdot DMF$ co-crystal (blue, λ_{ex} = 290 nm).

The $MAPbBr_3$ NP film was therefore exposed to NH_3 vapor, which cocrystalizes more strongly than CH_3NH_2, and this produced white crystals stable enough for XRD measurement. This combination of NP+NH_3 produced a complete change in the spectral features, with the most intense peak at a 2θ of 14.9° for $MAPbBr_3$ being moved to 8.4°. The spectrum contains weakened peaks of the original NP [e.g., (0 0 1), (0 1 1), (0 0 2), …] and unassigned complex pattern, in particular, at 2θ = 12.0°–13.4° and 25.4°–26.5°, the latter of which could be due to NP+NH_3 complex and regenerated $PbBr_2$.

By keeping a DMF solution of NP+NH_3 in a toluene-saturated vial under ambient conditions for one day, needle-shaped single crystals were successfully obtained (see Experimental). Analysis of these single crystals revealed a novel structure of NH_3·$PbBr_2$·DMF cocrystals, which included a 1D $PbBr_2$ network with a Pb–Br distance of 2.97–3.03 Å (Figure 2-10b). In addition, a pair of $PbBr_2$ wires was cofaced with

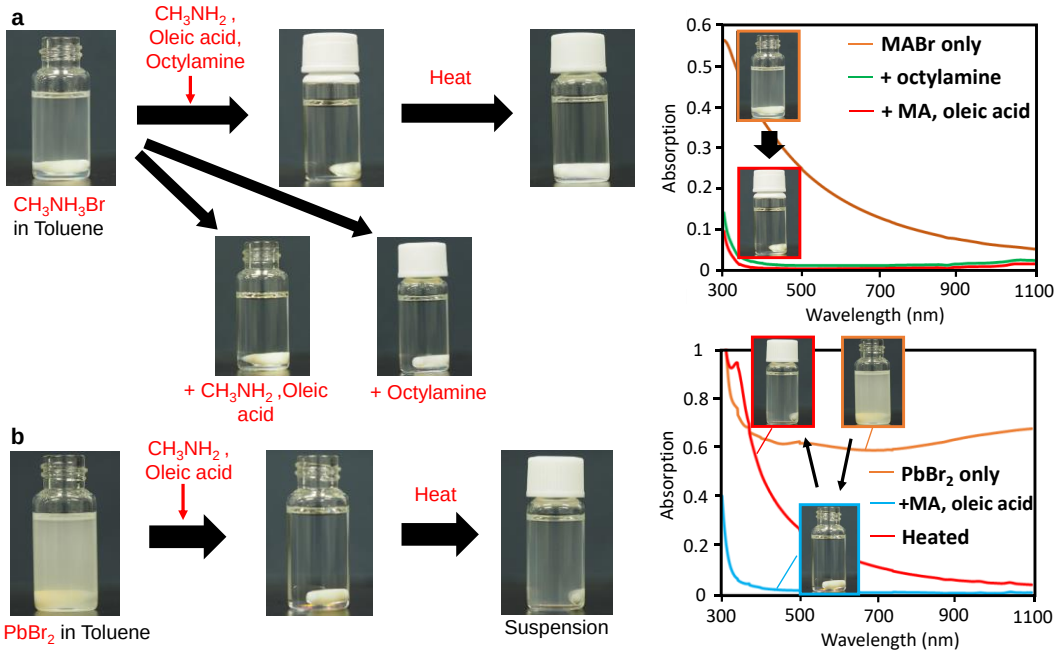

Figure 2-11. Examination of LCST behaviors of CH_3NH_3Br (MABr) and $PbBr_2$. (a) MABr in DMF was dispersed into toluene and then (CH_3NH_2 in methanol oleic acid, n-octylamine), (CH_3NH_2 in methanol, oleic acid), or (n-octylamine) was added. All of them led to dissolution, but did not show any LCST behaviors. (b) $PbBr_2$ in DMF was dispersed into toluene and then CH_3NH_2 in methanol and oleic acid were added, which led to dissolution. Upon heating, a white suspension is generated. These examinations support that the $PbBr_2$ is responsible for the formation of co-crystal and LCST behavior. In addition, MABr is dissolved when the $PbBr_2$ co-crystal is formed, but is trapped into $MAPbBr_3$ NP at a high temperature. The white object at the bottom of the vial is a stirring bar.

slipping along the longitudinal a-axis, and NH_3 coordinates with Pb ions at a distance of 2.40 Å (Figure 2-10c). The isotropic XRD spectrum reconstructed from the single crystal XRD data is analogous to that of a $MAPbBr_3$ NP film treated by NH_3 vapor (Figure 2-10a). The most intense peak of the reconstructed spectrum at the low angle is composed of two peaks [$2\theta = 8.9°$ and 9.1°, assigned to (1 1 −1) and (0 2 0), respectively]; however, it is likely merged into one peak in the NP+NH_3 film. Anisotropic orientation in the film may be a reason, because (1 1 −1) and (0 2 0) planes are perpendicular to each other (Figure 2-10d). Most importantly, the $NH_3 \cdot PbBr_2 \cdot DMF$ cocrystal produces a blue emission that peaks at 415 nm (Figure 2-10e), which is almost identical to that observed in the solution phase of NP+CH_3NH_2 (peaks at 409 and 433 nm). The blue emission from the LCST system is therefore ascribed to a 1D $PbBr_2$ network. The excess bromine anion (Br^-) and methylammonium cation (MA, $CH_3NH_3^+$) are dissolved in the solution by the aid of oleic acid and n-octylamine, as confirmed from stepwise addition of these reagents and no LCST behavior without $PbBr_2$ (Figure 2-11a). The $PbBr_2$ solution without MABr generates the cocrystals at a high temperature but no $MAPbBr_3$ NP (Figure 2-11b). These results are consistent with the lack of MABr in the composition of the cocrystal. The analogous complex adducts of $MAI \cdot PbI_2 \cdot x$DMSO in solid state also supports the obtained crystallographic results.[55–57]

In light of the XRD and optical spectroscopy results, the mechanism behind the LCST behavior was suggested to be that illustrated in Figure 2-12. Although the NP+CH_3NH_2 solution was unable to produce stable single crystals, most likely due to the weak coordination of CH_3NH_2 with Pb and distance between paired $PbBr_2$ wires, it is believed that a similar intermediate crystal is involved. The phase transition in Figure 2-9a consists of two sigmoidal curves: a small, gentle transition from room temperature to T_c; and a dominant, steep transition above T_c. Accordingly, the curve was analyzed using a three-state model given by the linear combination of two sigmoidal (Boltzmann) functions[57]

$$\text{Abs} = \sum_{n=1}^{2} \frac{A_n}{1+\exp(-\frac{T-T_n}{\varepsilon_n})} + A_0 \qquad (2\text{-}1)$$

where A_n (n = 0, 1, 2) is a scaling factor or baseline, T_n (n = 1, 2) is the transition temperature, and ε_n (n = 1, 2) is the degree of transition sharpness with temperature. A least-mean-square fitting showed good agreement with the experimental curves (the black solid and dotted lines in Figure 2-9a). Indeed, the three-state model is consistent with the emergence of intermediate white suspensions at the 2nd state (inset picture of Figure 2-12-ii), which are notably different to the yellowish $MAPbBr_3$ NP suspension formed at the 3rd state (Figure 2-12-iii). The solution state below the T_c is assumed to be a 1D wire

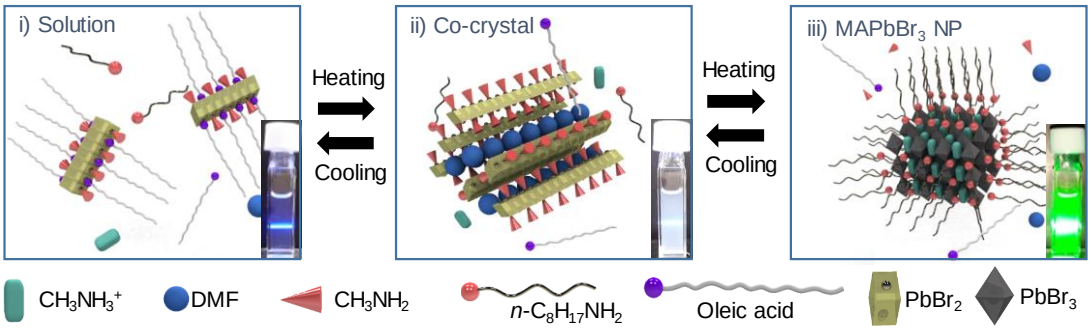

Figure 2-12. Mechanistic illustration of LCST behavior based on three-state model: (i) solution state, (ii) intermediate cocrystal state, and (iii) $MAPbBr_3$ NP state. The insets of each state are photographs under room light with exposure to a 375 nm CW laser.

of $PbBr_2$ coordinated by CH_3NH_2 and oleic acid (1st state, Figure 2-12-i). Without oleic acid, the suspension of white cocrystals formed via CH_3NH_2 coordination to Pb did not disappear, thereby underscoring the key role oleic acid plays in fragmentizing the intermediate cocrystal into soluble $PbBr_2$ wire and preventing excessive NP growth. The presence of oleic acid without CH_3NH_2, of course, causes no change in the NPs, highlighting the need for both CH_3NH_2 and oleic acid to create LCST behavior (Figure 2-7b).

Dynamic light scattering (DLS) confirmed that the NP+CH_2NH_2 solution has a relatively stable distribution at 30–50 °C (below T_c) and a small $D_{50\%}$ of 2.4–3.5 nm, as shown in Figure 2-13a. This size corresponds to 6–8 units of the $PbBr_2$ network, as illustrated in Figure 2-12-i. At 61 °C (above T_c), an abrupt and significant increase in particle size (~2.0 μm) was observed that corresponds to the formation of a NP suspension and aggregation. Note that the particle distribution evaluated by DLS is sensitive to the presence of larger particles, because the scattering intensity is dominated by the volume of particles. Cooling from 61 to 18 °C decomposed the NPs, and so the $D_{50\%}$ was reduced again to ~2.5 nm.

Picosecond fluorescence lifetime spectroscopy revealed two or three decay components in the photoemission of the LCST system (Figure 2-13b). In contrast, the emission of normal $MAPbBr_3$ NPs at 525 nm mostly exhibited a single exponential decay (average lifetime τ_{ave} = 7.2 ns at 25 °C, Figure 11c). Meanwhile, the τ_{ave} of the LCST system at 430 nm did not undergo any discernible change upon heating (~1.2 ns for 20–60 °C), but those at 525 nm were marginally elongated from 13.2 to 16.7 ns (Figure 2-13c). It was noticed that the lifetime is affected by the rate at which the temperature is increased and the concentration of the chemicals involved. A short lifetime is caused by

trapping sites[58] that are generated during the aggregation of NPs and/or an irregular transition from the intermediate co-crystal. Notably, diluting the solution and rapid heating produced photoemission quantum yields (QY) as high as 85% with an extended τ_{ave} of 73.7 ns (LCST2 in Figure 2-13b). This QY is equal to that previously reported for $MAPbBr_3$ NPs (80–90%),[59-61] and much larger than that for the LCST system without any optimization (typically a few percent).

Though first developed in perovskite NPs, further evolution of this molecular/ionic LCST system is foreseen owing to its versatile function of providing not only a transition between a solution and suspension, but also a drastic change in optical properties. For instance, both convection of fluid and temperature change are simultaneously visualized as fluorescent traces under UV light. Figure 2-14a shows a snapshot of the $MAPbBr_3$-based LCST solution during heating on a hot plate, where polystyrene is dissolved to increase the viscosity of the solution. The low viscous solution indicates a rapid and relatively homogeneous convection, whereas the high viscous solution shows a slow

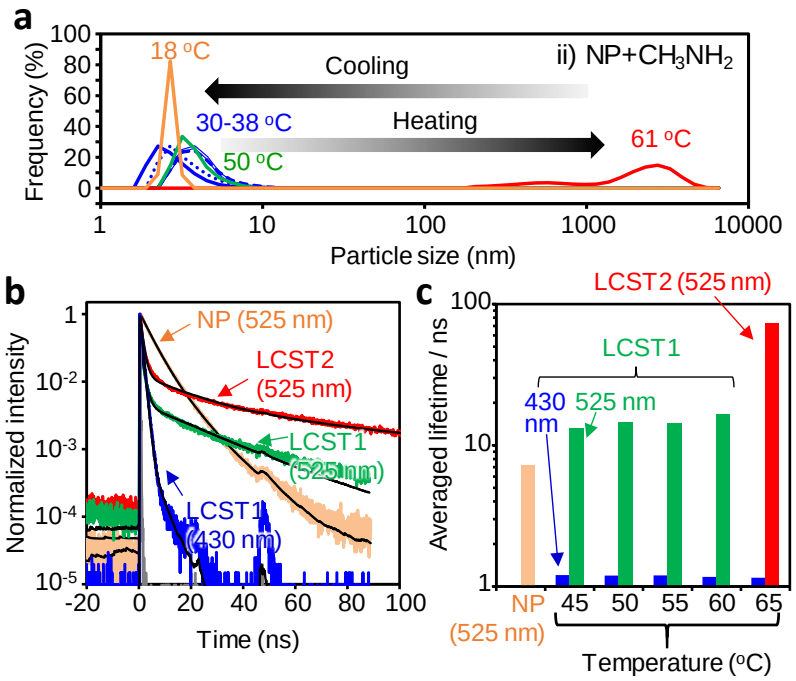

Figure 2-13. DLS and ps fluorescence lifetime spectroscopy of $MAPbBr_3$ NP+CH_3NH_2. (a) Particle size distribution of NP+CH_3NH_2 on heating from 30–50 °C (below T_c) to 61 °C (above T_c), and cooling to 18 °C. (b) Normalized photoemission decays at 525 nm for $MAPbBr_3$ NP (25 °C, orange), LCST1 (NP+CH_3NH_2 at 60 °C, green), and LCST2 with high quantum efficiency (NP+CH_3NH_2 at 65 °C, violet). λ_{ex} = 377 nm. The black lines are multiexponential fittings. (c) Average lifetimes of 525 nm decays of NP, LCST1, and LCST2.

diffusion followed by a sudden inhomogeneous build up, which forms Aurora-like traces. The latent green-emissive traces remain as long as the temperature is above T_c. Upon cooling on a cold plate, the bright photoluminescence disappears from the bottom and the solution turns back to the blue emission state (Figure 2-14b).

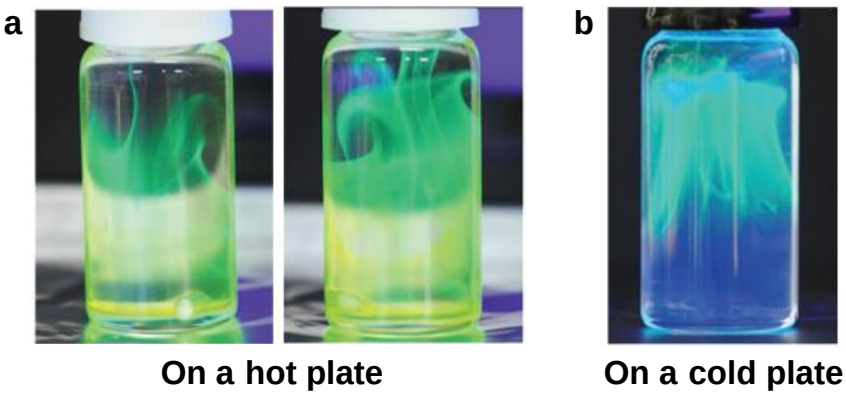

Figure 2-14. Visualization of fluid convection and temperature change in a toluene solution of polystyrene and $MAPbBr_3$+CH_3CH_2 under 365 nm irradiation. (a) Upon heating on a hot plate. (b) Upon cooling on a cold plate.

2-3. Conclusion

In this chapter, the investigation of the transformation behavior of THPs and LHPs with molecular adsorption were described. With the presence of oxygen, THPs showed significant deepening of VBM level in PYS evaluation. It was revealed that the addition of SnF_2 does not impact the VBMs without air exposure (−5.02 ± 0.03 eV for $MASnI_3$ and −5.13 ± 0.03 eV for $FASnI_3$), but suppress the defect-related DOS near the onset (deeper than −4.7 eV). The VBMs were gradually shifted to the deeper side after a few minutes of air exposure. This was accompanied by the deterioration of the PYS profiles, but was partly moderated by mixing with SnF_2. TRMC transient maxima of $FASnI_3$ progressively decreased with air exposure, where the addition of SnF_2 was found to improve the initial electronic quality instead of retarding the degradation itself. $MASnI_3$ exhibited the same degradation behavior, but concomitant with the anomalous peak at 2–4 min. The reason for the peak was suggested to be the formation of MA_2SnI_6, which shows a higher TRMC signal, deeper VBM (−6.35 ± 0.05 eV), and better stability. The author foresees further paths to an efficient, stable lead-free perovskite solar cell, where the energetics and degradation behavior revealed in the present study could be of help in designing the device structure and processing.

Meanwhile, LHPs did not show such a rapid changing with air exposure, but showed rapid and reversible transformation with CH_3NH_2 gas exposure. Inspired by the quick response to CH_3NH_2 vapor, the author developed a LCST system based on molecular/ionic materials that provides unique photoemission switching with a QY of up to 85%, as well as a transition between a solution and suspension. From single-crystal XRD analyses, a 1-dimensional $PbBr_2$ network coordinated by amine was identified as the blue-emitting entity. Furthermore, this intermediate phase was found to play an important role in generating green-emitting $MAPbBr_3$ NPs at high temperature. Accordingly, a three-state model was suggested to account for the observed transition in photoabsorption, wherein oleic acid and CH_3NH_2 mediate a reversible self-organization in the transition from a solution (1st state) to an intermediate suspension (2nd state) and NP suspension (3rd state). Given the ease with which the cloud point and emission color can be tuned via compositional engineering of concentration and halogen exchange, it is anticipated that this LCST system based on an organic-inorganic perovskite scaffold will give rise to a diverse range of new applications in thermoresponsive photonic materials.

2-4. Experimental

2-4-1. Preparation and evaluation of THPs powder

Sample preparation

MAI and FAI were purchased from Tokyo Chemical Industry (TCI) Co. Ltd. SnF_2 was purchased from Sigma-Aldrich Co. Llc. These materials were used as received. Dehydrated ethanol (super dehydrated) and *N,N*-dimethylformamide (DMF, dehydrated-super) were purchased from Wako Pure Chemical Industries Ltd. and Kanto Chemical. Co. Inc., respectively, which were further dried over molecular sieves and degassed by Ar gas bubbling for 1h before use. As a purified precursor for THPs, [SnI_2(dmf)] complex was prepared by recrystallization from a DMF solution of SnI_2 (sublimed, TCI) in an Ar-filled glove box (O_2 ~10 ppm). The details on preparation and characterization of the [SnI_2(dmf)] complex will be reported elsewhere.[23] In an Ar-filled glove box, MAI (or FAI), [SnI_2(dmf)], and SnF_2 in DMF (1 M) were dissolved in ethanol at the stoichiometric ratio (1:1:0 or 1:1:0.2 in molar fraction). The reaction mixture was stirred at 80 °C for 30 min. The obtained pale green solution was cooled down to afford blackish green crystalline powder. After filtration and washed with ethanol, powder of $MASnI_3$ or $FASnI_3$ with/without SnF_2 was obtained. MA_2SnI_6 was prepared in the same fashion using MAI and a SnI_4 precursor (purchased from Aldrich) at 2:1 stoichiometry (no addition of SnF_2).

Photoelectron yield spectroscopy

PYS experiments were carried out using a Bunko Keiki BIP-KV201 (accuracy: ±0.02 eV, extraction voltage = 10 V) in a vacuum ($<10^{-2}$ Pa). In a N_2-filled glove box (O_2 ~ 0.0 ppm), powder samples were placed on a conductive carbon tape on glass, which was contacted through aluminum tape and an Au-coated electrode. Note that carbon tape without samples gives a deep onset energy (~ −6.9 eV), and the intensity of the photoelectron yield is about two orders of magnitude smaller than those of THPs. Thus, the effect of the carbon tape is negligible. The sample was transferred in a pass box from the glove box to another one (O_2 ~ 50 ppm) that was directly connected to the chamber of the PYS. After each measurement (about 20 min in total), the sample was moved outside the glove box to be exposed to air. The air exposure time is the integrated value of each exposure time. The temperature and humidity of the air are ~ 25°C and 60%, respectively, which were not precisely controlled, but mostly constant.

Time-resolved microwave conductivity and photoemission spectroscopy

In a N_2-filled glove box, powder samples were placed on adhesive tape on a quartz plate and set in a sealed resonant cavity. The sample in a cavity was moved outside, set in a microwave circuit, and subject to a TRMC evaluation using continuous microwaves at approximately 9.1 GHz. The third harmonic generation of a Nd:YAG laser (Continuum Inc., Surelite II, 5–8-ns pulse duration, 10 Hz) was used as the excitation (incident photon density, I_0 = 1.8 × 10^{15} photons cm^{-2} $pulse^{-1}$). The photoconductivity transient $\Delta\sigma$ was converted to $\phi\Sigma\mu$ based on the eq. 1-5 in Chapter 1.

After the first measurement (=0 min), the cavity was open to air (~ 25°C and 60% humidity), and measurements were conducted (the air exposure time is the time after opening the cavity). Photoemission spectroscopy was performed using a Jasco FP-8300 spectrometer. A powder sample on a quartz plate was prepared in the same way as those of the TRMC evaluation. The time evolution of emission (λ_{ex} = 500 nm, λ_{em} = 900 nm) was recorded from 1 min after the removal of a sample from a glove box. Powder X-ray diffraction (XRD) data were collected on a Rigaku MiniFlex-600 using Cu−K_α radiation (λ = 1.54187 Å) at room temperature in the air.

2-4-2. Preparation and evaluation of LHPs nanoparticles (NPs)

Preparation of NPs and LCST Solution.

The 0.08 mmol CH_3NH_3Br, 0.10 mmol $PbBr_2$, 10 μL *n*-octylamine, and 250 μL oleic acid were dissolved in 5 mL of DMF. To prepare $MAPbBr_3$ NP+CH_3NH_2 (A), 80 μL of the abovementioned DMF precursor solution was added dropwise into 2.5 mL of vigorously-stirred dehydrated toluene to produce a suspension of $MAPbBr_3$ NPs. A 0.5 ml sample of this solution was then added to 2 mL of dehydrated toluene containing 10 μL of a 40% CH_3NH_2 (ca. 9.8 mmol mL^{-1}) methanol solution and 2 μL of oleic acid, which produced a transparent solution. For $MAPbBr_3$ NP+CH_3NH_2 (B), 80 μL of the DMF precursor solution was added dropwise to 2.5 mL of toluene to create a NP suspension. A 0.5 mL sample of this NP suspension was then added to 2 mL of toluene along with 10 μL of a CH_3NH_3 methanol solution and 20 μL of oleic acid diluted ten-fold in toluene. A high fluorescence quantum yield (HQY) solution was obtained through ten-fold dilution of (A) by adding 60 μL of the DMF precursor solution dropwise to 20 mL of toluene containing 7 μL of a CH_3NH_3 methanol solution and 10 μL of oleic acid diluted ten-fold in toluene.

General Measurement

UV-vis and fluorescence spectroscopy were performed using a Jasco V-730 UV-Vis spectrophotometer and Jasco FP-8300 spectrometer, respectively. The fluorescence quantum yield was evaluated relative to a fluorescein reference (QY = 92%) using these same spectrometers after their sensitivity was calibrated with Rhodamine B. Picosecond fluorescence lifetime measurements based on the time-correlated single-photon counting (TCSPC) technique were performed using a HORIBA model FluoroCube 3000U-UltraFast-SP spectrophotometer (λ_{ex} = 377 nm). Dynamic light scattering measurements were performed using a MicrotracBEL model NanotracWave UT-151 (λ_{probe} = 780 nm, detectable range: 0.8 nm ~ 6.5 μm) after passing each solution through a 0.45 μm membrane filter. Powder X-ray diffraction data were collected on a Rigaku RINT-2000 using graphite-monochromatised Cu−K_α radiation (λ = 1.54187 Å) at room temperature.

Single crystal XRD

Needle-shaped single crystals were obtained by poor solvent (toluene) diffusion of a DMF solution of NPs and NH_3 (Figure 2-15). Diffraction data were collected using a Rigaku XtaLAB mini with Mo–Kα radiation (λ= 0.71075 Å) at -60 °C. For $C_3H_{10}Br_2N_2OPb$, M_w = 457.13, a = 4.239(4), b = 19.47(2), c = 11.757(13) Å, α = 90°, β = 99.515(9)°, γ = 90°, V = 957.1(18) $Å^3$, T = 213 K, monoclinic, space group $P2_1/n$ (#14), Z = 4, ρ_{calcd} = 3.172 g cm^{-3}.

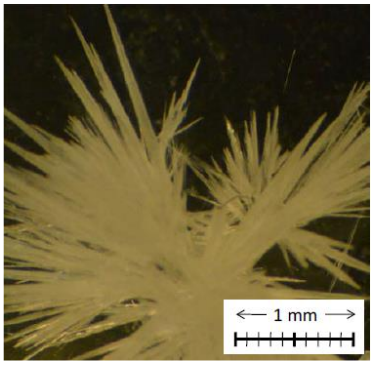

Figure 2-15. Needle-shaped single crystals of NH_3-$PbBr_2$-DMF grown by solvent diffusion method.

2-5. Reference

[1] Niu, G.D.; Li, W.Z.; Meng, F.Q.; Wang, L.D.; Dong, H.P.; Qiu, *J. Mater. Chem. A* **2014**, *2*, 705–710.

[2] Chung, I.; Lee, B.; He, J.; Chang, R. P. H.; Kanatzidis, M. G. *Nature* **2012**, *485*, 486−489.

[3] Koh, T. M.; Krishnamoorthy, T.; Yantara, N.; Shi, C.; Leong, W. L.; Boix, P. P.; Grimsdale, A. C.; Mhaisalkar, S. G.; Mathews, N. *J. Mater. Chem. A* **2015**, *3*, 14996–15000.

[4] Liao, W.; Zhao, D.; Yu, Y.; Grice, C. R.; Wang, C.; Cimaroli, A. J.; Schulz, P.; Meng, W.; Zhu, K.; Xiong, R. –G. Yan, Y.; *Adv. Mater.* **2016**, *28*, 9333–9340.

[5] Song, T. -.B; Yokoyama, T.; Stoumpos, C. C.; Logsdon, J.; Cao, D. H.; Wasielewski, M. R.; Aramaki, S.; Kanatzidis, M. G. *J. Am. Chem. Soc.* **2017**, *139*, 836−842.

[6] Ke, W.; Stoumpos, C. C.; Logsdon, J. L.; Wasielewski, M. R.; Yan, Y.; Fang, G.; Kanatzidis, M. G. *J. Am. Chem. Soc.* **2016**, *138*, 14998−15003.

[7] Lee, S. J.; Shin, S. S.; Kim, Y. C.; Kim, D.; Ahn, T. K.; Noh, J. H.; Seo, J.; Seok, S. I. *J. Am. Chem. Soc.* **2016**, *138*, 3974−3977.

[8] Liao, Y.; Liu, H.; Zhou, W.; Yang, D.; Shang, Y.; Shi, Z.; Li, B.; Jiang, X.; Zhang, L.; Quan, L.N.; *J. Am. Chem. Soc.* **2017**, *139*, 6693−6699.

[9] Hao, R.; Stoumpos, C.C.; Guo, P.; Zhou, N.; Marks, T. J.; Chang, R. P. H.; Kanatzidis, M. G. *J. Am. Chem. Soc.* **2015**, *137*, 11445−11452.

[10] Nakayama, Y.; Machida, S.; Tsunami, D.; Kimura, Y.; Niwano, M.; Noguchi, Y.; Ishii, H. *Appl. Phys. Lett.* **2008**, *92*, 153306/1−3.

[11] Oga, H.; Saeki, A.; Ogomi, Y.; Hayase, S.; Seki, S. *J. Am. Chem. Soc.* **2014**, *136*, 13818−13825.

[12] Hutter, E. M.; Hofman, J. –J.; Petrus, M. L.; Moes, M.; Abellón, R. D.; Docampo, P.; Savenije, T. J. *Adv. Energy Mater.* **2017**, *7*, 1602349/1−8.

[13] Pang, S.; Zhou, Y.; Wang, Z.; Yang, M.; Krause, A. R.; Zhou, Z.; Zhu, K.; Padture, N. P.; Cui, G. *J. Am. Chem. Soc.* **2016**, *138*, 750−753.

[14] Schild, H. G. *Prog. Polym. Sci.* **1992**, *17*, 163−249.

[15] Ramos, J.; Imaz, A.; Forcada, J. *Polym. Chem.* **2012**, *3*, 852–856.

[16] Deshmukh, S.; Mooney, D. A.; McDermott, T.; Kulkarni, S.; Don MacElroy, J. M. *Soft Matter* **2009**, *5*, 1514–1521.

[17] Kochi, M.; Harada, Y.; Hirooka, T.; Inokuchi, H. *Bull. Chem. Soc. Jpn.* **1970**, *43*, 2690–2701.

[18] Kane, E. O. *Phys. Rev.* **1962**, *127*, 131–141.

[19] Fowler, R. H. *Phys. Rev.* **1931**, *38*, 45–56.

[20] Williams, R.; Dresner, J. Photoemission of Holes from Metals into Anthracene. *J. Chem. Phys.* **1967**, *46*, 2133–2138.

[21] Belisle, R. A.; Jain, P.; Prasanna, R.; Leijtens, T.; McGehee, M. D. *ACS Energy Lett.* **2016**, *1*, 556−560.

[22] Malinkiewicz, O.; Yella, A.: Lee, Y. H.; Espallargas, G. M.; Grätzel, M. Nazeeruddin, M. K. Bolink, H. J. *Nat. Photonics* **2014**, *8*, 128–132.

[23] Nishimura, H.; Ishida, N.; Shimazaki, A.; Wakamiya, A.; Saeki, A.; Scott, L. T.; Murata, Y. *J. Am. Chem. Soc.* **2015**, *137*, 15656–15659.

[24] Ishida, N.; Wakamiya, A.; Saeki, A. *ACS Photonics* **2016**, *3*, 1678−1688.

[25] Ogomi, Y.; Morita, A.; Tsukamoto, S.; Saitho, T.; Fujikawa, N.; Shen, Q.; Toyoda, T.; Yoshino, K.; Pandey, S. S.; Ma, T.; Hayase, S. *J. Phys. Chem. Lett.* **2014**, *5*, 1004−1011.

[26] Song, T. –B.; Yokoyama, T.; Aramaki, S.; Kanatzidis, M. G. *ACS Energy Lett.* **2017**, *2*, 897−903.

[27] Yokoyama, T.; Cao, D. H.; Stoumpos, C. C.; Song, T. –B.; Sato, Y.; Aramaki, S.; Kanatzidis, M. G. *J. Phys. Chem. Lett.* **2016**, *7*, 776−782.

[28] Hao, F.; Stoumpos, C. C.; Cao, D. H.; Chang, R. P. H.; Kanatzidis, M. G. *Nat. Photonics* **2014**, *8*, 489−494.

[29] Hao, F.; Stoumpos, C. C.; Chang, R. P. H.; Kanatzidis, M. G. *J. Am. Chem. Soc.* **2014**, *136*, 8094−8099.

[30] Saparov, B.; Sun, J. –P.; Meng, W.; Xiao, Z.; Duan, H. –S.; Gunawan, O.; Shin, D.; Hill, I. G.; Yan, Y.; Mitzi, D. B. *Chem. Mater.* **2016**, *28*, 2315−2322.

[31] Maughan, A. E.; Ganose, A. M.; Bordelon, M. M.; Miller, E. M.; Scanlon, D. O.; Neilson, J. R. *J. Am. Chem. Soc.* **2016**, *138*, 8453−8464.

[32] Wang, F.; Ma,J.; Xie, F.; Li, L.; Chen, J.; Fan, J.; Zhao, N. *Adv. Funct. Mater.* **2016**, *26*, 3417–3423.

[33] Szuber, J. *Vacuum* **2000**, *57*, 209−217.

[34] Oshime, N.; Kano, J.; Ikeda, N.; Teranishi, T.; Fujii, T.; Ueda, T.; Ohkubo, T. *J. Appl. Phys.* **2016**, *120*, 154101/1−6.

[35] Machida, S. –i.; Nakayama, Y.; Duhm, S.; Xin, Q.; Funakoshi, A.; Ogawa, N.; Kera, S.; Ueno, N.; Ishii, H. *Phys. Rev. Lett.* **2010**, *104*, 156401/1−4.

[36] Liu, C.; Wang, K.; Du, P.; Meng, T.; Yu, X.; Cheng, S. Z. D.; Gong, X. *ACS Appl. Mater. Interfaces* **2015**, *7*, 1153−1159.

[37] Huang, J.; Yu, X.; Xie, J.; Li, C.- Z.; Zhang, Y.; Xu, D.; Tang, Z.; Cui, C.; Yang, D. *ACS Appl. Mater. Interfaces* **2016**, *8*, 34612−34619.

[38] Guo, Q.; Xu, Y.; Xiao, B.; Zhang, B.; Zhou, E.; Wang, R.; Bai, Y.; Hayat, T.; Alsaedi, A.; Tan, Z. *ACS Appl. Mater. Interfaces* **2017**, *9*, 10983−10991.

[39] Gupta, S.; Bendikov, T.; Hodes, G.; Cahen, D. $CsSnBr_3$, *ACS Energy Lett.* **2016**, *1*, 1028−1033.

[40] Christians, J. A.; Herrera, P. A. M.; Kamat, P. V. *J. Am. Chem. Soc.* **2015**, *137*, 1530−1538.

[41] Xiao, Z.; Zhou, Y.; Hosono, H.; Kamiya, T. *Phys. Chem. Chem. Phys.* **2015**, *17*, 18900−18903.

[42] Aristidou, N.; Eames, C.; Sanchez-Molina, I.; Bu, X.; Kosco, J.; Islam, M. S.; Haque, S. A. *Nat. Commun.* **2017**, *8*, 15218/1–10.

[43] Zhao, Z.; Gu, F.; Li, Y.; Sun, W.; Ye, S.; Rao, H.; Liu, Z.; Bian, Z.; Huang, C. *Adv. Sci.* **2017**, *4*, 1700204/1–7.

[44] Zhang, F.; Zhong, H.; Chen, C.; Wu, X. −g.; Hu, X.; Huang, H.; Han, J.; Zou, B.; Dong, Y. *ACS Nano* **2015**, *9*, 4533−4542.

[45] Zhao, Y.; Zhu, K. *Chem. Commun.* **2014**, *50*, 1605–1607.

[46] Zhou, Z.; Wang, Z.; Zhou, Y.; Pang, S.; Wang, D.; Xu, H.; Liu, Z.; Padture, N. P.; Cui, G. *Angew. Chem. Int. Ed.* **2015**, *54*, 9705 –9709.

[47] Kadro, J. M.; Nonomura, K.; Gachet, D.; Grätzel, M.; Hagfeldt, A. *Sci. Rep.* **2015**, *5*, 11654/1−6.

[48] Nayak, P. K.; Moore, D. T.; Wenger, B.; Nayak, S.; Haghighirad, A. A.; Fineberg, A.; Noel, N. K.; Reid, O. G.; Rumbles, G.; Kukura, P.; Vincent, K. A.; Snaith, H. J. *Nat. Comun.* **2016**, *7*, 13303/1−8.

[49] Grancini, G.; Kandada, A. R. S.; Frost, J. M.; Barker, A. J.; Bastiani, M. De; Gandini, M.; Marras, S.; Lanzani, G.; Walsh, A.; Petrozza, A. *Nat. Photonics* **2015**, *9*, 695–701.

[50] Huang, H.; Susha, A. S.; Kershaw, S. V.; Hung, T. F.; Rogach, A. L. *Adv. Sci.* **2015**, *2*, 1500194/1–5.

[51] Marchioro, A.; Teuscher, J.; Friedrich, D.; Kunst, M.; Krol, R. van de; Moehl, T.; Grätzel, M.; Moser, J. –E. *Nat. Photonics* **2014**, *8*, 250–255.

[52] Wu, B.; Nguyen, H. T.; Ku, Z.; Han, G.; Giovanni, D.; Mathews, N.; Fan, H. J.; Sum, T. C. *Adv. Energy Mater.* **2016**, *6*, 1600551/1–9.

[53] Niu, Y.; Zhang, F.; Bai, Z.; Dong, Y.; Yang, J.; Liu, R.; Zou, B.; Li, J.; Zhong, H. *Adv. Optical Mater.* **2015**, *3*, 112–119.

[54] Schmidt, L. C.; Pertegás, A.; González-Carrero, S.; Malinkiewicz, O.; Agouram, S.; Espallargas, G. M.; Bolink, H. J.; Galian, R. E.; Pérez-Prieto, J. *J. Am. Chem. Soc.* **2014**, *136*, 850−853.

[55] Rong, Y.; Tang, Z.; Zhao, Y.; Zhong, X.; Venkatesan, S.; Graham, H.; Patton, M.; Jing, Y.; Guloy, A. M.; Yao, Y. *Nanoscale* **2015**, *7*, 10595–10599.

[56] Jeon, N. J.; Noh, J. H.; Kim, Y. C.; Yang, W. S.; Ryu, S.; Seok, S. I. *Nat. Mater.* **2014**, *13*, 897−903.

[57] Zhou, Y.; Game, O. S.; Pang, S.; Padture, N. P. *J. Phys. Chem. Lett.* **2015**, *6*, 4827−4839.

[58] Zheng, K.; Žídek, K.; Abdellah, M.; Messing, M. E.; Al-Marri, M. J.; Pullerits, T. *J. Phys. Chem. C* **2016**, *120*, 3077−3084.

[59] Huang, S.; Li, Z.; Kong, L.; Zhu, N.; Shan, A.; Li, L. *J. Am. Chem. Soc.* **2016**, *138*, 5749−5752.

[60] Gonzalez-Carrero, S.; Galian, R. E.; Pérez-Prieto, J. *J. Mater. Chem. A* **2015**, *3*, 9187–9193.

[61] Huang, H.; Zhao, F.; Liu, L.; Zhang, F.; Wu, X. −g.; Shi, L.; Zou, B.; Pei, Q.; Zhong, H. *ACS Appl. Mater. Interfaces* **2015**, *7*, 28128−28133.

Chapter 3: Development of Solution Processed Pb-free Chalcogenide Thin Film for Optoelectronic Application

3-1. Introduction

Metal chalcogenides with two-dimensional (2D) atomic layers are an emerging class of materials with rich optical and electronic properties.[1–3] Transition metal dichalcogenides such as WS_2, MoS_2, and $MoSe_2$ exhibit large charge carrier mobilities above 50 $cm^2\ V^{-1}\ s^{-1}$ in ambipolar field effect transistors (FETs)[4,5] and subthermionic tunneling behavior in FETs.[6] Besides, bismuth sulfide (Bi_2S_3) is potentially suitable for optoelectronic applications, owing to its significantly large Hall mobility (257 $cm^2\ V^{-1}\ s^{-1}$, a thermally-evaporated *n*-doped film)[7] and moderate bandgap of 1.3–1.6 eV[8,9] (dependent on the grain size and stoichiometry).[10]

Although there are several reports on Bi_2S_3-based photovoltaic cells[8,10,11–14] and photodetectors,[15,16] their widespread use and improved performance are limited by current film processing techniques, which require a trade-off between electronic and morphological qualities. As described in chapter 1, deposition using a colloidal nanoparticles (NPs)[8,10,11,12] suspension, chemical bath deposition (CBD),[17,18] successive-ionic-layer-adsorption-reaction (SILAR),[19,20] and spray pyrolysis (SP)[21,22] allow for the fabrication of smooth films over large areas, however the electronic properties are degraded by the small grain size and presence of impurities. By contrast, thermal decomposition of bismuth triethyldithiocarbonate ($Bi(EtXa)_3$) results in a highly-crystalline film,[23,24] though the film displays a mesoporous or nanorod morphology detrimental to long-range carrier transport. So far, a solution process that mitigates this trade-off has not yet been realized. Thermal evaporation yields a smooth but sulfur-poor film, giving a metallic bismuth or highly electron-doped Bi_2S_3 film ($10^{19}\ cm^{-3}$)[7] that can only be used as a negative electrode buffer.[14]

In this chapter, the effectiveness of a two-step technique for the facile fabrication of a Bi_2S_3 film involving spin-coating of a propionic acid (PA, CH_3CH_2COOH) solution of bismuth acetate ($Bi(OAc)_3$, OAc = CH_3COO^-) and thiourea ($CS(NH_2)_2$), followed by film crystallization under diluted H_2S gas is described. This sequential process was proposed to reconcile the current trade-off issue by separating the nucleation and growth steps. Hereafter, this process is referred to as a chemically-assisted spin-coat and crystallization (CASC) process. The morphology, optoelectronics, and other characteristics of a photoresistor device utilizing a CASC film were investigated and compared to those of similar devices prepared by conventional methods.

3-2. Results and Discussion

3-2-1. Development of chemically-assisted spin-coat and crystallization (CASC) process

A schematic of the CASC process is illustrated in Figure 3-1a. A mixture of $Bi(OAc)_3$ and thiourea in PA was found to be the most suitable precursor solution for the Bi_2S_3 CASC process, after performing rigorous combinatorial surveys of different solvents [*N*,*N*-dimethylformamide (DMF), dimethyl sulfoxide (DMSO), chlorobenzene, alcohol, carboxylic acid, and PA], bismuth sources [$Bi(OAc)_3$, $Bi(EtXa)_3$, bismuth nitric acid ($Bi(NO_3)_3$), $BiCl_3$, and BiI_3], and sulfur sources [thiourea and thiomalic acid]. Upon pre-thermal annealing of a spin-coated film at 150 °C for 50 s, thiourea is decomposed to gaseous CS_2, H_2NCN, NH_3, HNCS, and H_2S,[25,26] and the sulfur-containing compounds react with $Bi(OAc)_3$. The CASC process involved introducing a moderate number of seed

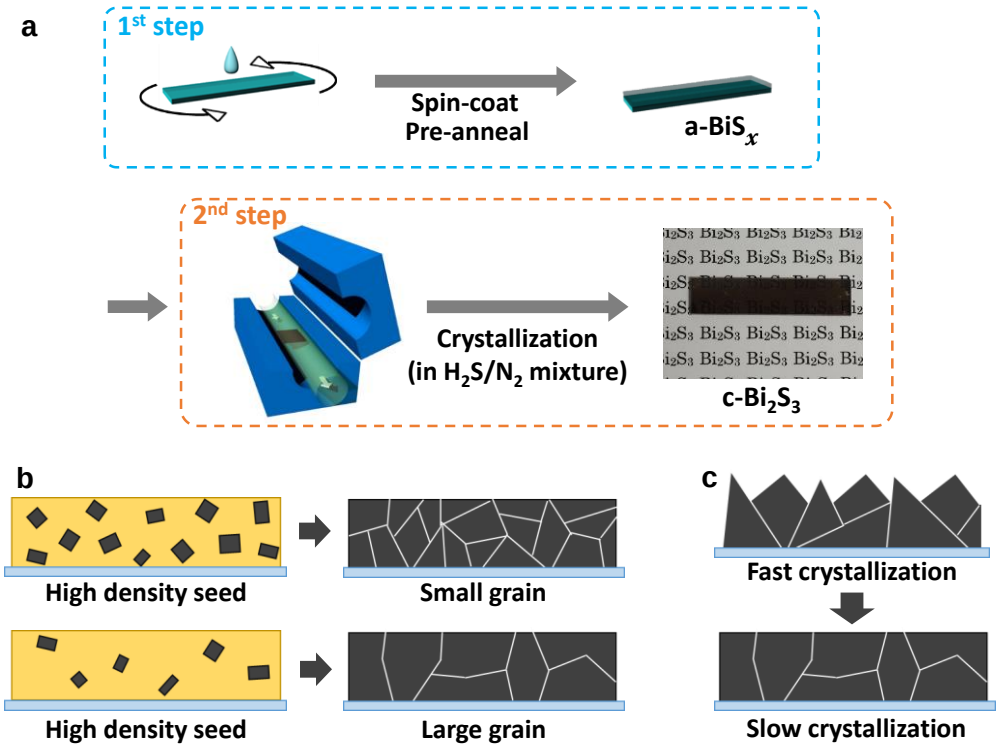

Figure 3-1. Schematics of CASC process. (a) Two-step CASC process. a-BiS_x and c-Bi_2S_3 represent amorphous and crystalline films after pre-thermal annealing and crystallization, respectively. Picture of the film is given. (b) Schematic showing how the seed crystal density affects the grain size. (c) Schematic showing the effect of the crystallization speed. Slow crystallization (right) prevents disordered crystal growth, resulting in a smooth surface.

crystals, as an excessive number would yield small-sized grains (Figure 3-1b). The resulting film was mostly amorphous (a-BiS_x) without complete conversion to a crystalline phase, despite the presence of B_2S_3 seed crystals inside the film. This was confirmed by the pale brown color and weak X-ray diffraction (XRD) pattern (*vide infra*) of a-BiS_x. As reported for a bismuth-thiourea-chloride complex of ($Bi[CS(NH_2)_2]_3Cl_3$),[27] a similar complex with a reduced thiourea stoichiometry (*vide infra*) was presumably formed in the precursor solution. The lower crystallinity of the complex allowed for spin-coating of a smooth amorphous film.

The a-BiS_x film was crystallized at an elevated temperature of 310 °C in a H_2S/N_2 gas mixture. During ~30 min of gas-phase crystallization, the film was gradually converted to a multi-crystalline smooth Bi_2S_3 thin film (see image in Figure 3-1a, c). The grain size was strongly dependent on the stoichiometry of the precursor solution, and $Bi(OAc)_3$:thiourea in a 1:1.1 ratio was found to be optimal, while a 1:1.5 ratio yielded only small grains (Figure 3-2). In addition to the stoichiometry of $Bi(OAc)_3$ and thiourea (1:0.5–1.6), the following parameters were also examined: the environment (in air or a N_2-glovebox), concentration (0.04–0.15 mol dm^{-3}), temperature (120–165 °C), and time (20-120 s) of pre-thermal annealing; crystallization temperature of the furnace (280–360 °C); number of spin-coating steps (1–5); and H_2S/N_2 gas temperature (25–260 °C) (see Experimental). During the optimization process, photoconductivity transients obtained by electrode-less flash-photolysis time-resolved microwave conductivity (TRMC) measurements served as an intuitive guide of the optoelectronic properties of the films.[28] Among the parameters listed above, the precursor stoichiometry and temperature had the largest impact on the TRMC transients. It should be noted that the CASC process is widely applicable to various substrates, including quartz, glass, silicon

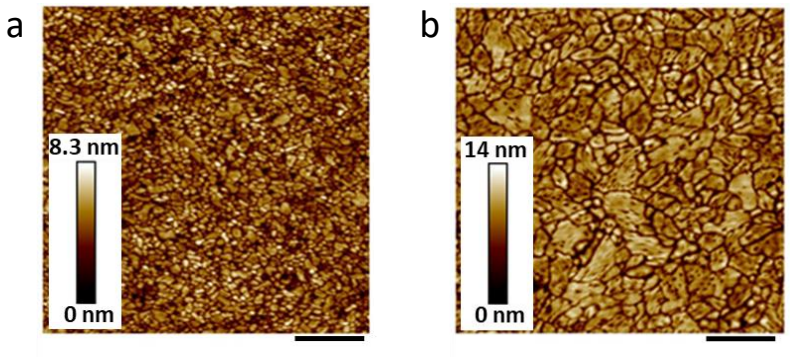

Figure 3-2. AFM images of CASC-processed Bi_2S_3 thin film obtained from different composition of the precursor. $Bi(OAc)_3$: thiourea = (a) 1 : 1.5 and (b) 1 : 1.1.

wafers with/without UV-ozone treatment, and mesoporous (mp-)TiO_2, whereas the SILAR process requires a coarse surface such as mp-TiO_2 for deposition.

X-ray photoelectron spectroscopy (XPS) of the optimized Bi_2S_3 film revealed peaks attributable to Bi 6s and S 2s orbitals (Figure 3-3), in agreement with previous reports.[7, 14,24] The calculated elemental ratio (Bi:S = 39.84:60.16) was in good agreement with the stoichiometry of Bi_2S_3, and no oxygen or nitrogen peaks were detected. Thus, the XPS results confirmed the high purity of CASC-processed Bi_2S_3.

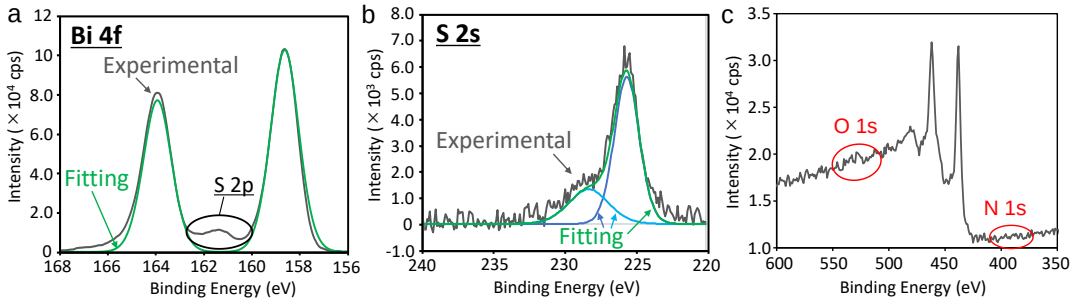

Figure 3-3. XPS spectra of CASC-processed Bi_2S_3 at (a) Bi 4f orbital, (b) S 2s orbital, and (c) O and N 1s orbital. The fitting curves are drawn along with experimental data. The ratio of Bi : S was calculated as 39.84 : 60.16, mostly identical to the theoretical stoichiometry of Bi_2S_3. No peak attributed to oxygen or nitrogen are not observed.

3-2-2. Structural orientation and morphology

Figure 3-4a shows XRD pattern of as-received Bi_2S_3 powder, a pre-thermally-annealed film (a-BiS_x), and a CASC-processed film (c-Bi_2S_3). A dramatic change from an amorphous to a highly-crystalline film was observed after gas-phase crystallization. The CASC film showed the most intense, sharp XRD pattern of all the films (Figure 3-4a, b). The correlation length of the crystallite at the (2 0 0) [15,24] peak (*d*-spacing = 0.56 nm) calculated using the Scherrer equation was largest for the CASC film (24 nm, Table 3-1). Interestingly, 2D-grazing incidence X-ray diffraction (2D-GIXD) results of the CASC film showed a more intense diffraction of the (2 0 0) peak in the out-of-plane direction than the in-plane direction (Figure 3-4c, d). These XRD results showed that the CASC film had a higher degree of 2D layer-stacking than did those prepared by other methods ($Bi(EtXa)_3$ and NPs). This is likely due to the slow, thermodynamically-favored

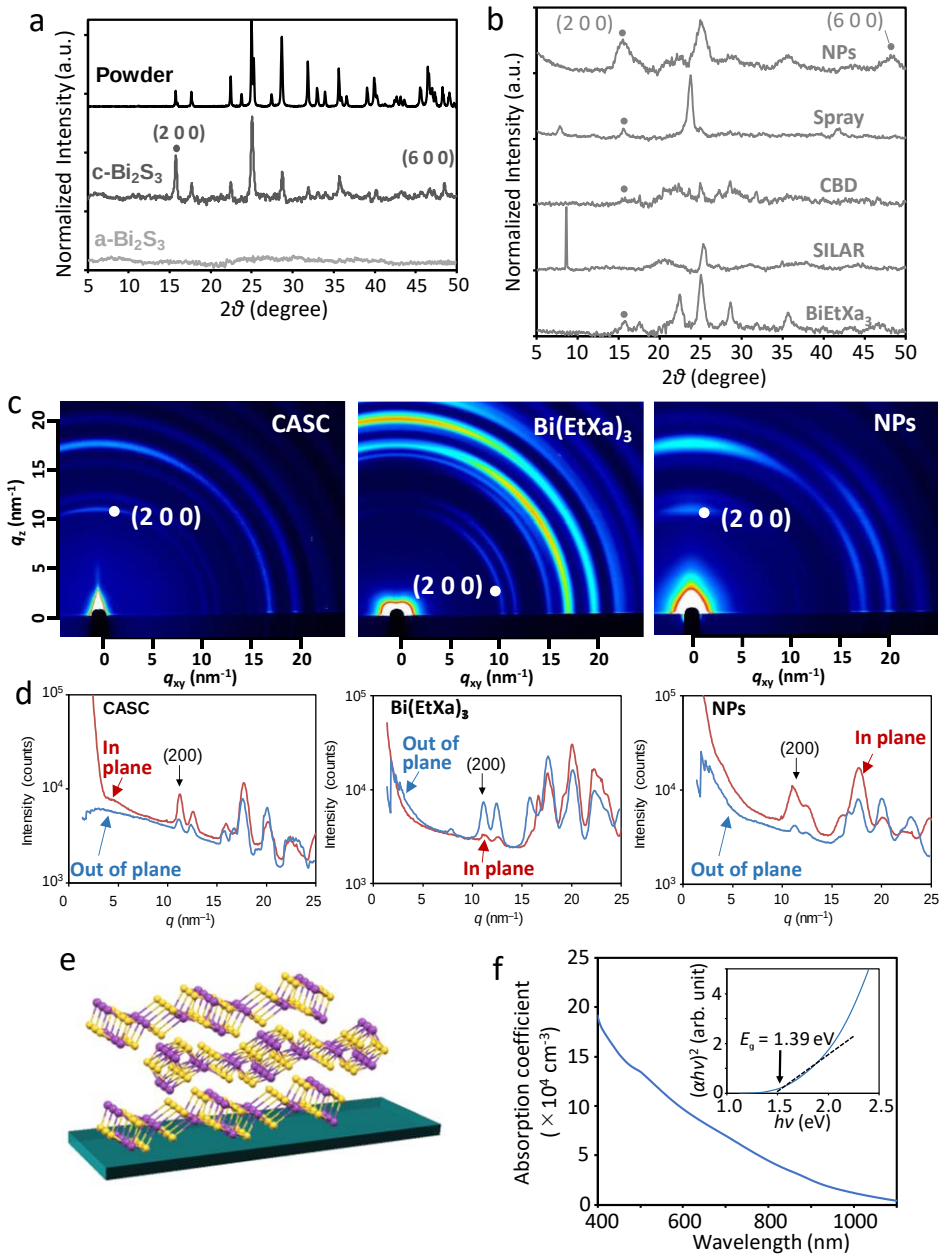

Figure 3-4. Crystallographic evaluations of Bi_2S_3 films. (a) PXRD pattern of Bi_2S_3 powder, Bi_2S_3 films after pre-thermal annealing (a-BiS_x), and after crystallization (c-Bi_2S_3) in CASC process. The dots represent the (2 0 0) diffraction. (b) PXRD patterns of Bi_2S_3 films prepared by NPs spincoat, SP, CBD, SILAR, and $Bi(EtXa)_3$ spincoat. (c, d) 2D-GIXD images and profiles of Bi_2S_3 films prepared by CASC, $Bi(EtXa)_3$, and NPs. The white dots represent the (2 0 0) diffraction. q_{xy} and q_z are the scattering vectors along the xy and z planes, respectively. (e) Schematic of the stacked layer structures of Bi_2S_3. (f) UV−vis absorption spectra of a CASC-Bi_2S_3 film. The inset is the Tauc plot to evaluate the band gap.

growth of 2D layers during crystallization of the CASC film. The observed layer structure illustrated in Figure 3-4e would merit charge carrier transport in the horizontal direction, as in a MoS_2-based FET device.[29,30] An ultraviolet (UV)-visible absorption spectrum of the Bi_2S_3 film displayed a broad feature extending to ~925 nm, the Tauc plot onset of which indicated a 1.39 eV bandgap (Figure 3-4f). The linear absorption coefficient at 900 nm and Urbach tail energy were 1.7×10^4 cm^{-1} (for either a direct[8,31] or indirect[9] transition) and 0.14 eV, respectively, which were inferior to those of LHPs (>10^4 cm^{-1} and ~15 meV, respectively)[32], however the wide coverage in the visible light region is promising for optoelectronic device applications.

Table 3-1. Summary of morphology and photoresistor output of Bi_2S_3 films.

Method	Morphology		
	Grain size (nm) [a]	R_a (nm) [a]	Correlation length (nm)[b]
CASC	50–300	1.7	23.7
$Bi(EtXa)_3$	50 × 400	47.3	17.4
CBD	20–40	29.1	1.2
SILAR	10–30	10.8	1.9
SP	40–200	52.2	21.7
NPs	5–20	3.5	7.3

[a] Evaluated from AFM height images of 2 × 2 or 1 × 1 μm^2. [b] Evaluated from the (2 0 0) peaks of XRD patterns using the Scherrer relation.

The most pronounced effect observed for the CASC process was the improved AFM morphology (see Figure 3-5), which showed large, closely-packed crystal grains (with size L = 50–400 nm) with a root-mean-square surface roughness (R_a) as small as 1.7 nm (Table 3-1). This was in sharp contrast to the trade-off observed in Bi_2S_3 films prepared by conventional techniques; for NPs, a small R_a of 3.5 nm accompanied a small L of 5–20 nm, while for $Bi(EtXa)_3$ and SP, a large L (partly rod-like shapes) up to 400–500 nm gave a large R_a of 40–50 nm (Figure 3-5, Table 3-1). This was due to the two-step CASC process, consisting of amorphous film formation with a low seed level followed by slow crystallization, enabling separation of the nucleation and growth processes, which often occur simultaneously and uncontrollably. A SILAR-processed film exhibited a moderate L of 20–40 nm and R_a of 11 nm, however its inferior photoresponse associated with low crystallinity is a critical drawback for device applications.

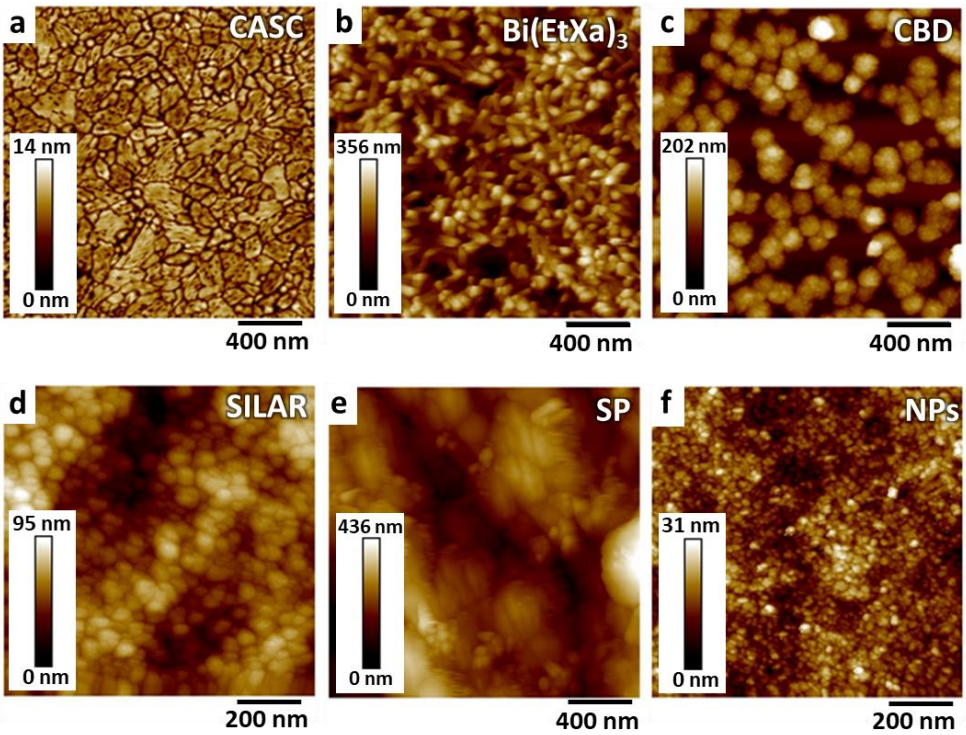

Figure 3-5. AFM images of Bi_2S_3 films prepared by (a) CASC process, (b) $Bi(EtXa)_3$ spin-coating, (c) CBD, (d) SILAR, (e) SP, and (f) NPs. Note that the scale of figure (d) and (f) (a bar = 200 nm) is smaller than others (a bar = 400 nm), because of the small crystal grains.

3-2-3. Optoelectronic properties of Bi_2S_3 thin films prepared by various process

The TRMC photoconductivity of Bi_2S_3 films prepared by CASC and other methods were measured (Figure 3-6a, b). The optimized CASC film showed a $\phi\Sigma\mu$ (see eq. 1-5 in Chapter 1) maximum ($\phi\Sigma\mu_{max}$) of 1.3 ± 0.3 $cm^2\ V^{-1}\ s^{-1}$ at a reduced excitation light density (10^{12} photons $cm^{-2}\ pulse^{-1}$) (Figure 3-6c, d). High $\phi\Sigma\mu_{max}$ values of 1.65 and 0.95 $cm^2\ V^{-1}\ s^{-1}$ were also observed in the film from $Bi(EtXa)_3$ and as-received powder, respectively. In fact, the large TRMC signal observed for the powder sample was the basis of the initial motivation for developing the CASC process. The comparable $\phi\Sigma\mu_{max}$ values of these films showcase their excellent optoelectronic response, consistent with the observed high crystallinities and large grain sizes. In contrast, the $\phi\Sigma\mu_{max}$ values of films prepared by CBD, SILAR, SP, and NPs were two orders of magnitude smaller (< 10^{-2}

$cm^2\ V^{-1}\ s^{-1}$) than that of the CASC film. The low crystallinity and small grains comprising many lattice defects and/or impurities accounted for the low TRMC signals. Note that TRMC evaluation of a thermally-evaporated film failed, due to its extremely high steady-state conductivity arising from the inclusion of metallic bismuth. The $\phi\Sigma\mu$ transients were also analyzed using a double exponential function. Analysis of the effective lifetime (τ) demonstrated that $Bi(EtXa)_3$ and CASC films had longer τ values (20 and 13 μs, respectively) than the others (4.0–9.5 μs, Figure 3-6b). The short τ values of Bi_2S_3 prepared by other methods was likely due to degradation by carrier trapping in small-sized grains with high levels of impurities. Meanwhile, the high $\phi\Sigma\mu$ and long τ values observed for $Bi(EtXa)_3$ and CASC films appeared to be suitable for optoelectronic devices.

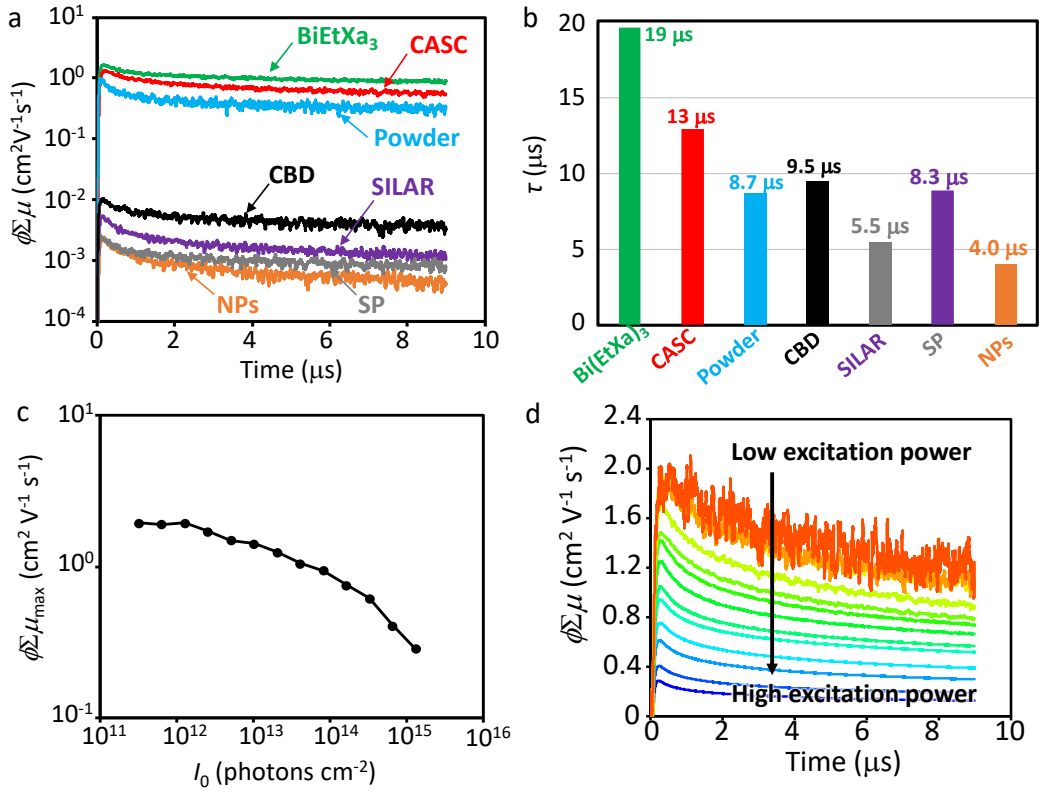

Figure 3-6. Comparative evaluation of Bi_2S_3 using the TRMC technique. (a) TRMC transients of each sample (λ_{ex} = 500 nm, $I_0 = 10^{13}$ photons cm^{-2}). (b) Effective lifetimes (τs) of the TRMC decays obtained by analysis with a double-exponential function: $A_1\exp(-k_1t) + A_2\exp(-k_2t)$, $\tau = (A_1(k_1)^{-1} + A_2(k_2)^{-1})(A_1 + A_2)^{-1}$. (c) Dependence of TRMC transint maxima ($\phi\Sigma\mu_{max}$) of CASC-Bi_2S_3 on the excitation intensity (I_0). (d) The kinetics at $I_0 = 10^{11}$ photons cm^{-2} to $I_0 = 10^{15}$ photons cm^{-2}. λ_{ex} = 500 nm.

Long-range carrier transport in a device, which is complementary to the local charge carrier dynamics evaluated by electrode-less TRMC, is another crucial aspect. Thus, transient photocurrent (TPC) evaluations were performed in a simple device with two gold electrodes. Upon exposure to a nanosecond laser, the TPC intensity linearly increased with the applied bias (1–10 V), indicating ohmic contact between Bi_2S_3 and the electrodes (Figure 3-7a–d). The schematics of TPC measurement is represented in Figure 3-7a. Interestingly, the TPC transients showed very slow decay rates of the order of several milliseconds, regardless of the preparation method. This was in contrast to the fast

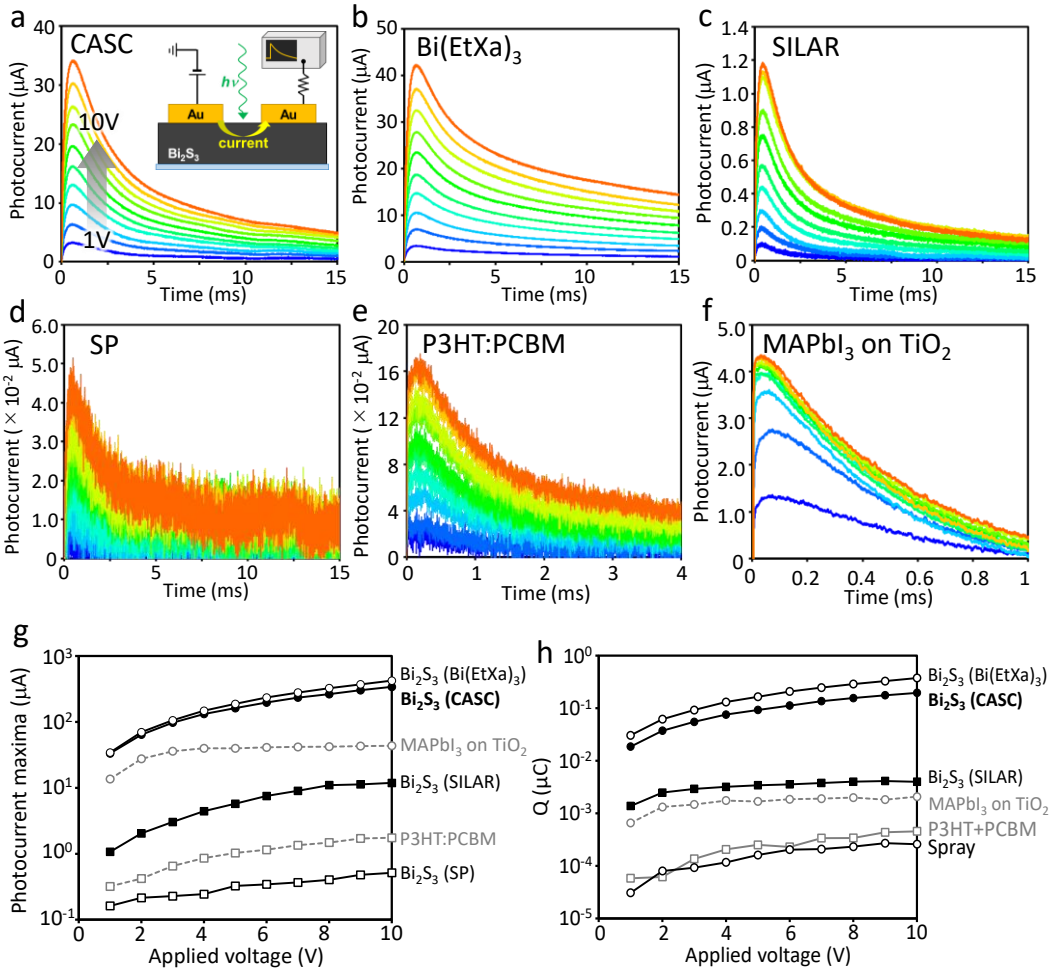

Figure 3-7. TPC transients of Bi_2S_3 films (prepared by (a) CASC, (b) $Bi(EtXa)_3$, (c) SILAR, and (d) SP), (e) P3HT:PCBM, and (f) $MAPbI_3$ on mp-TiO_2 with the applied bias of 1–10 V. The inset is a schematic of a photoresistor device (the gap length is 0.5 mm). λ_{ex} = 355 nm. Dependence of the (g) TPC maxima and (h) the number of charge (Q) calculated by integrating TPC transients over the time on the applied voltage for Bi_2S_3 thin films ($Bi(EtXa)_3$, CASC, SILAR, and SP), P3HT:PCBM, and $MAPbI_3$ on mp-TiO_2.

TPC decay (0.41–1.1 ms) of emerging photovoltaic materials; a blend of regioregular poly(3-hexylthiophene) (P3HT) and [6,6]-phenyl-C_{61}-butyric acid methyl ester (PCBM) and a film of methylammonium cation ($CH_3NH_3^+$, MA) lead iodide perovskite ($MAPbI_3$) on mp-TiO_2 (Figure 3-7e, f). The slow TPC decay of Bi_2S_3 was in line with the TRMC transients showing retarded charge recombination and slow relaxation (trapping). Most importantly, $Bi(EtXa)_3$ and CASC films demonstrated the highest TPC maxima over the entire applied bias; 2–3 orders of magnitude higher than those of P3HT:PCBM and Bi_2S_3 prepared by SILAR and SP, and 10-fold higher than that of $MAPbI_3$ on mp-TiO_2 (Figure 3-7g). TPC evaluations of Bi_2S_3 devices fabricated using CBD and NPs were not possible because of the large dark current due to excessive doping and low conductivity, respectively. The number of charges calculated by integrating the TPC over the elapsed time highlighted the superiority of $Bi(EtXa)_3$ and CASC over the others (Figure 3-7h).

3-2-4. Temperature-dependent measurements on CASC-processed Bi_2S_3 film

To further understand the charge carrier transport mechanism in a CASC-Bi_2S_3 film, the temperature dependence of the TRMC (Figure 3-8a, c) and TPC (Figure 3-8b, d) was evaluated. With decreasing temperature, $\phi\Sigma\mu_{max}$ increased according to $T^{-1.5}$ at 290–252 K, then decreased at 252–122 K. This indicated that the charge carriers obeyed band transport governed by phonon scattering near room temperature and hopping transport at low temperature, with activation energies (E_a) of 140 meV (252–202 K) and 17 meV (202–122 K) obtained via following Arrhenius equation (3-1);

$$\mu = A\exp\left(-\frac{E_a}{kT}\right) \qquad (3\text{-}1)$$

where μ is charge mobility, A is scaling factor, and k is Boltzmann constant. The $T^{-1.5}$ dependence at room temperature was consistent with the relatively large TRMC mobility (1.3 ± 0.3 cm^2 V^{-1} s^{-1}, assuming $\phi = 1$). The same trends were observed in the temperature-dependent TPC, showing identical local and long-range carrier transport mechanisms. Remarkably, Hall effect measurements at room temperature revealed a moderate electron mobility of 7.2 ± 2.3 cm^2 V^{-1}s^{-1} along with an electron density (n) of $(1.3 \pm 0.3) \times 10^{14}$ cm^{-3} for the CASC film. n was five orders of magnitude lower than that of a thermally-evaporated Bi_2S_3 film,[7] which is beneficial for dark current reduction in a device.

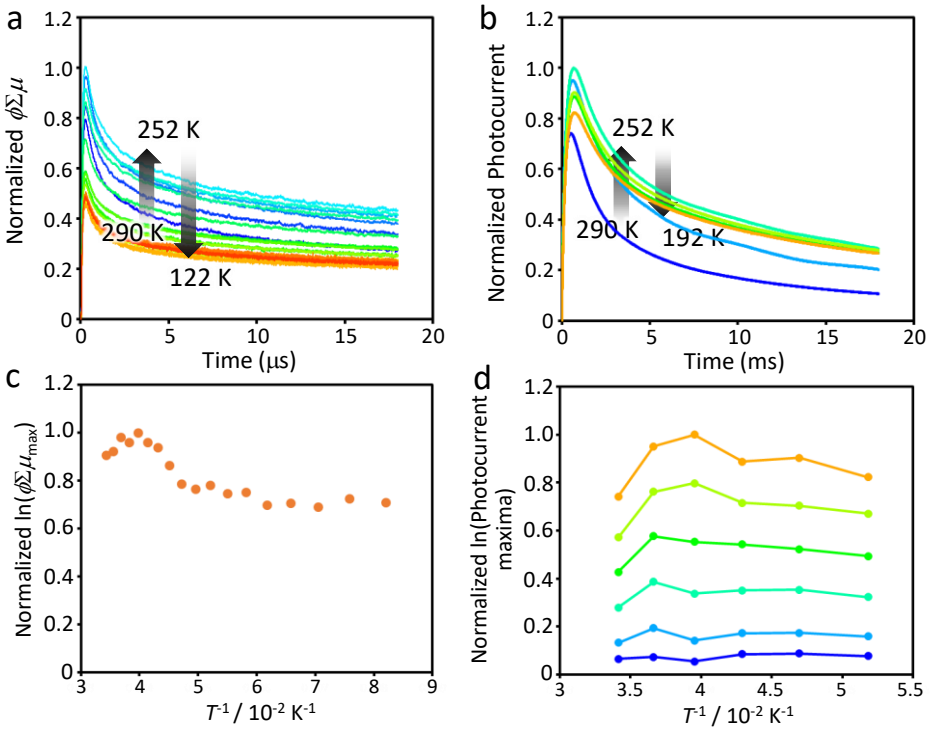

Figure 3-8. (a) TRMC and (b) TPC transients at low temperature. The colors and the arrows represent the decrease of the temperature. λ_{ex} = 355 nm. Temperature dependence of (c) normalized TRMC maxima ($\phi\Sigma\mu_{max}$) and (d) TPC maxima obtained from a) and b), respectively.

3-2-5. Evaluation of photosensing property

Motivated by the observed heightened photoresponsivity of CASC-Bi_2S_3, it was utilized as photoresistor, a device used to detect steady-state light (sunlight or room light) by the change in conductance, allowing for automatic control of on-off switching of an external device such as a street light. A photoresistor has a simple device structure similar to that shown in Figure 3-7a (a commercial device has a pair of winding stripes to increase conductance). CdS has been widely used as the active layer, though the toxicity of Cd is a common issue, over which Bi_2S_3 has a great advantage. The author evaluated current (I)-voltage (V) curves of a CASC-Bi_2S_3 photoresistor with/without exposure to pseudo-sunlight (AM 1.5 G, 100 mW cm^{-2}) or ambient room light from fluorescence tubes (Figure 3-9a). The photoconductance (ΔG) and on-off ratio (the ratio of conductance with/without light) were measured from the slope of the I-V curve and compared to other

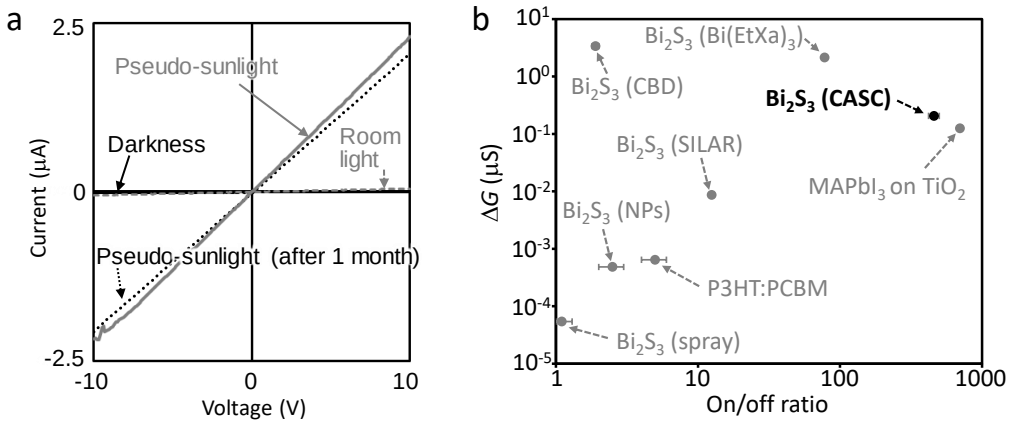

Figure 3-9. Photoresistor characterization. (a) $I-V$ curves of a CASC-Bi_2S_3 film (gray solid line: photocurrent under pseudosunlight; gray dot line: photocurrent under room light; black solid line: dark current; black dot line: photocurrent under pseudosunlight after 1 month aging). (b) Plots of the photoconductance (ΔG) and on/off ratio of Bi_2S_3 films prepared by various methods. Those of P3HT:PCBM and $MAPbI_3$ on mp-TiO_2 are also shown.

samples (Figure 3-9b). The obtained average ΔG and on/off ratio of the CASC-Bi_2S_3 photoresistor were as large as 0.21 μS and 4.6×10^2, respectively - several orders of magnitude larger than those of other Bi_2S_3 and P3HT:PCBM photoresistors (Table 3-2). The low ΔG and on/off ratio of P3HT:PCBM photoresistors are considered as a result of insufficient charge separation due to low electric field intensity (~200 V / cm) in photoresistor device. The CASC photoresistor exhibited high sensitivity even for room light, with an on/off ratio of 8. Although a $MAPbI_3$ photoresistor performed similarly to the CASC photoresistor (ΔG ~0.12 μS and on-off ratio ~7.0×10^2), the excellent stability of CASC-Bi_2S_3 allowed the initial performance to be retained even after storage in air for one month (Figure 3-9a). Although $Bi(EtXa)_3$ and CBD films showed larger ΔG values than did a CASC film, their on-off ratios were 1–3 orders of magnitude lower, due to the large dark current. In contrast, the CASC film achieved both large photoconductance and high on-off ratio, making them most suitable for light sensing applications.

Upon periodic illumination (515 nm, ~1 Hz), CACS-Bi_2S_3 exhibited good photoswitching with the prompt rise and slow decay times of 0.02 and 0.06 s, respectively (Figure 3-10, the former is close to the instrumental response function). The figures-of-merit of photodetector, i.e. responsivity (R), external quantum efficiency (EQE), and detectivity (D^*) were evaluated for the Bi_2S_3 photoresistors according to the reported procedure (see Experimental).[29] Although the R (2.4×10^{-3} A W^{-1}) and EQE (0.58%) of

CASC-Bi_2S_3 were lower than those of $Bi(EtXa)_3$ film (R = 5.4 × 10^{-2} A W^{-1}, EQE =13%) due to the lower photocurrent (Table 3-2), D^* of the former was much larger than that of the latter owing to the excellent on/off ratio. Note that R, EQE, and D^* are dependent on the applied bias, wavelength, and light power density,[29,30] in particular, the gap length of electrodes. Nonetheless, the large D^* (1.7 × 10^{11} Jones) of CASC-Bi_2S_3 comparable to

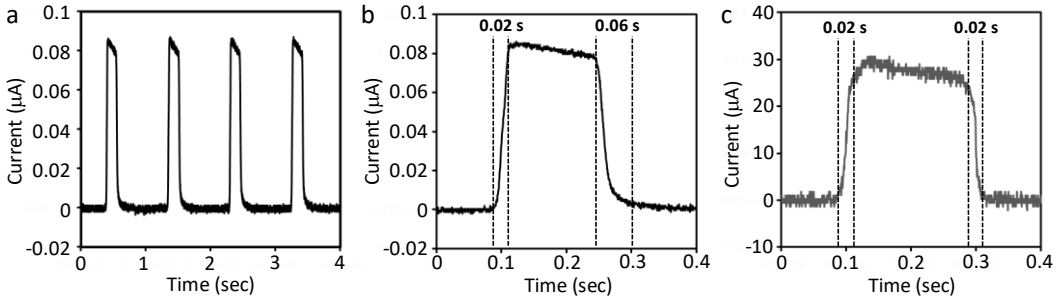

Figure 3-10. (a) Photoresponse of the CASC-Bi_2S_3 photoresistor upon exposure to a CW laser (λ = 515 nm) through a mechanical chopper (~1 Hz). A termination: 50 Ω. (b) Expanded signal of the photoresponse. (c) Photoresponse of a Si photodiode, which can be assumed as an instrumental response function (the rise and decay of signals are caused by the edge part of chopper slit, not due to the response time of a Si photodetector). A termination: 50Ω.

Table 3-2. Summary of photoresistor output (photoconductance (ΔG), on-off ratio, responsivity, external quantum efficiency (EQE), and detectivity (D^*)) of Bi_2S_3 films.

Method	ΔG (μS) [a]	On/off ratio [a]	Responsivity (A W^{-1}) [b]	EQE (%) [b]	D^* (10^{10} Jones) [b,c]
CASC	2.1×10^{-1}	460	2.4 × 10^{-3}	0.58	17
$Bi(EtXa)_3$	2.1	78	5.4 × 10^{-2}	13	6.4
CBD	3.4	1.9	8.9 × 10^{-2}	21	1.3
SILAR	8.7×10^{-3}	12.5	1.4 × 10^{-3}	0.34	1.2
SP	4.8×10^{-4}	2.5	1.1 × 10^{-4}	2.7 × 10^{-2}	2.6
NPs	5.4×10^{-5}	1.1	2.9 × 10^{-5}	7.0 × 10^{-3}	1.3

[a] Evaluated from the slope of the I–V curves of photoresistors under pseudo-sunlight (AM 1.5 G, 100 mW cm^{-2}). [b] Evaluated from the currents of photoresistors at 10 V with/without monochromatic light (512 nm, 0.95 mW cm^{-2}). The gap distance and length of electrodes were 0.5 mm and 3 mm, respectively. Note that responsivity and EQE are varied by the gap distance, the light wavelength, and the light power density. [c] 1 Jones = 1 cm $Hz^{1/2}$ W^{-1}

the reports found in high-sensitive heterojunction Bi_2Te_3 photodetectors (10^{10}–10^{11} Jones)[29,30,33] is notable.

Solution-processable bismuth-based semiconductors have emerged as viable alternatives to lead-based photovoltaics. These include $MA_3Bi_2I_9$ processed from DMSO,[34] $AgBi_2I_7$ from *n*-butylamine,[35] and colloidal nanocrystals of $AgBiS_2$ from toluene,[36] which reportedly show PCEs of 1, 1.2, and 6.3%, respectively. Antimony chalcogenides of Sb_2S_3 prepared by CBD (PCE = 7.5%)[37] and thermally-evaporated Sb_2Se_3 (PCE = 5.6%)[38] are notable analogues of Bi_2S_3. The author applied a preliminary CASC process to lead sulfide (PbS) and obtained a film with large grains (~100 nm), a small R_a (6.3 nm), and a large TRMC signal ($\phi\Sigma\mu_{max}$ of 0.45 $cm^2\ V^{-1}s^{-1}$), comparable to those of Bi_2S_3 (Figure 3-11). Therefore, the CASC process shows great promise for advanced solution-processed metal sulfide semiconductors.

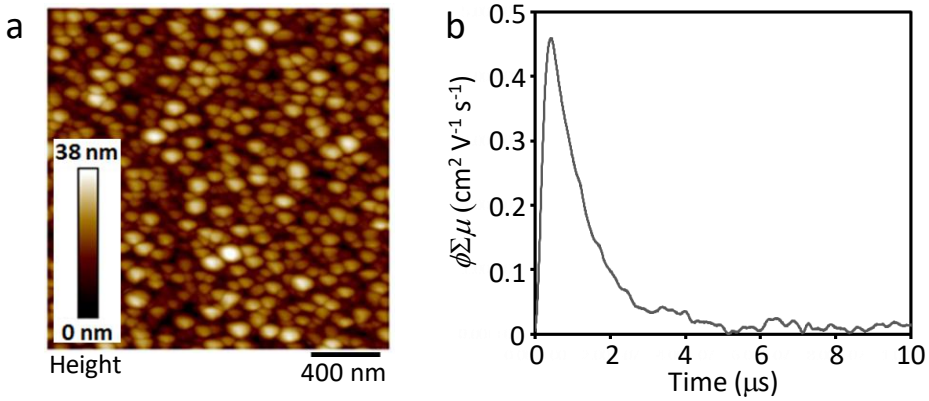

Figure 3-11. (a) AFM image of the PbS film. R_a = 6.3 nm. (b) TRMC transient of a PbS film prepared by CASC process.

3-3. Conclusion

In conclusion, the author successfully developed a CASC process for the preparation of high quality Bi_2S_3 thin films, consisting of facile spin-coating and crystallization steps. Thiourea was used in the precursor solution as a sulfurization source upon pre-thermal annealing, as well as a chemical mediator to fabricate a smooth, amorphous film with the lack of sulfur. Subsequent gas-phase crystallization lead to a high degree of crystallinity and purity with the expected elemental stoichiometry and a 2D layer-stacked structure. Importantly, the CASC process simultaneously achieved excellent film morphology (low surface roughness and large grain size), high TRMC/TPC signal strength with band transport at room temperature, and moderate Hall effect electron mobility. The CASC photoresistor demonstrated superior performance (photoconductance, on-off ratio, and detectivity) over other Bi_2S_3 devices prepared by conventional methods. The high stability and non-toxicity are also attractive features, making the CASC method promising for fabricating optoelectronic devices from metal sulfide materials.

3-4. Experimental

Materials and general measurements

$Bi(OAc)_3$, $Bi(NO_3)_3$, BiI_3, and $BiCl_3$ were purchased from Sigma-Aldrich. Thiourea and propionic acid were purchased from Tokyo Chemical Industry. Super dehydrated grade DMSO and toluene were purchased from Wako Chemical Industries Ltd. These chemicals were used without further purification. Steady-state photoabsorption spectroscopy was performed using a Jasco V-730 UV−vis spectrophotometer. PYS experiments were performed using a Bunko Keiki BIP-KV202GD. AFM observations and thickness measurements were performed using a Bruker Innova and a Bruker Dektak XT, respectively. XPS evaluations were performed using a Shimadzu AXIS-165x. XRD data were collected on a Rigaku MiniFlex-600 instrument using Cu K_α radiation (λ = 1.54187 Å) at room temperature in air. 2D-GIXD experiments were conducted on the BL46XU beamline at SPring-8 (Japan Synchrotron Radiation Research Institute, JASRI), using 12.39 keV (λ = 1 Å) X-rays. Hall effect mobilities were evaluated using a Toyo Resitest8303 and the van der Pauw method under an applied magnetic field of 0.66 T in air at room temperature. The Hall carrier concentration (n) and Hall mobility (μ) were calculated from the Hall coefficient (R_H) by assuming a single-band model and a Hall factor of 1, i.e. $n = (eR_H)^{-1}$ and $\mu = \sigma R_H$, where e is the elementary charge and σ is the conductivity.

Preparation of CASC-Bi_2S_3 films and other films

The optimized CASC process was performed as follows: $Bi(OAc)_3$ (0.1 M) and thiourea (0.11 M) were dissolved in propionic acid and stirred for 30 min at 50 °C. This precursor solution was then filtrated (0.20 μm), spin-coated (2500 rpm, 20 s) onto a cleaned substrate after UV-ozone treatment (10 min), and subjected to pre-thermal annealing at 150 °C for 50 s. The spin-coating and annealing steps were repeated three times to produce a film with a thickness of 60 nm. These processes were performed in a N_2 glovebox (O_2 < 0 ppm, H_2O < 0.0 ppm). The obtained film was then transferred into a glass pipe chamber (3.0 cm in inner diameter, 40 cm in length) equipped with a cylindrical muffle heater and thermally annealed (with a heater temperature of 330 °C and measured substrate temperature of 310 °C) under a flow of mixed gases (H_2S:N_2 =1:3) for 20 min. The gas flow was initiated when the chamber temperature reached 200 °C, with an initial flow rate of 300 mL min^{-1} for 2 min, followed by a decrease to 100 mL min^{-1}. Details on the gas flow and temperature are given in Figure 3-12. The optimization of each condition such as precursor composition, annealing temperature, etc. were conducted with TRMC

evaluation (Figure 3-13). PbS film was prepared by the same manner as Bi_2S_3. The precursor solution involved Pb acetate (0.1 M) and thiourea (0.11 M) dissolved in propionic acid. For comparative studies, Bi_2S_3 thin films were prepared according to reported procedures for SILAR,[19] CBD,[17] NPs,[10] $Bi(EtXa)_3$,[23] and SP[21]. These were deposited on a cleaned quartz substrate for TRMC or a cleaned glass substrate for TPC and photoresistors. Note that SILAR required an underlying mp-TiO_2 layer, as a film was not able to be formed on a bare substrate. A $MAPbI_3$ film (300 nm in thickness) was prepared on a mp-TiO_2 layer in a N_2 glovebox by spin-coating a 1.0 M DMSO solution, along with toluene anti-solvent treatment and thermal annealing at 110 °C for 10 min. A P3HT:PCBM = 1:1 (wt/wt) film (200 nm in thickness) was prepared by spin-coating (at 2000 rpm for 20 s, slope 2 s) a 1.5 wt% chlorobenzene solution. The film was thermally annealed at 150 °C for 10 min. All procedures were conducted in a N_2 glovebox.

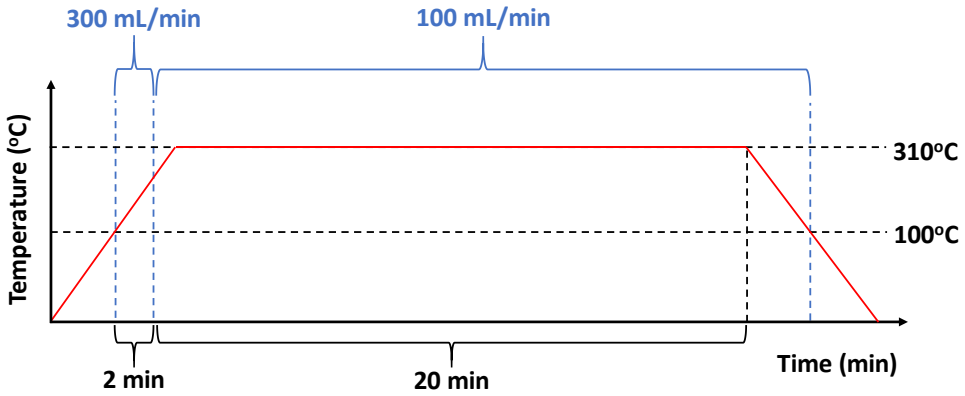

Figure 3-12. Profile of crystallization temperature and gas flow rate. Gas-flow rate (drawn by blue) was precisely controlled by using a mass-flow controller (KOFLOC; 8500MC-0-1-2). The heater temperature measured with a thermocouple is provided. The temperature of a substrate in a glass pipe chamber was measured to be 310 ºC when the heater temperature was 320 ºC. Before starting gas-flow, the glass pipe chamber was purged by nitrogen.

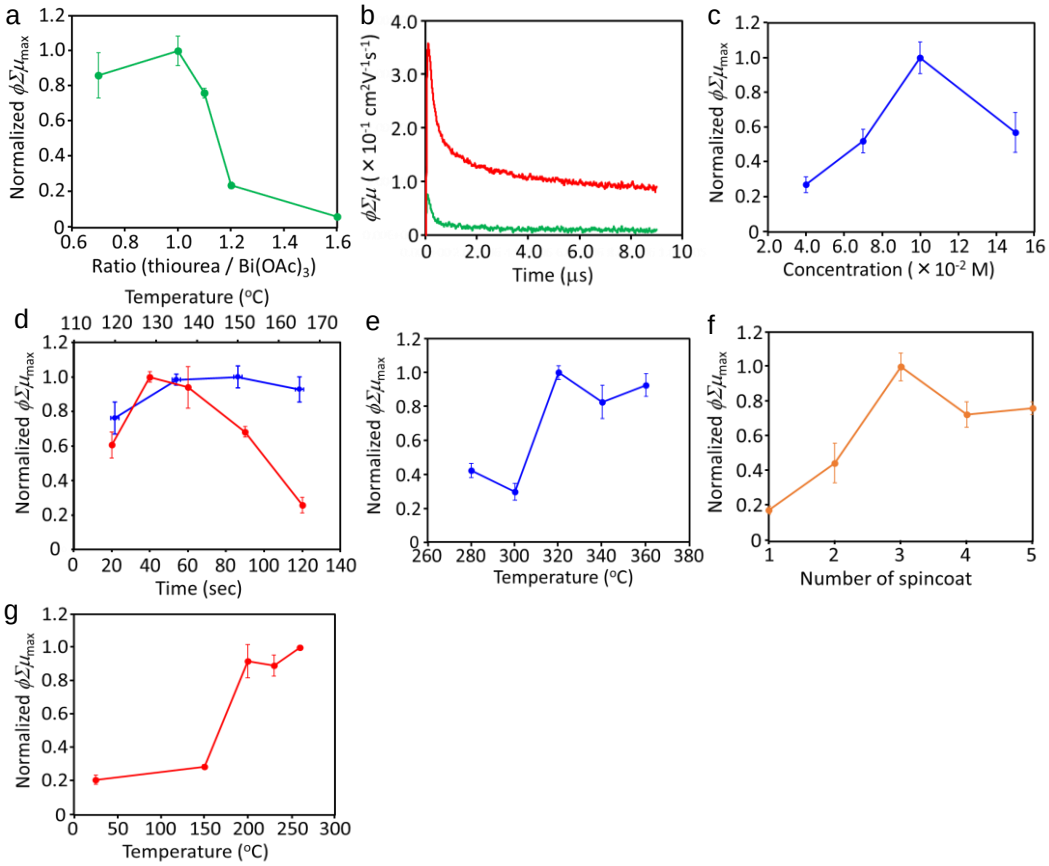

Figure 3-13. Screening of processing parameters by using TRMC. (a) The composition of precursor solution ($Bi(OAc)_3$: thiourea = 1:0.5–1.6), (b) environment of spin-coating and pre-thermal annealing (in the air or a N_2-glovebox), (c) the concentration (0.04–0.15 mol dm^{-3}), (d) temperature (120–165°C, blue line) and time (20–120 s, red line) of pre-thermal annealing, (e) crystallization temperature (280–360°C), (f) the number of spin-coating (1–5 times), and (g) the initial temperature to start flowing H_2S/N_2 gas (25–260°C).

Flash-photolysis TRMC

Thin films were prepared on a quartz plate. The sample was set in a resonant cavity and probed by continuous microwaves at ca. 9.1 GHz. The laser excitation from an optical parametric oscillator (OPO, Continuum Inc., Panther) seeded by third harmonic generation of a Nd:YAG laser (Continuum Inc., Surelite II, 5−8 ns pulse duration, 10 Hz) was set at 500 nm. The photon density (I_0) varied from 1.28×10^{11}–6.42×10^{14} photons cm^{-2} pulse^{-1}. The photoconductivity transient $\Delta\sigma$ was converted to $\phi\Sigma\mu$ via the eq. 1-5 in

Chapter 1. For low-temperature experiments, a cavity with a sample was set in a vacuum chamber with an electric cooler. Other experiments were conducted at room temperature in air.

TPC and photoresistor

The films were prepared on a cleaned glass substrate by the above-mentioned procedures (SILAR and $MAPbI_3$ films were prepared on mp-TiO_2/glass). A pair of rectangular gold electrodes (0.5 mm gap, 1 mm width and 3 mm length) was deposited through a shadow mask by thermal evaporation in a vacuum chamber (10^{-5} Pa). TPC transients induced by exposure to third-harmonic generation (THG: 355 nm) of a Nd:YAG laser (I_0 = 1.82 × 10^{13} photons cm^{-2} $pulse^{-1}$) were measured using an oscilloscope (Tektronix model DPO4000 with a 3 kΩ termination) under an external bias (0−10 V: 1 V steps) applied using a source meter (Keithley model 2612A). For the low-temperature experiments, a device was set in a vacuum chamber with an electric cooler. Other experiments were conducted at room temperature in air. Photoresponse under periodic illumination was measured using an oscilloscope and an attenuated CW laser (Spectra-Physics Inc., EXLSR-515-50S-W, 515 nm) through a mechanical chopper (~1 Hz). *I-V* curves of photoresistors (using the same device as for TPC measurements) were measured by sweeping the voltage (from −10 to +10 V) of the source meter under AM 1.5 G solar illumination at 100 mW cm^{-2} (1 sun, monitored by a calibrated standard cell, Bunko Keiki SM-250 KD) from a 300 W solar simulator (SAN-EI Corp., XES-301S). Responsivity (R), external quantum efficiency (EQE), and detectivity (D^*) were evaluated from the current of photoresistor at 10 V with/without monochromatic light (512 nm, 0.95 mW cm^{-2}) from a Xe lamp (Asahi Spectra Corp., MAX-303) through a band-pass filter ($\Delta\lambda$ = 7 nm). These parameters were calculated according to the report,[29] through $R = I_P (PA)^{-1}$, $EQE = (I_p hv)(qPA)^{-1}$, and $D^* = (AR (2qI_d)^{-1})^{1/2}$, where I_p is the photocurrent, I_d is the dark current, P is the light power density, A is the active area, h is the Planck constant, v is the photon frequency, and q is the elementary charge.

3-5. Reference

[1] Mitzi, D. B. *Adv. Mater.* **2009**, *21*, 3141–3158.

[2] Wang, Q. H.; Kalantar-Zadeh, K.; Kis, A.; Coleman, J. N.; Strano, M. S. *Nat. Nanotech.* **2012**, *7*, 699–712.

[3] Tan, C.; Lai, Z.; Zhang, H. *Adv. Mater.* **2017**, *29*, 1701392/1-25.

[4] Perera, M. M.; Lin, M. –W.; Chuang, H. -J.; Chamlagain, B. P.; Wang, C.; Tan, X.; Cheng, M. M.-C.; Tománek, D.; Zhou, Z. *ACS Nano* **2013**, *7*, 4449–4458.

[5] Kappera, R.; Voiry, D.; Yalcin, S. E.; Branch, B.; Gupta, G.; Mohite, A. D.; Chhowalla, M. *Nat. Mater.* **2014**, *13*, 1128 –1134.

[6] Sarkar, D.; Xie, X.; Liu, W.; Cao, W.; Kang, J.; Gong, Y.; Kraemer, S.; Ajayan, P. M.; Banerjee, K. *Nature* **2015**, *526*, 91–95.

[7] Song, H.; Zhan, X.; Li, D.; Zhou, Y.; Yang, B.; Zeng, K.; Zhong, J.; Miao, X.; Tang, J. *Sol. Energy Mater. Sol. Cells* **2016**, *146*, 1–7.

[8] Martinez, L.; Bernechea, M.; De Arquer, F. P. G.; Konstantatos, G. *Adv. Energy Mater.* **2011**, *1*, 1029–1035.

[9] Al-Douri, A. A. J.; Madik, M. P. *Renewable Energy* **2000**, *21*, 411–416.

[10] Bernechea, M.; Cao, Y.; Konstantatos, G. *J. Mater. Chem. A* **2015**, *3*, 20642–20648.

[11] Rath, A. K.; Bernechea, M.; Martinez, L.; Pelayo Garcia De Arquer, F.; Osmond, J.; Konstantatos, G. *Nat. Photonics* **2012**, *6*, 529–534.

[12] Martinez, L.; Stavrinadis, A.; Higuchi, S.; Diedenhofen, S. L.; Bernechea, M.; Tajima, K.; Konstantatos, G. *Phys. Chem. Chem. Phys.* **2013**, *15*, 5482–5487.

[13] Lindblad, R.; Cappel, U. B.; O'Mahony, F. T. F.; Siegbahn, H.; Johansson, E. M. J.; Haque, S. A.; Rensmo, H. *Phys. Chem. Chem. Phys.* **2014**, *16*, 17099–17107.

[14] Li, D.-B.; Hu, L.; Xie, Y.; Niu, G.; Liu, T.; Zhou, Y.; Gao, L.; Yang, B.; Tang, J. *ACS Photonics* **2016**, *3*, 2122–2128.

[15] Konstantatos, G.; Levina, L.; Tang, J.; Sargent, E. H. *Nano Lett.* **2008**, *8*, 4002–4006.

[16] Yu, H.; Wang, J.; Wang, T.; Yu, H.; Yang, J.; Liu, G.; Qiao, G.; Yang, W.; Cheng, X. *CrystEngComm* **2017**, *19*, 727–733.

[17] Moreno-García, H.; Messina, S.; Calixto-Rodriguez, M.; Martínez, H. *Appl. Surf. Sci.* **2014**, *311*, 729–733.

[18] Sonawane, P. S.; Patil, L. A. *Mater. Chem. Phys.* **2007**, *105*, 157–161.

[19] Raut, S. S.; Dhobale, J. A.; Sankapal, B. R. *Physica E* **2017**, *87*, 209–212.

[20] Becker, M. A.; Radich, J. G.; Bunker, B. A.; Kamat, P. V. *J. Phys. Chem. Lett.* **2014**, *5*, 1575−1582.

[21] Khadraoui, M.; Benramdane, N.; Miloua, R.; Mathieu, C.; Bouzidi, A.; Sahraoui, K. *Optelectron. Adv. Mater.* **2015**, *9*, 1167–1170.

[22] Bubenhofer, S. B.; Schumacher, C. M.; Koehler, F. M.; Luechinger, N. A.; Grass, R. N.;

Stark, W. J. *J. Phys. Chem. C* **2012**, *116*, 16264−16270.

[23] Maclachlan, A. J.; O'Mahony, F. T. F.; Sudlow, A. L.; Hill, M. S.; Molloy, K. C.; Nelson, J.; Haque, S. A. *ChemPhysChem* **2014**, *15*, 1019–1023.

[24] Han, Q.; Chen, J.; Yang, X.; Lu, D.; Wang, X. *J. Phys. Chem. C* **2007**, *111*, 14072–14077.

[25] Timchenko, V. P.; Novozhilov, A. L.; Slepysheva, O. A. *Russ. J. General. Chem.* **2004**, *74*, 1046–1050.

[26] Wang, S.; Gao, Q.; Wang, J. *J. Phys. Chem. B* **2005**, *109*, 17281–17289.

[27] Li, M.; Li, R. K. *CrystEngComm* **2013**, *15*, 4176–4180.

[28] Saeki, A.; Yoshikawa, S.; Tsuji, M.; Koizumi, Y.; Ide, M.; Vijayakumar, C.; Seki, S. *J. Am. Chem. Soc.* **2012**, *134*, 19035–19042.

[29] Yao, J.; Zheng, Z.; Yang, G. *Adv. Funct. Mater.* **2017**, *27*, 1701823/1–10.

[30] Yao, J.; Yang, G. *Small* **2018**, *14*, 1704524/1–8.

[31] Calzia, V.; Piras, R.; Ardu, A.; Musinu, A.; Saba, M.; Bongiovanni, G.; Mattoni, A. *J. Phys. Chem. C* **2015**, *119*, 16913–16919.

[32] De Wolf, S.; Holovsky, J.; Moon, S. –J.; Löper, P.; Niesen, B.; Ledinsky, M.; Haug, F. J.; Yum, J. –H.; Ballif, C. *J. Phys. Chem. Lett.* **2014**, *5*, 1035−1039.

[33] Yao, J.; Shao, J.; Wang, Y.; Zhao, Z.; Yang, G. *Nanoscale* **2015**, *7*, 12535–12541.

[34] Park, B. –W.; Philippe, B.; Zhang, X.; Rensmo, H.; Boschloo, G.; Johansson, E. M. J. *Adv. Mater.* **2015**, *27*, 6806–6813.

[35] Kim, Y.; Yang, Z.; Jain, A.; Voznyy, O.; Kim, G. –H.; Liu, M.; Quan, L. N.; de Arquer, F. P. G.; Comin, R.; Fan, J. Z.; Sargent, E. H. *Angew. Chem. Int. Ed.* **2016**, *55*, 9586–9590.

[36] Bernechea, M.; Miller, N. C.; Xercavins, G.; So, D.; Stavrinadis, A.; Konstantatos, G. *Nat. Photonics* **2016**, *10*, 521–525.

[37] Choi, Y. C.; Lee, D. U.; Noh, J. H.; Kim, E. K.; Seok, S. I. *Adv. Funct. Mater.* **2014**, *24*, 3587–3592.

[38] Zhou, Y.; Wang, L.; Chen, S.; Qin, S.; Liu, X.; Chen, J.; Xue, D. –J.; Luo, M.; Cao, Y.; Cheng, Y.; Sargent, E. H.; Tang, J. *Nat. Photonics* **2015**, *9*, 409–415.

Chapter 4: Comparative Study of Charge Carrier Dynamics in Bismuth Dimer and Double Perovskite

4-1. Introduction

Bismuth-based halide semiconducting materials such as dimer structure of $A_3Bi_2I_9$ ($A = Cs^+$, $CH_3NH_3^+$ (MA), $(CH_3)_2NH^+$ (FA)) and double perovskite (DP) of $Cs_2AgBiBr_6$ have been widely investigated for photovoltaic application. Park *et al.* performed a theoretical and experimental study on the dimer $A_3Bi_2I_9$ ($A = Cs^+$, MA) solar cells.[1] Pazoki, *et al.* reportedly showed the large carrier effective mass and exciton binding energy of $A_3Bi_2I_9$ by theoretical calculation.[2] Shin, *et al.* demonstrated 0.71% PCE for $Cs_3Bi_2I_9$ by solvent engineering and device structure optimization.[3] On the other hand, 3-dimensional (3D) DPs such as $Cs_2AgBiBr_6$ are claimed to exhibit better charge transport property than $A_3Bi_2I_9$ dimer structures, owing to the band-like transport.[4,5] Indeed, $Cs_2AgBiBr_6$-based solar cells have exhibited the higher PCE of 2.23% than $A_3Bi_2I_9$-based solar cells.[4] However, the PCE is still much lower than the theoretical limit of 7.92% calculated from the spectral integration and assumed small voltage loss.[6] A low photocurrent density is presumably due to the large effective mass of charge carrier and giant electron-phonon coupling.[7] However, direct observation of charge carrier generation, transport, and transfer process including non-radiative recombination are mostly unexplored in these materials.

In this chapter, it is described that the dynamics of photogenerated charge carrier were investigated by using TRMC measurement.[8,9] Photoconductivity and charge carrier transport /transfer from $A_3Bi_2I_9$ or $Cs_2AgBiBr_6$ to electron transport material (ETM) and hole transport material (HTM) were comparatively evaluated, which showed a good correlation with the solar cell performance. The obtained results contribute to understanding the potential optoelectronic performance of bismuth-based halide materials.

4-2. Results and discussion

4-2-1. Charge transport property evaluated by TRMC

Thin films of $A_3Bi_2I_9$ and $Cs_2AgBiBr_6$ were prepared by simple spin-coating and thermal annealing of precursor solution (see Experimental). XRD pattern of each film showed a good agreement with the previous reports,[3,4] indicating that crystal structures of prepared film samples are expected dimer or DP (Figure 4-1a). The resultant crystal structures of $A_3Bi_2I_9$ (A = Cs, MA, FA) and $Cs_2AgBiBr_6$ are shown in Figure 4-1b and c, respectively. The bandgap energies (E_g) were determined from the onset of UV-vis absorption spectra, where absorption edges of Tauc plot (n = 2) correspond to the direct transition (Figure 4-1d).[29] The determined E_g were $Cs_3Bi_2I_9$: 2.05 eV, $MA_3Bi_2I_9$: 2.16 eV, $FA_3Bi_2I_9$: 2.20 eV, and $Cs_2AgBiBr_6$: 2.37 eV. If $Cs_2AgBiBr_6$ is regarded as an indirect transition material as reported previously,[11] its E_g is 2.20 eV from the Tauc plot of n = 1/2. These results are also consistent with the literature,[11] which further supports the appropriate preparation of the films. Emission was too small to be detected in fluorescence spectrometer.

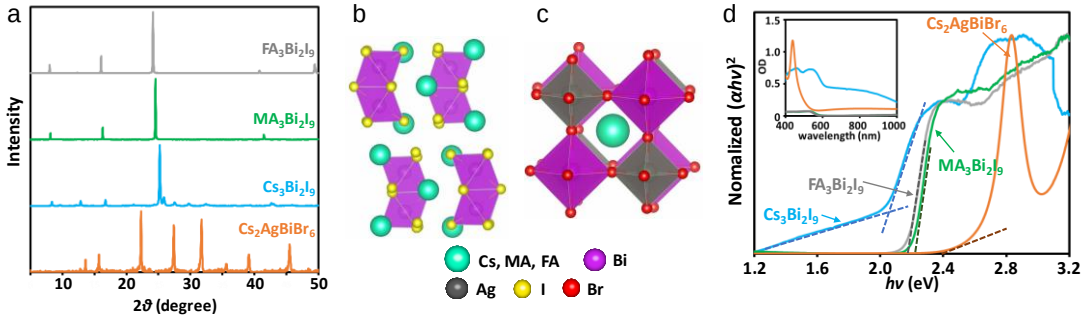

Figure 4-1. (a) XRD patterns of $FA_3Bi_2I_9$, $MA_3Bi_2I_9$, $Cs_3Bi_2I_9$, and $Cs_2AgBiBr_6$ thin films. Schematic image of crystal structure of (b) $A_3Bi_2I_9$ and (c) $Cs_2AgBiBr_6$. (d) Tauc plots of film samples obtained from photoabsorption spectra. The inset is the original absorption spectra.

TRMC measurements of dimer $A_3Bi_2I_9$ were carried out for the single layer films (single), bilayer films (n/i) composed of mp-TiO_2 as n-type ETM and $A_3Bi_2I_9$ as the intrinsic (i) layer, and triple layer films ($n/i/p$) composed of mp-TiO_2, $A_3Bi_2I_9$, and Poly(bis(4-phenyl)(2,4,6-trimethylphenyl)amine) (PTAA) as p-type HTM (Figure 4-2a). The single layer films showed very similar TRMC transients among the samples ($Cs_3Bi_2I_9$, $MA_3Bi_2I_9$, and $FA_3Bi_2I_9$) in both $\phi\Sigma\mu$ maxima ($\phi\Sigma\mu_{max}$) of (1–2) × 10^{-4} cm^2 V^{-1} s^{-1} and decay speed (Figure 4-2b–d). The n/i films showed distinct increase of $\phi\Sigma\mu_{max}$ and

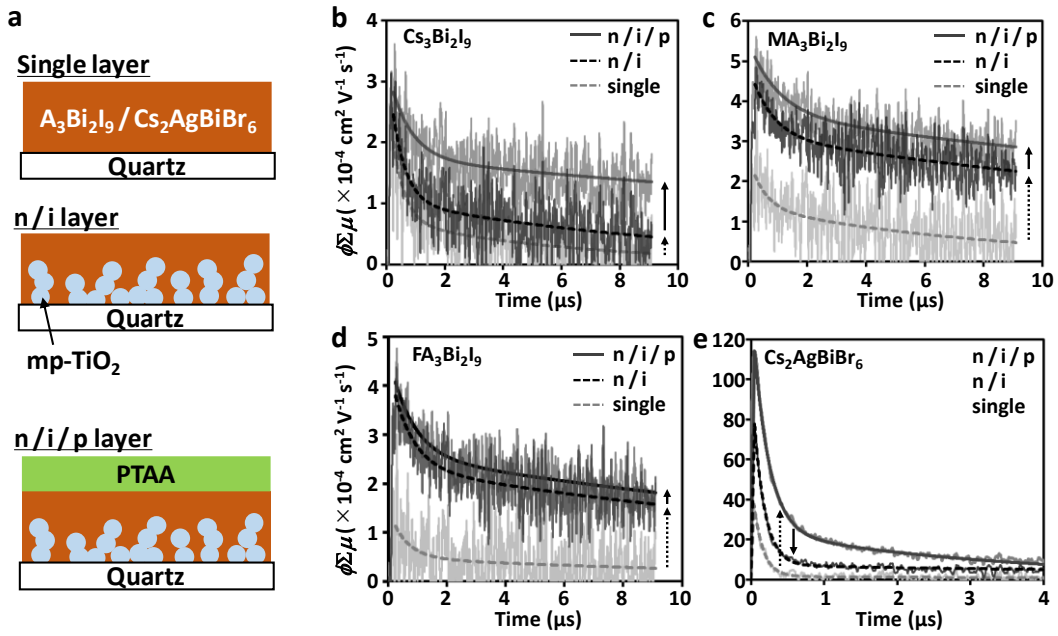

Figure 4-2. (a) Schematics of film sample for TRMC measurement. TRMC transients of (b) $Cs_3Bi_2I_9$, (c) $MA_3Bi_2I_9$, (d) $FA_3Bi_2I_9$, and (e) $Cs_2AgBiBr_6$ thin films. The fitting curves are drawn by double exponential functions: $A_1\exp(-k_1t) + A_2\exp(-k_2t)$. The effective lifetime (τ) was calculated by $(A_1/k_1 + A_2/k_2)/(A_1 + A_2)$. The colors and line shape of fitting curves correspond to the sample structure; single *i* layer (gray dot line), *n*/*i* layer (black dot line), and *n*/*i*/*p* layer (black solid line).

Table 4-1. Summary of $\phi\Sigma\mu_{max}$ and effective lifetime (τ, see Figure 4-2) obtained from double exponential fitting.

Materials	$\phi\Sigma\mu_{max}$ ($\times10^{-4}$ cm^2 V^{-1} s^{-1})			τ (μs)		
	single	*n*/*i*	*n*/*i*/*p*	single	*n*/*i*	*n*/*i*/*p*
$Cs_3Bi_2I_9$	2.0	2.5	2.8	0.61	0.75	1.8
$MA_3Bi_2I_9$	2.0	4.2	5.0	1.2	2.4	3.3
$FA_3Bi_2I_9$	1.2	3.6	4.0	0.97	1.7	2.0
$Cs_2AgBiBr_6$	38	110	78	0.13	0.26	0.16

effective lifetime (τ) compared with the single layers (Table 4-1). This is explained by electron transfer from $A_3Bi_2I_9$ to mp-TiO_2 and retarded charge recombination, where the electron mobility in $A_3Bi_2I_9$ is assumed much smaller than that in TiO_2 (~10^{-1} cm^2 V^{-1} s^{-1}).[12] It should be noted that the increase of $\phi\Sigma\mu_{max}$ was insignificant without HI addition. Although electron transfer to mp-TiO_2 was observed, the increase of $\phi\Sigma\mu_{max}$ from single layer to *n*/*i* layer was insignificant (from (1.2–2.0) × 10^{-4} to (2.5–4.2) × 10^{-4} cm^2 V^{-1} s^{-1}), which is much lower than electron mobility in TiO_2 (~10^{-1} cm^2 V^{-1} s^{-1}).[12] This would suggest the inefficient electron transfer to TiO_2. Similarly, hole transfer was examined by comparing TRMC signals of *n*/*i* layer and *n*/*i*/*p* layer, showing the increase of $\phi\Sigma\mu_{max}$ as small as 0.1–0.2 times. Therefore, hole transfer is also inefficient and/or TRMC hole mobility of $A_3Bi_2I_9$ is comparable to that of PTAA (~10^{-1} cm^2 V^{-1} s^{-1}).[13] Despite the low hole/electron transfer, the charge recombination is suppressed to some extent, which would merit the solar cell performance. In addition, $A_3Bi_2I_9$ suffers from a large exciton binding energy, short carrier diffusion length, and high trap state density,[4] in accordance with the low score of the TRMC evaluation.

Besides, the single layer of $Cs_2AgBiBr_6$ DP showed much higher $\phi\Sigma\mu_{max}$ of 3.8 × 10^{-3} cm^2 V^{-1} s^{-1} than $A_3Bi_2I_9$ dimer (Figure 4-2d). This is possibly associated with the 3D crystal structure of $Cs_2AgBiBr_6$ that leads to a small exciton binding energy and high charge carrier mobility.[4] However, the τ of TRMC transient of $Cs_2AgBiBr_6$ (0.13 μs) is much shorter than those of $A_3Bi_2I_9$ (~1 μs). After compositing with mp-TiO_2, the $\phi\Sigma\mu_{max}$ of $Cs_2AgBiBr_6$ exhibited a notable increase in the $\phi\Sigma\mu_{max}$ (from 3.8 × 10^{-3} to 1.1 × 10^{-2} cm^2 V^{-1} s^{-1}), and the τ was extended by two times, owing to more efficient electron transfer than $A_3Bi_2I_9$. In contrast, the $\phi\Sigma\mu_{max}$ of *n*/*i*/*p* layer was decreased compared with that of *n*/*i* layer, which opposes to $A_3Bi_2I_9$. This suggests that $Cs_2AgBiBr_6$ has a higher hole mobility than PTAA. Note that low ϕ (<<1) of $Cs_2AgBiBr_6$ limits $\phi\Sigma\mu_{max}$. This is the origin of lower $\phi\Sigma\mu_{max}$ of *n*/*i*/*p* $Cs_2AgBiBr_6$ (~8 × 10^{-3} cm^2 V^{-1} s^{-1}) than the hole mobility of PTAA (~10^{-1} cm^2 V^{-1} s^{-1}).

Regardless of the layer structure (single, *n*/*i*, and *n*/*i*/*p*), $MA_3Bi_2I_9$ showed greater $\phi\Sigma\mu_{max}$ and τ than $Cs_3Bi_2I_9$ and $FA_3Bi_2I_9$, suggestive of superior solar cell performance of $MA_3Bi_2I_9$ to $Cs_3Bi_2I_9$ and $FA_3Bi_2I_9$. Remarkably, $Cs_2AgBiBr_6$ displayed more increased $\phi\Sigma\mu_{max}$ than $MA_3Bi_2I_9$, and thus it should show the highest PCE in these pseudo-perovskites. Note that $\phi\Sigma\mu_{max}$ of high-performing $MAPbI_3$ is extremely large (~70 cm^2 V^{-1} s^{-1}) and shows nearly 100% electron and hole transfer efficiencies from $MAPbI_3$ to mp-TiO_2 and PTAA.[14] Based on these facts, $Cs_2AgBiBr_6$ is still unable to compete with $MAPbI_3$.

4-2-2. Solar cell performance

Consequently, photovoltaic devices with a normal structure (FTO/compact TiO_2/mp-TiO_2 /absorber/PTAA (doped)/Au) were prepared (Figure 4-3a). According to the energy diagram obtained from PYS and Tauc plot, all absorbers have downhill energy levels of VBM and conduction band minimum (CBM) relative to HTL and ETL, respectively (Figure 4-3b). In spite of the energy level matching, $A_3Bi_2I_9$-based devices showed a poor short circuit current density (J_{SC}, ~0.11 mA cm^{-2}), which strictly limited the PCE (< 0.016%) (Table 4-2). The external quantum efficiency (EQE) spectra also

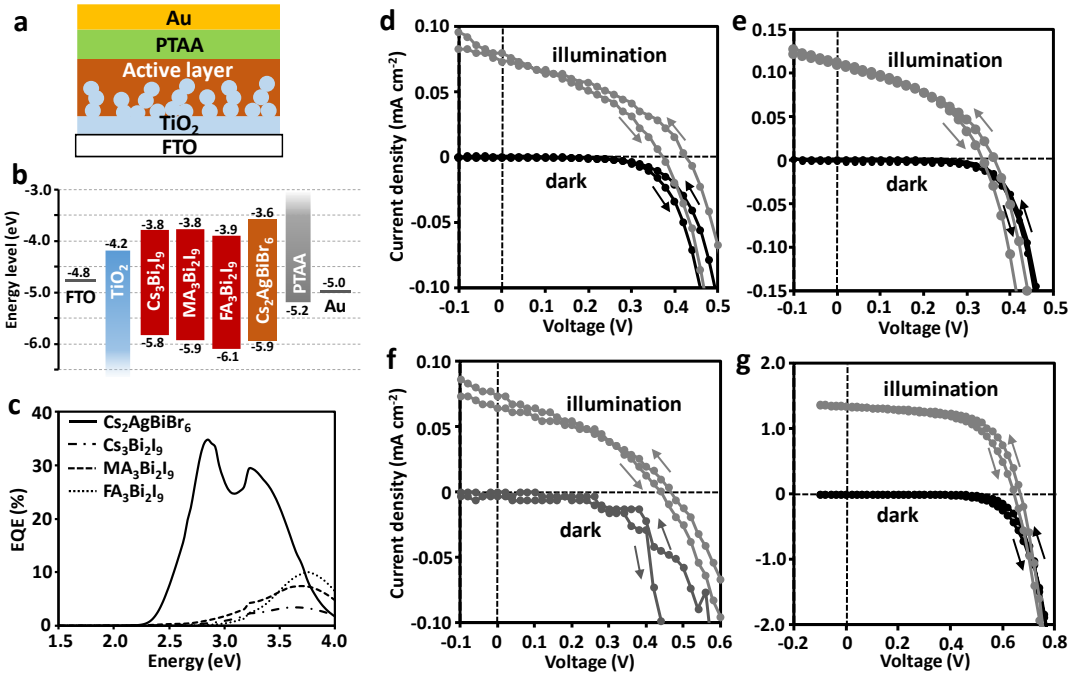

Figure 4-3. (a) Schematic of a layered photovoltaic device. (b) Energy diagram of each layer obtained from PYS and UV-vis measurement. (c) EQE spectra of each devices. *J-V* curve of photovoltaic devices based on $A_3Bi_2I_9$ (A = (d) Cs, (e) MA, and (f) FA) and (g) $Cs_2AgBiBr_6$.

Table 4-2. Summary of best-performed device performance.

	J_{SC} (mA cm^{-2})	V_{OC} (V)	FF	R_S (Ω cm^2)	R_{Sh} (kΩ cm^2)	PCE (%)
$Cs_3Bi_2I_9$	0.076	0.40	0.38	100	11	0.012
$MA_3Bi_2I_9$	0.11	0.34	0.42	20	7.4	0.016
$FA_3Bi_2I_9$	0.068	0.45	0.39	1000	14	0.012
$Cs_2AgBiBr_6$	1.2	0.92	0.64	40	7.3	0.72

show very low values for $A_3Bi_2I_9$ (Figure 4-3c). Their PCE and J_{SC} were even lower without HI processing. These results are consistent with the TRMC evaluations, which showed the small $\phi\Sigma\mu_{max}$ and low charge transfer efficiency to ETL and HTL. Despite insignificant leak current (Figure 4-3d−f), a large open circuit voltage loss (~1.89 eV) and low fill factor (~0.42) are observed. This might result from a high trap density[15] and large offset between VBM of $A_3Bi_2I_9$ and HOMO of PTAA.

Meanwhile, $Cs_2AgBiBr_6$-based device afforded more than 10-fold higher J_{SC} (1.2 mA cm^{-2}) compared with the $A_3Bi_2I_9$-based devices. This is also consistent with the high $\phi\Sigma\mu_{max}$ and charge transfer efficiency observed in TRMC evaluation. In addition, $Cs_2AgBiBr_6$-based device showed smaller V_{OC} loss (~1.46 eV) and higher FF value (~0.64), which suggests a less trap state density than $A_3Bi_2I_9$. However, the obtained PCE is still considerably lower than theoretical limit (7.92%),[5] suffering from the limited current density. The significantly small J_{SC} compared to the integration of solar spectrum up to the bandgap (~8 mA cm^{-2}) is probably caused by the low ϕ value due to inefficient charge separation and the limited charge carrier transfer as revealed in TRMC evaluation. To quantify the ϕ value for further discussion, transient photocurrent (TPC) measurement and charge extraction (CE) measurement appears to promising way, where generated charge density (n) and bimolecular recombination current density (J_{bi}) is obtained.[17–19] The hysteresis in *J-V* curve (forward: 0.69%, reverse: 0.76%) is not so small, which is frequently considered as a result of ion migration in perovskite solar cells.[16] Anti-solvent treatment which is not used in the study described in this chapter is expected to decrease vacancies responsible for the hysteresis.

4-3. Conclusion

The charge carrier dynamics in $A_3Bi_2I_9$ dimer ($A = Cs^+$, $CH_3NH_3^+$, and $HC(NH_2)_2^+$) and $Cs_2AgBiBr_6$ DP were studied by TRMC evaluation. $Cs_2AgBiBr_6$ single layer film showed a relatively high TRMC signal compared with $A_3Bi_2I_9$ owing to the higher electron and hole mobility. In addition, $Cs_2AgBiBr_6$/mp-TiO_2 bilayer showed the greater increase of $\phi\Sigma\mu_{max}$ (1.1×10^{-2} cm^2 V^{-1} s^{-1}) than $A_3Bi_2I_9$/mp-TiO_2 bilayer. This indicates a higher electron transfer efficiency in the former. However, the electron and hole transfer efficiencies were not high enough compared to the high-performing $MAPbI_3$. The obtained device performance, especially current density, showed a good agreement with TRMC evaluation. Despite the limited potential of $A_3Bi_2I_9$ and $Cs_2AgBiBr_6$ as the light absorber, this result provides a rational step for exploring forthcoming lead-free perovskites. Based on the insight, further material exploration is desired.

4-4. Experimental

Materials and film preparation

CsI, MAI, FAI were purchased from Tokyo Chemical Industry (TCI) Co., Ltd. CsBr, BiI_3, $BiBr_3$ were bought from Sigma-Aldrich Co., Ltd. All chemicals were used without further purification. A 0.5 M precursor solution of $A_3Bi_2I_9$ and $Cs_2AgBiBr_6$ (molar fraction) was prepared in a N_2-filled glovebox by dissolving 0.5 mmol of BiI_3 or $BiBr_3$ and stoichiometric amount of AX (A = Cs, MAI, FAI, X = I, Br) into 1 mL dimethyl sulfoxide (DMSO). 40 μL HI aqueous solution (54 wt%, TCI) was added to $A_3Bi_2I_9$ solution to increase solubility and improve film quality. The precursor solution was spin-coated onto a substrate with/without mesoporous (mp) TiO_2 at 2,000 rpm for 30 s. The obtained films were subsequently annealed at 110 °C for $A_3Bi_2I_9$ and 250 °C for $Cs_2AgBiBr_6$ for 10 min. For the observation of hole transfer, a toluene solution (10 mg/mL) of poly(triarylamine) (PTAA) with Li-dopant (Li-TFSI) was spin-coated onto the $A_3Bi_2I_9$ or $Cs_2AgBiBr_6$ film. These procedures were operated inside the glovebox.

Film characterization

Valence band maxima (VBM) was measured by photoelectron yield spectroscopy (PYS) using a Bunko Keiki Corp. BIP-KV201 (accuracy: ±0.02 eV, extraction voltage = 10 V) in a vacuum ($<10^{-2}$ Pa). The film was prepared onto a F-doped SnO_2 (FTO) layer on a glass substrate, which was contacted through aluminum tape and an Au-coated electrode. X-ray diffraction (XRD) was performed by using a Rigaku Corp. MiniFlex-600 instrument (Cu Kα radiation: λ = 1.54 Å) in the air at room temperature. Photoabsorption spectra were measured using a Jasco Corp. V-730.

TRMC

A thin film was prepared on a quartz plate. The sample was set in a resonant cavity and probed by continuous microwaves at ca. 9.1 GHz. The excitation laser (500 nm) from an optical parametric oscillator (OPO, Continuum Inc., Panther) seeded by the third harmonic generation of a Nd:YAG laser (Continuum Inc., Surelite II, 5−8 ns pulse duration, 10 Hz) was used as the excitation. The photon density (I_0) was changed from 6.4×10^{14} to 2.6×10^{15} photons cm^{-2} $pulse^{-1}$. The photoconductivity transient $\Delta\sigma$ was converted to $\phi\Sigma\mu$ via the eq. 1-5 in Chapter 1.

Device fabrication

An FTO substrate was cleaned with detergent, acetone, isopropyl alcohol, and deionized water, a compact TiO_2 layer was deposited onto the FTO/glass by spray pyrolysis using a solution of titanium diisopropoxide bis(acetylacetonate) (Sigma Aldrich) in ethanol (1:40 v/v) at 500 °C. The substrate was immersed in a 50 mM aqueous solution of $TiCl_4$ (Wako Chemical Industries Ltd.) for 30 min, followed by rinsing with deionized water and sintering at 500 °C for 20 min. A 200 nm-thick mp-TiO_2 layer was deposited onto the compact TiO_2 layer by spin-coating (5,000 rpm, 30 s) of a diluted TiO_2 paste (PST−18NR, JGC Catalysts and Chemicals Ltd.) in ethanol (paste/ethanol = 1:7 w/w), followed by sintering at 500 °C for 20 min. A precursor solution was spin-coated at 2,000 rpm for 30 s onto a substrate, followed by annealing at 100 °C for 10 min. A PTAA toluene solution with Li-TFSI (PTAA : Li-TFSI = 1 : 0.15) was spin-coated (4,000 rpm, 30s) as HTL. Subsequently, a 100 nm-thick gold anode was thermally deposited in a vacuum chamber. R_s and R_{sh} values were calculated from the inverse of the slope of *JV* curve at $V = V_{OC}$ and $V = 0$, respectively.

4-5. Reference

[1] Park, B. W.; Philippe, B.; Zhang, X.; Rensmo, H.; Boschloo, G.; Johansson, E. M. J. *Adv. Mater.* **2015**, *27*, 6806–6813.

[2] Pazoki, M.; Johansson, M. B.; Zhu, H.; Broqvist, P.; Edvinsson, T.; Boschloo, G.; Johansson, E. M. J. *J. Phys. Chem. C* **2016**, *120*, 29039–29046.

[3] Shin, S. S.; Correa Baena, J. P.; Kurchin, R. C.; Polizzotti, A.; Yoo, J. J.; Wieghold, S.; Bawendi, M. G.; Buonassisi, T. *Chem. Mater.* **2018**, *30*, 336–343.

[4] Gao, W.; Ran, C.; Xi, J.; Jiao, B.; Zhang, W.; Wu, M.; Hou, X.; Wu, Z. *ChemPhysChem* **2018**, *19*, 1696–1700.

[5] Hutter, E. M.; Gélvez-Rueda, M. C.; Bartesaghi, D.; Grozema, F. C.; Savenije, T. J. *ACS Omega*, **2018**, *3*, 11655−11662.

[6] Savory, C. N.; Walsh, A.; Scanlon, D. O. *ACS Energy Lett.* **2016**, *1*, 949–955.

[7] Steele, J. A.; Puech, P.; Keshavarz, M.; Yang, R.; Banerjee, S.; Debroye, E.; Kim, C. W.; Yuan, H.; Heo, N. H.; Vanacken, J.; Walsh, A.; Hofkens, J.; Roeffaers, M. B. J. *ACS Nano* **2018**, *12*, 8081–8090.

[8] Saeki, A.; Yoshikawa, S.; Tsuji, M.; Koizumi, Y.; Ide, M.; Vijayakumar, C.; Seki, S. A *J. Am. Chem. Soc.* **2012**, *134*, 19035–19042.

[9] Nishikubo, R.; Saeki, *J. Phys. Chem. Lett.* **2018**, *9*, 5392–5399.

[10] Li, T.; Wang, Q.; Nichol, G. S.; Morrison, C. A.; Han, H.; Hu, Y.; Robertson, N. *Dalt. Trans.* **2018**, *47*, 7050–7058.

[11] Pantaler, M.; Cho, K. T.; Queloz, V. I. E.; García Benito, I.; Fettkenhauer, C.; Anusca, I.; Nazeeruddin, M. K.; Lupascu, D. C.; Grancini, G. *ACS Energy Lett.* **2018**, *3*, 1781–1786.

[12] A. Saeki, Y. Yasutani, H. Oga, S. Seki, *J. Phys. Chem. C* **2014**, 118, 22561–22572.

[13] T. Fukumatsu, A. Saeki, S. Seki, *Appl. Phys. Express* **2012**, *5*, 061701/1–3.

[14] Ishida, N.; Wakamiya, A.; Saeki, A. *ACS Photonics* **2016**, *3*, 1678–1688.

[15] Jiang, F.; Yang, D.; Jiang, Y.; Liu, T.; Zhao, X.; Ming, Y.; Luo, B.; Qin, F.; Fan, J.; Han, H.; Zhang, L.; Zhou, Y. *J. Am. Chem. Soc.* **2018**, *140*, 1019–1027.

[16] Yuan, Y.; Huang, J. *Acc. Chem. Res.* **2016**, *49*, 286–293.

[17] Shuttle, C. G.; Hamilton, R.; O'Regan, B. C.; Nelson, J.; Durrant, J. R. *PNAS* **2010**, *107*, 16448–16452.

[18] Maurano, A.; Shuttle, C. G.; Hamilton, R.; Ballantyne, A. M.; Nelson J.; Zhang, W.; Heeney, M.; Durrant, J. R. *J. Phys. Chem. C* **2011**, *115*, 5947–5957.

[19] Credgington, D.; Durrant, J. R. *J. Phys. Chem. Lett.* **2012**, *3*, 1465–1478.

Chapter 5: Optoelectronic and Energy Level Exploration of Bi- and Sb-Based Photoabsorber

5-1. Introduction

There are numerous crystal structures of Bi- and Sb-based materials as described in Chapter 1. The most primitive one is $A_3M_2X_9$,[1–7] with dimer or layered crystal structures (Figure 1-7a in Chapter 1), though the dimer such as $A_3Bi_2I_9$ (A = Cs, MA, FA) would be detrimental to the exciton diffusion and efficient charge transport,[8] resulting in a low PCE (Chapter 4).[9] Besides, other halide materials such as silver bismuth iodide (e.g., $AgBiI_4$)[10–12] and the $A_2MM'X_6$ DPs[13–16] (Figure 1-7b, c), chalcogenide materials[24–27] (Figure 1-7d), and chalcohalide materials such as rod-like MSX[17–20] and $AMSX_2$ split-anion perovskites (SAPs) (Figure 1-7e, f)[21–23] are also notable. However, a comprehensive evaluation and comparison of these candidates are still lacking in terms of their intrinsic optoelectronic nature and predominant process of carrier dynamics, which precludes a rational design of various compositions, crystal structures, and device physics.

In the work presented in Chapter 5, the author performed a rigorous exploration of Bi- and Sb-based materials through the use of contact-less, time-resolved microwave conductivity (TRMC) measurements along with electrochemical characterizations.[28] TRMC measurements yield the transient photoconductivity ($\Delta\sigma$), which provides an important factor associated with the intrinsic optoelectronics (eq. 1-5 in Chapter 1).[29] In addition, the TRMC measurements of multi-layered samples revealed the charge transfer from the active layer to the electron transport material (ETM) and hole transport material (HTM).[30] The author prepared a total of 44 different compositions, including 12 compositions of $A_3M_2X_9$ (A = Cs, MA, FA, M = Bi, Sb, X = I, Br), 4 compositions of MSX (M = Bi, Sb, X = I, Br), 2 compositions each of M_2S_3 and $AgMI_4$ (M = Bi, Sb), 12 compositions of $A_2MM'X_6$ DP (A = Cs, MA, FA, M = Bi, Sb, M' = Ag, X = I, Br), and 12 compositions of $AMSX_2$ SAP (A = Cs, MA, FA, M = Bi, Sb, X = I, Br) and characterized them by X-ray diffraction (XRD), UV-vis photoabsorption spectroscopy, and photoelectron yield spectroscopy (PYS). Based on the TRMC and solar cell characterizations, the combination of the active layer and chemical structure of the HTMs were found to significantly influence the charge extraction, rather than the energy-level matching of the conduction band minimum (CBM) and valence band maximum (VBM).

5-2. Results and Discussion

5-2-1. Structural characterization

Performing the initial characterization, XRD measurements were conducted on the 44 film samples (Figure 5-1) prepared by solution process (see Experimental). The XRD patterns of $A_3M_2X_9$ were revealed to be consistent with the previous reports[4,5,7] or reconstructed XRD patterns of Crystallographic Open Database (COD) data, confirming the formation of the expected multi-crystalline films (Figure 5-1a, b, i, j, Table 5-1). They showed high crystallinities, as evident from the XRD peaks, which were much more intense than those of the other samples. It is assumed that the isolated $[M_2X_9]^{3-}$ units with reduced crystal strain facilitate the growth of large crystal grains.

For the rod-like MSX structure, expected crystalline XRD profiles were obtained in BiSI, BiSBr, and SbSI films, whereas the SbSBr film exhibited no peaks (Figure 5-1c, k). Thus, this film was renamed as "Sb-S-Br". Of note, the annealing of SbSI at 240 ℃ revealed the appearance of Sb_2S_3 contamination (Figure 5-1k). Energy dispersive X-ray fluorescence (EDX) measurements of the SbSI at 240 ℃ and Sb-S-Br films clearly showed the presence of expected elements (SbSI at 240 ℃, Sb : S : I = 1.0 : 0.89 : 0.89; Sb-S-Br, Sb : S : Br = 1.0 : 0.42 : 1.5, Table 5-2).

The chalcogenide films (M_2S_3) were prepared by chemically assisted spin-coat and crystallization (CASC) process (Figure 5-1d, l), which yields a Bi_2S_3 thin film with high electronic and morphological qualities as shown in chapter 3,[31] exhibiting appropriate multi-crystalline films in both Bi_2S_3 and Sb_2S_3. Regarding silver bismuth/antimony iodide, $AgBiI_4$ showed the expected XRD patterns analogous to the $CdCl_2$ structure,[11] whereas $AgSbI_4$ did not. In the case of DPs ($A_2MM'X_6$), a significant contamination of $A_3M_2X_9$ was observed in all their XRD peaks, except for $Cs_2AgBiBr_6$ (Figure 5-1e, f, m, n). Despite the correct inclusion of each component in obtained film (Table 5-2) and their moderate Goldschmidt tolerance factors (0.88–1.09, Table 5-3),[32,33] the formation of $A_3M_2X_9$ was dominant as the dimer and layered structures were thermodynamically more stable than that of the DPs.

For the SAPs ($AMSX_2$), remnant contamination-originated XRD peaks arisen from $A_3M_2X_9$ were also observed, except $CsSbSI_2$ and $MASbSI_2$ (Figure 5-1g, h, o, p). The XRD profiles of $MASbSI_2$ were identical to those reported by Nie *et al.*[22] Although the XRD references for the other SAP materials could not be found, the pattern of $CsSbSI_2$ is analogous to that of $MASbSI_2$; thus, the $CsSbSI_2$ is assumed to be appropriately formed. Meanwhile, the other compositions failed to form SAP structure, resulting in the dominant formation of $A_3M_2X_9$. Importantly, the author developed a simple one-step spin-coating

method using metal ethylxanthate[34] as the metal and sulfur source for the preparation of MSX and SAP thin films. This is completely different from the previously reported step-by-step chemical bath deposition (CBD) and spin-coating methods.[22] Accordingly, the author summarized the results of the XRD measurements and categorized them into four types: (A) well-identified without contamination, (B) includes a little contamination, (C) includes dominant contamination, and (U) crystal structures are unable to be resolved (Table 5-1). Hereafter, because large part of DP and SAP precursor yielded $A_3M_2X_9$ structures, those samples are identified as "$A_3M_2X_9$ from A_2AgMX_6/$AMSX_2$ precursor".

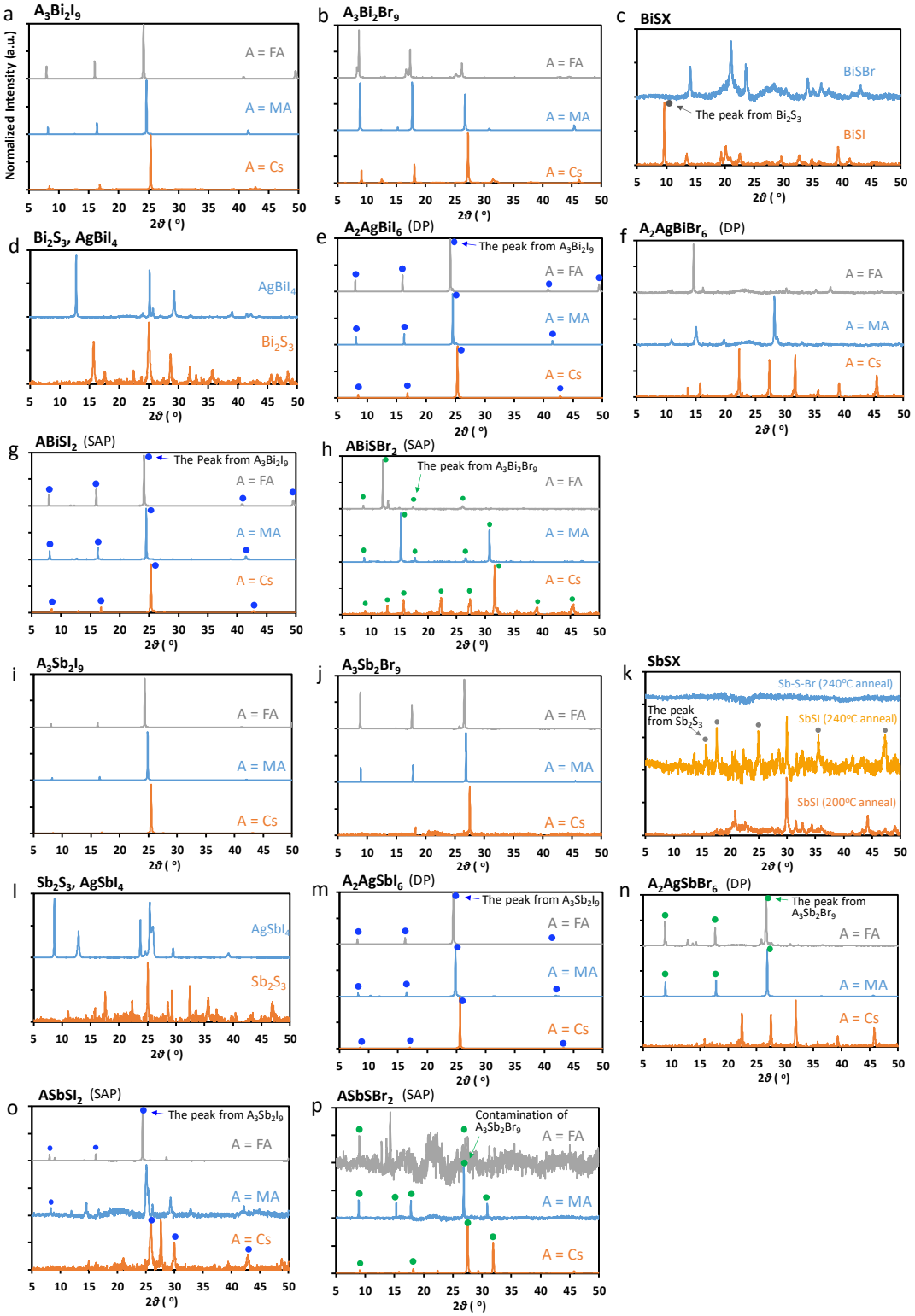

Figure 5-1. XRD patterns of all the samples. Contamination of other crystal phases such as $A_3M_2X_9$ is given by the dots.

Table 5-1. Categorized class of crystal structures evaluated from XRD measurements. (A) without contamination, (B) including a little contamination, (C) including dominant contamination, and (U) crystal structures are unable to be resolved due to the lack of reference or amorphous nature.

Crystal structure	Precursor	Class	Reference [a]	Precursor	Class	Reference [a]
$A_3M_2X_9$	$Cs_3Bi_2I_9$	A	COD: 8103859	$Cs_3Sb_2I_9$	A	COD: 1537132
	$MA_3Bi_2I_9$	A	COD: 4344961	$MA_3Sb_2I_9$	A	COD: 7237225
	$FA_3Bi_2I_9$	A	COD: 7237621	$FA_3Sb_2I_9$	A	Ref. 4
	$Cs_3Bi_2Br_9$	A	COD: 1531067	$Cs_3Sb_2Br_9$	A	COD: 1537138
	$MA_3Bi_2Br_9$	A	Ref. 5	$MA_3Sb_2Br_9$	A	Ref. 7
	$FA_3Bi_2Br_9$	A	COD: 7701111	$FA_3Sb_2Br_9$	A	-
MSX	BiSI	B	COD: 1535800	SbSI	A	COD: 1535787
	BiSBr	A	COD: 1535795	SbSBr	U	COD: 1521208
Layered	Bi_2S_3	A	COD: 9003473	Sb_2S_3	A	COD: 1011154
	$AgBiI_4$	A	Ref. 11	$AgSbI_4$	U	-
DP	Cs_2AgBiI_6	C	-	Cs_2AgSbI_6	C	-
	MA_2AgBiI_6	C	-	MA_2AgSbI_6	C	-
	FA_2AgBiI_6	C	-	FA_2AgSbI_6	C	-
	$Cs_2AgBiBr_6$	A	COD: 4131244	$Cs_2AgSbBr_6$	B	Ref. 16
	$MA_2AgBiBr_6$	A	Ref. 15	$MA_2AgSbBr_6$	C	
	$FA_2AgBiBr_6$	U	-	$FA_2AgSbBr_6$	C	-
SAP	$CsBiSI_2$	C	-	$CsSbSI_2$	U	-
	$MABiSI_2$	C	-	$MASbSI_2$	B	Ref. 22
	$FABiSI_2$	C	-	$FASbSI_2$	C	-
	$CsBiSBr_2$	C	-	$CsSbSBr_2$	C	-
	$MABiSBr_2$	C	-	$MASbSBr_2$	C	-
	$FABiSBr_2$	C	-	$FASbSBr_2$	C	-

[a] Crystallography Open Database (COD) number or the reference number in the main text.

Table 5-2. Summary of elemental analysis by EDX on the compositions which showed dominant formation of other crystal phase such as $A_3M_2X_9$. Note that MA and FA which is composed of C, N, and H cannot be detected.

Precursor	Elemental ratio	Precursor	Elemental ratio
SbSI (240 ℃)	Sb : S : I = 1.0 : 0.89 : 0.89	$CsBiSI_2$	Cs : Bi : S : I = 0.92 : 1.0 : 0.72 : 2.4
SbSBr (240 ℃)	Sb : S : Br = 1.0 : 0.42 : 1.5	$MABiSI_2$	Bi : S : I = 1.0 : 0.46 : 2.2
Cs_2AgBiI_6	Cs : Ag : Bi : I = 1.6 : 0.97 : 1.0 : 4.8	$FABiSI_2$	Bi : S : I = 1.0 : 0.35 : 2.2
MA_2AgBiI_6	Ag : Bi : I = 0.90 : 1.0 : 5.1	$CsBiSBr_2$	Cs : Bi : S : Br = 0.84 : 1.0 : 0.77 : 2.8
FA_2AgBiI_6	Ag : Bi : I = 0.93 : 1.0 : 5.1	$MABiSBr_2$	Bi : S : Br = 1.0 : 0.52 : 2.6
Cs_2AgSbI_6	Cs : Ag : Sb : I = 2.0 : 0.98 : 1.0 : 5.0	$FABiSBr_2$	Bi : S : Br = 1.0 : 0.54 : 2.5
MA_2AgSbI_6	Ag : Bi : I = 0.94 : 1.0 : 5.3	$MASbSI_2$	Sb : S : I = 1.0 : 1.0 : 1.6
FA_2AgSbI_6	Ag : Bi : I = 0.98 : 1.0 : 5.4	$FASbSI_2$	Sb : S : I = 1.0 : 0.62 : 1.5
$MA_2AgSbBr_6$	Ag : Bi : Br = 0.83 : 1.0 : 6.3	$FASbSBr_2$	Sb : S : Br = 1.0 : 0.77 : 2.7
$FA_2AgSbBr_6$	Ag : Bi : Br = 0.74 : 1.0 : 7.1		

Table 5-3. Summary of calculated Goldschmidt tolerance factors (*T*) of DPs and SAPs. The equation is followed; $T = (r_A + r_X)/(2^{1/2}(r_B + r_X))$ where r_A, r_B, and r_X are the effective ionic radii of A site, B site, and X site ion, respectively.[32,33]

Structure	Bi-based	*T*	Sb-based	*T*
DP	Cs_2AgBiI_6	0.876	Cs_2AgSbI_6	0.914
	MA_2AgBiI_6	0.939	MA_2AgSbI_6	0.979
	FA_2AgBiI_6	1.02	FA_2AgSbI_6	1.06
	$Cs_2AgBiBr_6$	0.890	$Cs_2AgSbBr_6$	0.931
	$MA_2AgBiBr_6$	0.958	$MA_2AgSbBr_6$	1.00
	$FA_2AgBiBr_6$	1.04	$FA_2AgSbBr_6$	1.09
SAP	$CsBiSI_2$	0.928	$CsSbSI_2$	1.02
	$MABiSI_2$	0.994	$MASbSI_2$	1.08
	$FABiSI_2$	1.08	$FASbSI_2$	1.18
	$CsBiSBr_2$	0.920	$CsSbSBr_2$	1.01
	$MABiSBr_2$	0.990	$MASbSBr_2$	1.09
	$FABiSBr_2$	1.08	$FASbSBr_2$	1.18

5-2-2. Energy level characterization

The energy levels of the VBM and CBM were measured using optical spectroscopy and PYS, as shown in Figure 5-2 (the original profiles are provided in Experimental). CBM levels were determined by adding the optical bandgaps (direct or indirect transition analysis based on the Tauc plots) to the VBM levels. The bandgap energies of the $A_3M_2X_9$ materials were expectedly wide (2.1–2.8 eV), owing to their poor orbital overlaps of the $[M_2X_9]^{3-}$ units. Notably, Sb-based $A_3M_2X_9$ materials have relatively shallower VBM (−5.5 to −6.1 eV) than Bi-based ones (−5.8 to −6.3 eV). This trend was also observed in other structures, suggesting that Sb-based materials fit the energy levels of common ETM/HTM more suitably than Bi-based ones do. SbSI, Sb-S-Br, Bi_2S_3, and Sb_2S_3 exhibited moderate VBM levels (−5.5 to −5.6 eV) and bandgaps (1.4–1.8 eV). Although $AgBiI_4$ has a relatively narrow bandgap (1.8 eV), its deep VBM level is not ideal for energy-level matching with ETM/HTM. For the perovskite materials, DPs exhibited the wider bandgaps (2.2–2.9 eV) than SAPs (1.8–2.4 eV), as seen in the pictures of the films (Figure 5-3). Some SAPs, such as $CsSbSI_2$ and $MASbSI_2$, demonstrate moderate VBM (−5.6 eV) and CBM levels (−3.7 eV), suitable for charge transfer to ETM/HTM and efficient light absorption.

From the standpoint of VBM level (> −5.7 eV) and bandgap (< 2.0 eV), the author expected Sb-based MSX materials (SbSI and Sb-S-Br), Bi- and Sb-based layered materials (Bi_2S_3 and Sb_2S_3), and Sb-based SAPs ($CsSbSI_2$ and $MASbSI_2$) to be plausible candidates for use in efficient solar cells.

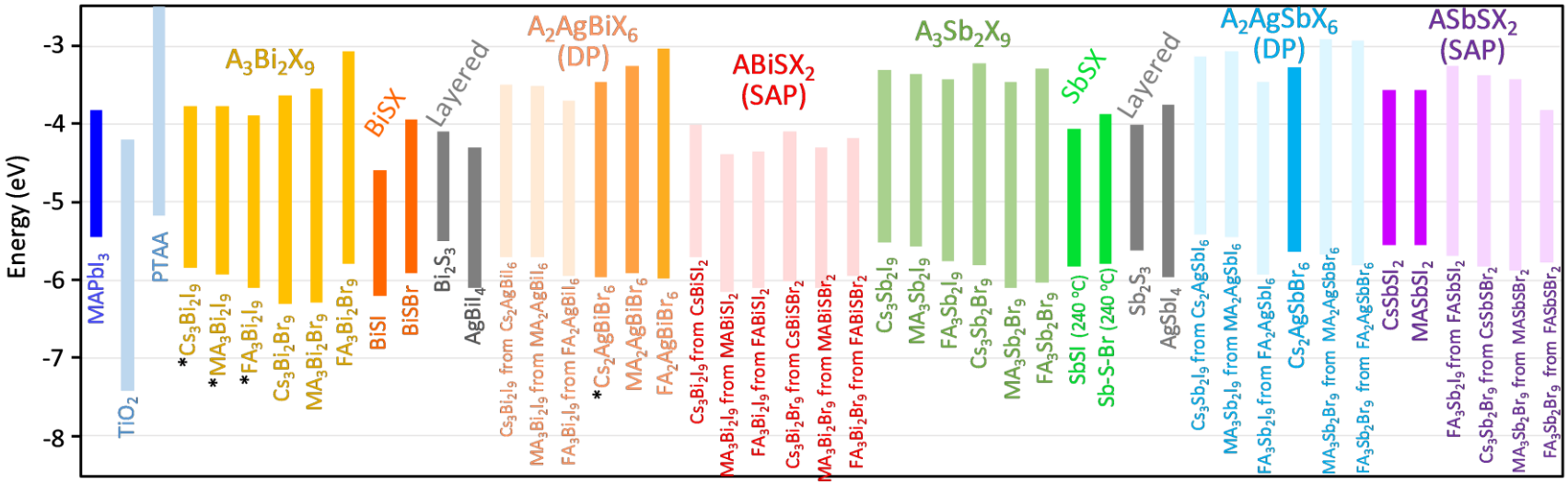

Figure 5-2. Energy levels of VBM and CBM for direct transition of the 44 Bi- and Sb-based films and $MAPbI_3$ obtained from PYS and UV-vis. TiO_2 and poly(tri-arylamine): PTAA are shown as the typical ETM and HTM. The compositions categorized as (C) (formation of different phase is dominant) in Table 5-1 are described with pale colored bar. The asterisk (*) represents the data from Chapter 4.[9]

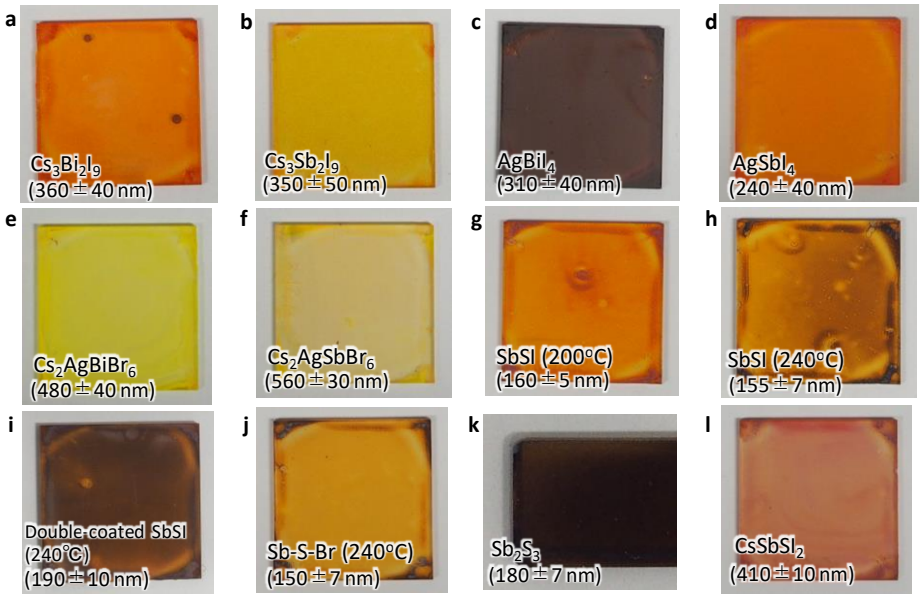

Figure 5-3. Pictures of $Cs_3Bi_2I_9$, $Cs_3Sb_2I_9$, $AgBiI_4$, $AgSbI_4$, $Cs_2AgBiBr_6$, $Cs_2AgSbBr_6$, SbSI (200 ℃), SbSI (240 ℃), double-coated SbSI (240 ℃), Sb-S-Br (240 ℃ annealed), Sb_2S_3, and $CsSbSI_2$ films. The film thickness of active layer/mp-TiO_2 with a standard deviation is appended in brackets. The thickness of mp-TiO_2 is 145 ± 7 nm.

5-2-3. Photoconductivity and electron transport evaluation by TRMC

To evaluate the photoconductive properties of the Bi- and Sb-based materials, the author performed Xe-flash TRMC measurements using a pseudo-sunlight white light pulse as the excitation[28]. Figure 5-4 shows the maximum transient photoconductivity ($\Delta\sigma_{max}$) of the active layer (single *i* layer drawn by narrow black bars) and mesoporous TiO_2 (mp-TiO_2)/active layer (*n*/*i* double layer drawn by wide colored bars) (original TRMC decay are provided in Experimental). The $\Delta\sigma_{max}$ value corresponds to the time-resolved peak of transient photoconductivity and provides a figure-of- merit that includes the generated charge carrier density, local charge carrier mobilities, charge carrier lifetimes at the end of the pulse (~10 μs), and the photoabsorption of the active layer. The single layers of Bi- and Sb-based materials, except for Bi_2S_3, showed a $\Delta\sigma_{max}$ 2–3 orders of magnitude lower than that of $MAPbI_3$ (Figure 5-4, narrow black bars), implying that the charge carrier mobilities of these materials are much smaller than that of $MAPbI_3$ (1–

100 $cm^2\ V^{-1}\ s^{-1}$).[30,35] Although Bi_2S_3 demonstrated high performance as a photodetector comparable to $MAPbI_3$,[31] the *n*-doping in the darkness[36] lead decrease in R_{sh} and inhibit an escalation in the PCE of the Bi_2S_3-based solar cell (< 1%). Meanwhile, some materials, such as SbSI, Sb_2S_3, and $MASbSI_2$, exhibit low $\Delta\sigma_{max}$, whereas their reported J_{SC} values of solar cells under AM1.5G are relatively high, SbSI: 9.11 mA cm^{-2} (FTO/compact-TiO_2/mp-TiO_2/SbSI/HTM/Au), Sb_2S_3: 16.1 mA cm^{-2} (FTO/compact-TiO_2/mp-TiO_2/Sb_2S_3/Au), and $MASbSI_2$: 8.12 mA cm^{-2} (FTO/compact-TiO_2/mp-TiO_2/$MASbSI_2$/HTM/Au).[19,22,27] This inconsistency is resolved by focusing on the results of *n*/*i* double layers, in which SbSX, Sb_2S_3, $AgSbI_4$, and Sb-SAPs showed a 10-fold increase in $\Delta\sigma_{max}$ compared with those of the single layers (Figure 5-4, wide colored bars). This is attributed to the efficient electron transfer (ET) from the active layer to mp-TiO_2, as observed in the mp-TiO_2/$Cs_2AgBiBr_6$ layer in Chapter 4.[9] The high $\Delta\sigma_{max}$ of *n*/*i* double layer could be originated from holes remaining in the photoabsorber and/or electrons in mp-TiO_2. Regardless of these two possibilities, the observed increase in $\Delta\sigma_{max}$ suggests that (i) the electron mobilities in these Sb-based materials are lower than that in TiO_2 (~0.1 $cm^2V^{-1}s^{-1}$),[37] where the interdigitated mesoporous ETM structure benefits the high yield of the ET process and (ii) the charge carrier density at the pulse end is increased (=charge recombination is reduced by extracting electrons). Thus, the large $\Delta\sigma_{max}$ of *n*/*i* double layer reflects efficient electron transport.

Based on the TRMC results of double layers and energetic assessments, the author expected the five most plausible materials to be SbSI, Sb-S-Br, Sb_2S_3, $CsSbSI_2$, and $MASbSI_2$, out of the 44 candidates. Interestingly, it was found that the ET was exceptionally efficient in a few Sb-based materials, despite the fact that other materials have CBM levels shallower than that of TiO_2. This suggests that a favorable band bending may occur at TiO_2/Sb-based materials interface or unfavorable energy barrier appears at TiO_2/Bi-based materials interface.

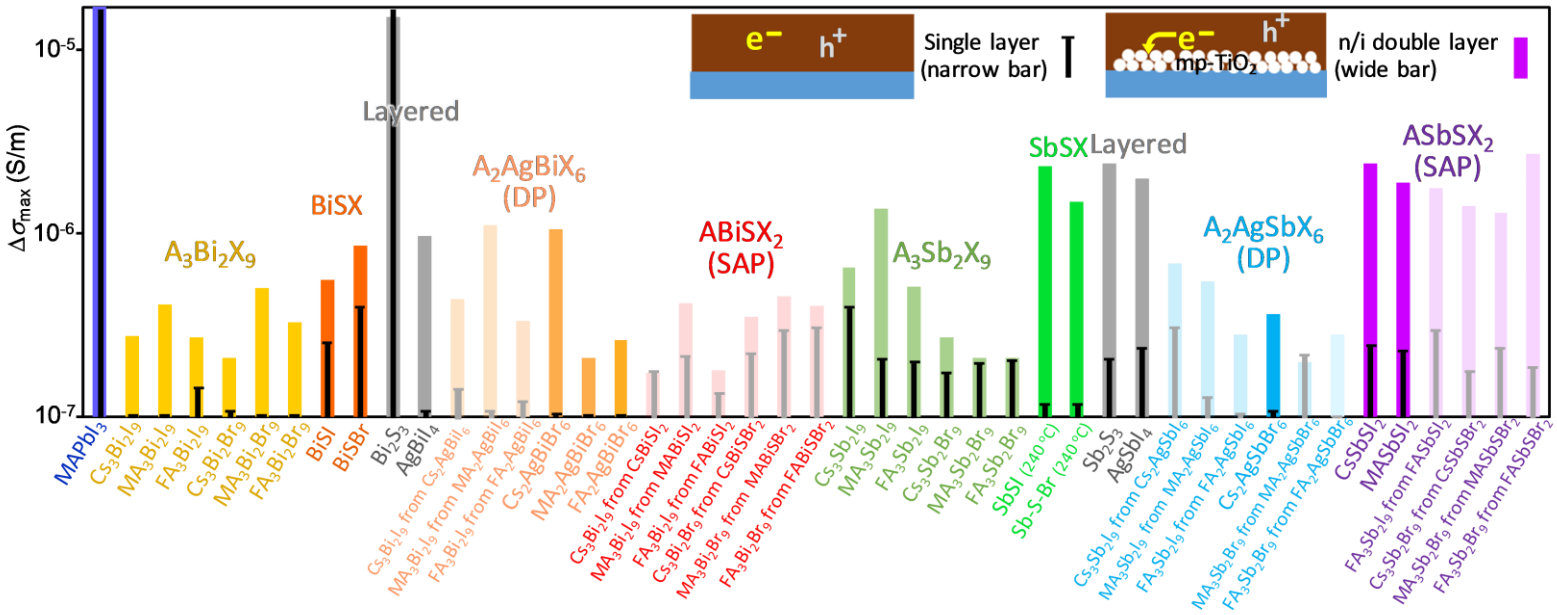

Figure 5-4. Photoconductivity transient maxima ($\Delta\sigma_{max}$) obtained from Xe-flash TRMC measurements. The narrow black bars and wide colored bars represent single active layer and mp-TiO_2/active layer (*n*/*i*), respectively.

5-2-4. Statistical analysis of TRMC results and solar cell performance

n-i-p solar cells (glass/FTO/compact-TiO_2/mp-TiO_2/absorber/HTM/Au, see Experimental) were fabricated and characterized for the materials that exhibited bandgaps smaller than 2.2 eV (for DP, smaller than 2.6 eV). The summary of a total of 29 materials are provided in Table 5-4. Among the devices using poly(tri-arylamine) (PTAA) with dopant as the HTM, $Cs_2AgBiBr_6$ (DP) exhibited a relatively high PCE of 0.72% along with a low short-circuit current density (J_{SC}) of 1.2 mA cm^{-2}, high open-circuit voltage (V_{OC}) of 0.93 V. However, the use of cychlopentadithiophene-benzothiadiazole copolymer (PCPDTBT) without dopant as HTM significantly suppressed its PCE to 0.3%, whereas $CsSbSI_2$, Sb_2S_3, and SbSI (annealed at 240 ℃) showed improvement in its PCE of 0.92%, 1.16%, and 1.35%, respectively, mainly owing to the increased J_{SC} (4.6–9.1 mA cm^{-2}).

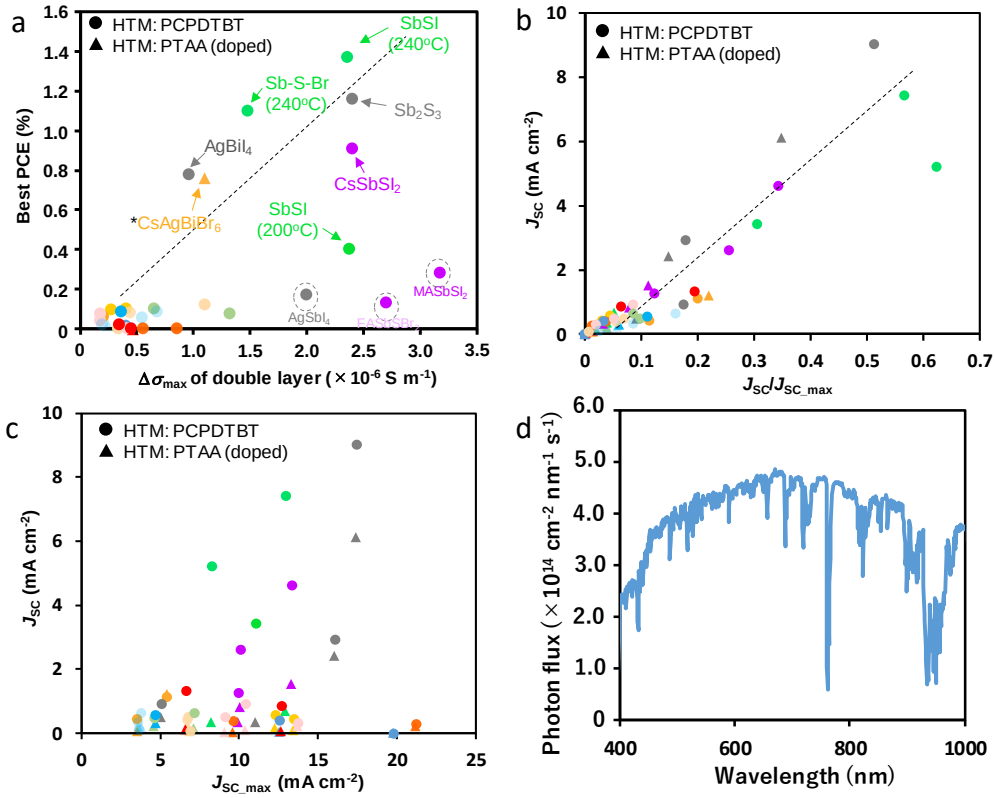

Figure 5-5. (a) Best PCE vs $\Delta\sigma_{max}$ of double layer (mp-TiO_2/active layer) obtained from Xe-flash TRMC. PTAA with dopant (triangles) and PCPDTBT without dopant (circles) were used as HTM. The color represents a crystal type as shown in Figure 5-2, 5-4. The dotted line is an eye-guide. (b) J_{SC} vs J_{SC}/J_{SC_max} and (c) J_{SC} vs J_{SC_max} plot obtained from the device results and calculation of J_{SC_max} (eq. 5-1). (d) Photon flux of AM1.5G sun light obtained from NREL.[38]

To examine the correlation between device performances and TRMC results, the best PCE of solar cells obtained using either PTAA or PCPDTBT as an HTM were plotted as a function of $\Delta\sigma_{max}$ of *n*/*i* double layers (Figure 5-5a). A nearly linear correlation was observed with moderate correlation factor (*r*) of 0.59, demonstrating that TRMC measurements are useful for the exploration of Bi- and Sb-based photoabsorbers. $AgSbI_4$, $MASbSI_2$, and $FASbSBr_2$ surrounded by dotted circles in Figure 5-5a are located far below the linear trend, which is presumably explained by inefficient hole transfer (HT) to HTM. The poor HT yield would be linked to the contamination of $A_3M_2X_9$ phase for $MASbSI_2$ and $FASbSBr_2$ and the instability for $AgSbI_4$ that easily turns transparent by exposing to the air for 1 h. Curiously, $Cs_2AgBiBr_6$, SbSI (annealed at 200 and 240 ℃), and Sb-S-Br (annealed at 240 ℃) devices showed a significant difference in PCE by changing HTM (for example, 0.16% for PTAA and 1.35% for PCPDTBT in the case of SbSI annealed at 240 ℃, see Table 5-4). This indicates the importance of the selection of HTMs.

Because J_{SC} strongly predominate PCE (r = 0.93 for PCE vs J_{SC}, r = 0.43 for PCE vs V_{OC}, and r = 0.34 for PCE vs FF), the predominant factor of J_{SC} was studied through J_{SC}/J_{SC_max} analysis (Figure 5-5b, c), where J_{SC_max} is the achievable J_{SC} at maximum calculated from the integration of complementary transmittance and sunlight spectra (see Figure 5-5d). The calculation is as follows;

$$J_{SC\_max} = -e \int_0^{\lambda a} P(\lambda)\{1 - T(\lambda)\}d\lambda \qquad (5\text{-}1)$$

, where e is the elemental charge, λ_a is the absorption edge, $P(\lambda)$ is the photon flux of the solar spectrum, and $T(\lambda)$ is the transmittance of mp-TiO_2/photoabsorber double layer. The refection was ignored in this calculation. The J_{SC} vs J_{SC}/J_{SC_max} plot showed a good linear correlation (r = 0.92), whereas the J_{SC} vs J_{SC_max} plot was scattered (r = 0.31). Thus, the device performance is strongly affected by the efficiency of exciton separation and charge extraction rather than photoabsorption associated with the film thickness. Consequently, the author decided to focus on Sb_2S_3-containing SbSI annealed at 240 ℃, which revealed the highest $\Delta\sigma_{max}$ (except for $MAPbI_3$ and Bi_2S_3) and PCE, despite the fact that it remains mostly unexplored thus far.

Table 5-4. Summary of solar cell performances with various active layer.

	HTM: PTAA					HTM: PCPDTBT				
Materials	J_{SC} (mA cm^{-2})	J_{SC} / J_{SC_max} [a]	V_{OC} (V)	FF	PCE (%)	J_{SC} (mA cm^{-2})	J_{SC} / J_{SC_max} [a]	V_{OC} (V)	FF	PCE (%)
$Cs_3Bi_2I_9$	0.082	0.0061	0.29	0.37	8.9×10^{-3}	0.41	0.030	0.48	0.49	0.098
$MA_3Bi_2I_9$	0.12	0.0097	0.34	0.41	0.016	0.55	0.045	0.38	0.48	0.1
BiSI	0.19	0.0085	0.0024	0.085	4.0×10^{-5}	0.078	0.012	0.032	0.27	6.5×10^{-4}
BiSBr	0	0	0	0	0	0.36	0.037	0.003	0.16	2.0×10^{-4}
Bi_2S_3	0	0	0	0	0	0	0	0	0	0
$AgBiI_4$	2.4	0.149	0.49	0.55	0.65	2.9	0.18	0.47	0.59	0.78
$Cs_3Bi_2I_9$ from Cs_2AgBiI_6 precursor	0.073	0.011	0.35	0.42	0.011	0.26	0.056	0.34	0.56	0.05
$MA_3Bi_2I_9$ from MA_2AgBiI_6 precursor	0.24	0.035	0.48	0.5	0.057	0.48	0.070	0.39	0.65	0.12
$FA_3Bi_2I_9$ from FA_2AgBiI_6 precursor	0.028	0.0041	0.13	0.38	1.4×10^{-3}	0.0051	0.0074	0.19	0.35	3.4×10^{-3}
$Cs_2AgBiBr_6$	1.2	0.22	0.95	0.67	0.76	1.1	0.20	0.46	0.59	0.31
$Cs_3Bi_2I_9$ from $CsBiSI_2$ precursor	0.078	0.0074	0.032	0.27	6.5×10^{-4}	0.90	0.086	0.23	0.37	0.077
$MA_3Bi_2I_9$ from $MABiSI_2$ precursor	0.19	0.014	0.036	0.27	1.9×10^{-3}	0.29	0.020	0.012	0.22	7.6×10^{-4}
$FA_3Bi_2I_9$ from $FABiSI_2$ precursor	0.017	0.0019	0.11	0.36	7.1×10^{-4}	0.48	0.053	0.22	0.39	0.041
$Cs_3Bi_2Br_9$ from $CsBiSBr_2$ precursor	0.042	0.014	0.012	0.25	1.2×10^{-4}	0.6	0.19	0.062	0.27	0.01
$MA_3Bi_2Br_9$ from $MABiSBr_2$ precursor	0.032	0.0025	0.0059	0.16	3.1×10^{-5}	0.83	0.065	0.017	0.23	3.2×10^{-3}
$FA_3Bi_2Br_9$ from $FABiSBr_2$ precursor	0.41	0.0018	0.14	0.34	0.019	0.022	0.033	0.1	0.36	8.1×10^{-4}
$Cs_3Sb_2I_9$	0.14	0.020	0.24	0.6	0.021	0.62	0.086	0.37	0.44	0.1
$MA_3Sb_2I_9$	0.18	0.039	0.32	0.49	0.028	0.46	0.099	0.29	0.54	0.074
SbSI (200 ℃)	0.31	0.028	0.20	0.37	0.023	3.4	0.31	0.31	0.38	0.40
SbSI (240 ℃)	0.67	0.051	0.42	0.56	0.16	7.1	0.57	0.37	0.53	1.35
Sb-S-Br (240 ℃)	0.33	0.040	0.41	0.56	0.076	5.2	0.62	0.4	0.53	1.1
Sb_2S_3	6.1	0.35	0.41	0.39	0.98	9	0.51	0.29	0.44	1.16
$AgSbI_4$	0.17	0.092	0.32	0.56	0.031	0.9	0.18	0.33	0.59	0.17

$Cs_3Sb_2I_9$ from Cs_2AgSbI_6 precursor	0.15	0.039	0.34	0.46	0.023	0.62	0.16	0.25	0.56	0.087
$MA_3Sb_2I_9$ from MA_2AgSbI_6 precursor	0.21	0.058	0.39	0.52	0.044	0.31	0.085	0.31	0.59	0.057
$Cs_2AgSbBr_6$	0.29	0.061	0.46	0.5	0.068	0.53	0.11	0.37	0.45	0.088
$CsSbSI_2$	1.5	0.022	0.43	0.47	0.31	4.6	0.025	0.38	0.53	0.92
$MASbSI_2$	0.8	0.11	0.35	0.46	0.13	2.6	0.34	0.22	0.48	0.27
$FA_3Sb_2Br_9$ from $FASbSBr_2$ precursor	0.32	0.079	0.31	0.42	0.04	1.24	0.26	0.24	0.44	0.13

[a] J_{SC_max} is the maximum J_{SC} calculated from the transmittance of mp-TiO_2/active layer and sunlight spectrum, as represented in eq. 5-1.

5-2-5. The Effect of the HTM structures

A dramatic improvement in Sb_2S_3-containing SbSI solar cells by changing the HTM from PTAA (PCE = 0.16%) to PCPDTBT (PCE = 1.35%) underscores the importance of HTM selection. Therefore, the author examined polymeric HTM (PTAA with dopant, PCPDTBT, and regioregular poly(3-hexylthiophene): P3HT), molecular

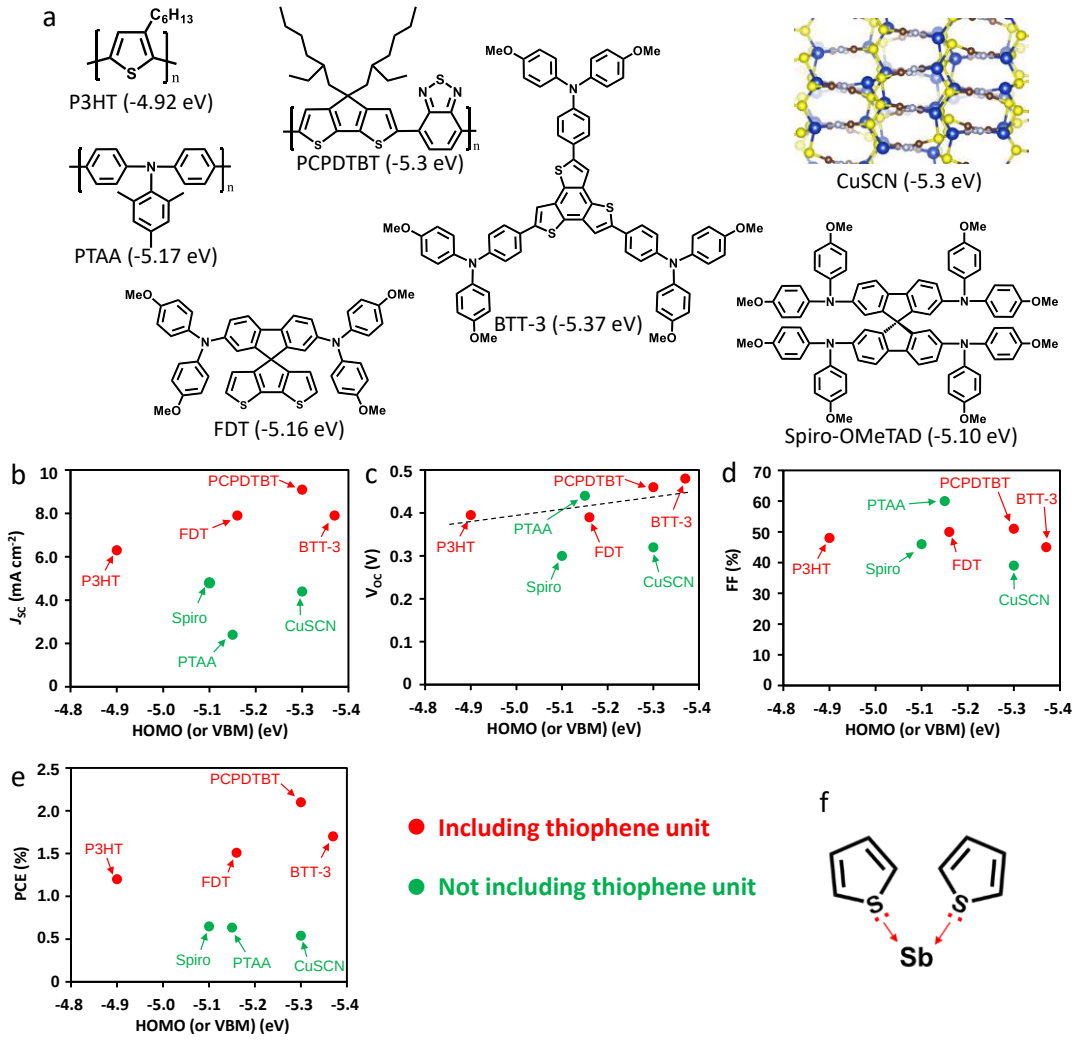

Figure 5-6. (a) Chemical (or crystal) structures of HTMs (P3HT,[30] PTAA,[30] PCPDTBT,[42] FDT,[39] BTT-3,[40] Spiro-OMeTAD,[30] and CuSCN[41]) used for SbSI devices. The HOMO (or VBM) levels taken from the corresponding references are appended. (b) J_{SC}, (c) V_{OC}, (d) FF, and (e) PCE vs. HOMO (or VBM) level of each HTM. Dopants were added in PTAA and molecular HTM (Spiro-OMeTAD, FDT, and BTT-3). (f) Schematic of coordination from the thiophene unit of HTM to the Sb ion at the surface of the Sb-based photoabsorber.

HTM (2,2',7,7'-tetrakis[*N*,*N*-di(4-methoxyphenyl)amino]-9,9'-spirobifluorene: Spiro-OMeTAD with dopant, FDT with dopant,[39] and BTT-3 with dopant[40]), and inorganic HTM (CuSCN[41]) (Figure 5-6a). The corresponding device performance is summarized in Table 5-5. To ensure the ohmic contact between the HTM and the Au electrode, a PEDOT:PSS layer was inserted between them (the device structure is drawn in Experimental; MoO_3/Ag is an alternative, but unsuccessful), resulting in an improved PCE (from 1.35% to 1.81%) (Table 5-6).[22] Double-spin-coated SbSI was also found to slightly improve the PCE (2.01%).

J_{SC}, V_{OC}, FF, and PCE vs. the highest occupied molecular orbital (HOMO) levels of the HTMs are displayed in Figure 5-6b–e, respectively. Notably, the HTMs including thiophene units (P3HT, PCPDTBT, FDT, and BTT-3 plotted by red circles) afforded the higher PCE than the others (PTAA, Spiro-OMeTAD, and CuSCN plotted by green circles), among which the best PCE of 2.01% (J_{SC} = 9.2 mA cm^{-2}, V_{OC} = 0.46 V, and FF = 48%) was obtained for PCPDTBT. This result indicates that thiophene unit greatly enhanced the hole transport, while the impact of the HTM HOMO level was insignificant. The reason for the enhanced device characteristics is likely the coordination of the thiophene lone pair on the active layer surface, as suggested in the Sb_2S_3/PCPDTBT interface (Figure 5-6f).[42] Such a surface interaction would facilitate the hole transport to the HTM, leading to an increase in J_{SC} and V_{OC}. It is also notable that molecular HTMs (especially BTT-3) afforded relatively high V_{OC} (0.52–0.61 V), even without the PEDOT:PSS layer. This is likely because of the easy penetration of a single molecule into the SbSI layer preferable for efficient surface passivation. The introduction of the PEDOT:PSS layer further increases J_{SC}, whereas the V_{OC} was slightly decreased.

Table 5-5. Summary of Sb_2S_3-containing SbSI solar cells with various HTMs.

HTM	HOMO (eV)	J_{SC} (mA cm^{-2})	V_{OC} (V)	FF	PCE (%)
PTAA	−5.15[30]	2.4	0.24	0.60	0.63
P3HT	−4.9[30]	6.3	0.40	0.48	1.2
PCPDTBT	−5.3[42]	9.2	0.46	0.48	2.01
Spiro-OMeTAD	−5.1[30]	4.8	0.30	0.46	0.65
FDT	−5.16[39]	7.9	0.39	0.50	1.5
BTT-3	−5.37[40]	7.9	0.48	0.45	1.7
CuSCN	−5.3[41]	4.4	0.32	0.39	0.54

5-2-6. Improvement of Sb_2S_3-containing SbSI solar cell

The critical issue to be addressed in the SbSI device is the large V_{OC} loss of 1.33 eV (Table 5-4) relative to its optical bandgap (1.73 eV). This can be attributed to the many pinholes observed in the image obtained by scanning electron microscopy (SEM) (Figure 5-7a); these pinholes cause the shortening of the diode circuit. Notably, V_{OC} was successfully improved by introducing the pre-deposition of a thin SbSI layer and double spin-coating (finally 200 nm in thickness) (Table 5-6 and Experimental). Consequently, a maximum PCE of 2.91% (J_{SC} = 12.0 mA cm^{-2}, V_{OC} = 0.47 V, and FF = 52%) was obtained (Figure 5-7b, average PCE = 2.4 ± 0.5%) by using PCPDTBT as the HTM.

The external quantum efficiency (EQE) spectra was in good agreement with the photoabsorption spectra given by the complementary of the transmittance (Figure 5-7c). The maximum EQE was 59% at 390 nm, and the integrated J_{SC} over the EQE spectrum (10.2 mA cm^{-2}) was consistent with the J_{SC} under one sun (10.3 mA cm^{-2} for the corresponding cell). The PCE of Sb_2S_3-containing SbSI was mostly comparable to the

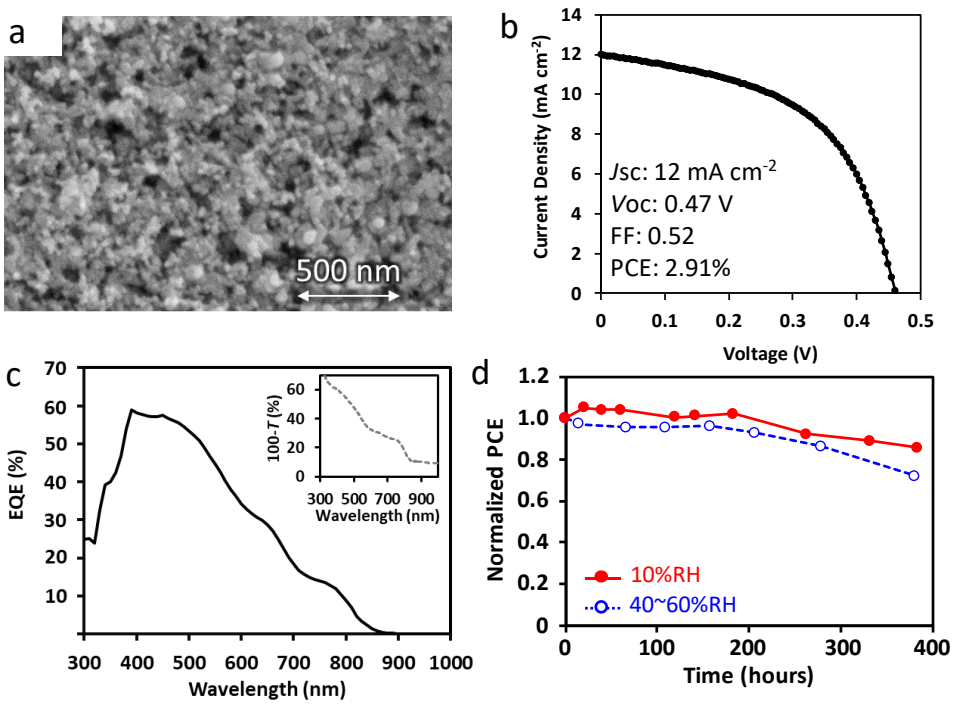

Figure 5-7. (a) SEM image of the Sb_2S_3-containing SbSI surface. (b) *J-V* curve of the best performing cell. The obtained parameters are appended. (c) EQE spectrum of a SbSI device. The inset is the photoabsorption spectrum of an Sb_2S_3-containing SbSI film (100−*T*%, *T* is transmittance). (d) Normalized PCE as a function of storage time under dried condition (~10%RH, solid line) and high humidity (40~60%RH, dot line) under room light.

3.05% reported by Nie *et al*., where step-by-step deposition with CBD and spin-coating was used.[19] However, the author's SbSI film was prepared by a new, facile spin-coating of dimethyl sulfoxide (DMSO) solution of the ethylxanthate complex of $Sb(EtXa)_3$ and SbI_3 (3:4 in mol%) followed by thermal annealing. Additionally, the device showed good stability in dried air (~10%RH) and humid air (40~60%RH) and kept 86% and 72% of initial PCE for 16 days, respectively (Figures 5-7d). This chapter presented the demonstration of the effective screening of Pb-free solar cells under the guidance of TRMC and photoabsorption/photoelectron spectroscopies, among which the Sb_2S_3-containing SbSI with thiophene-containing HTM was identified as the most promising candidate.

Table 5-6. Summary of Sb_2S_3-containing SbSI/PCPDTBT-based device performance.

Device structure[a)]	Mask size (mm^2)	J_{SC} (mA cm^{-2})	V_{OC} (V)	FF	PCE (%)
A	3.14	7.1	0.37	0.53	1.35
B	3.14	8.5	0.40	0.52	1.81
B, double spin-coat	9.00	9.2	0.46	0.48	2.01
B, pre-deposition and double spin-coat	9.00	9.1	0.48	0.49	2.10
B, pre-deposition and double spin-coat	4.00	12.0	0.47	0.52	2.91

[a)]Device structure A: FTO/compact-TiO_2/mp-TiO_2/SbSI/PCPDTBT/Au. Device structure B: FTO/compact-TiO_2/mp-TiO_2/SbSI/PCPDTBT/PEDOT:PSS/Au. The detail of double spin-coat and pre-deposition are described in Experimental.

5-3. Conclusion

In conclusion, the author conducted a comprehensive survey on Bi and Sb-based semiconducting materials with 6 structural categories and 44 compositions, considering crystal phase formation (XRD), bandgap (UV-vis), VBM (PYS), and photoconductivity/charge transfer (TRMC). Consequently, the Sb-based MSX, Sb_2S_3, $AgSbI_4$, and SAP showed higher solar cell performances than the others, as suggested from the 10-fold increase in $\Delta\sigma_{max}$ of TRMC in the mp-TiO_2/active layer compared with the single layer. The increased $\Delta\sigma_{max}$ is understood from the efficient electron transfer to mp-TiO_2 and reduced charge recombination. Among the candidates, Sb_2S_3-containing SbSI prepared by a new method with the use of $Sb(EtXa)_3$ exhibited the top-level $\Delta\sigma_{max}$ and PCE; thus, further device optimization (insertion of PEDOT:PSS, screening of HTM, and a repeat of active layer coating) was applied. Interestingly, the inclusion of a thiophene unit in the HTM, rather than the HOMO level, greatly impacted the PCE, leading to an improved PCE of 2.91%. Importantly, these results indicate that even if the charge carrier mobility of active layer is much lower than the typical LHP, efficient charge extraction and improvement of solar cell efficiency are possible by the rational combination of the active layer and HTM. These findings on the photoabsorber composition, the HTM structure, and the premiere indicator of $\Delta\sigma_{max}$ of *n*/*i* double layer will help a further exploration and development of Pb-free solar cells.

5-4. Experimental

5-4-1. Preparation

Materials

CsI, MAI, FAI, CsBr, MABr, FABr, thiourea, and potassium ethylxanthate were purchased from Tokyo Chemical Industry (TCI) Co., Ltd. BiI_3, $BiBr_3$, $BiCl_3$, $Bi(OAc)_3$, SbI_3, $SbBr_3$, $SbCl_3$, $Sb(OAc)_3$, AgI, and AgBr were bought from Sigma-Aldrich Co., Ltd. Super dehydrated grade DMSO were purchased from Wako Chemical Industries Ltd. All chemicals were used without further purification. $Bi(OAc)_3$, $Sb(OAc)_3$, and thiourea were used for the preparation of Bi_2S_3 and Sb_2S_3 film through CASC process. $BiCl_3$, $SbCl_3$, and potassium ethylxanthate were used for the synthesis of $Bi(EtXa)_3$ and $Sb(EtXa)_3$. Other chemicals were used for the preparation of $A_3M_2X_9$, MSX, $AgMX_4$, DP and SAP films.

Synthesis of $Bi(EtXa)_3$ and $Sb(EtXa)_3$

$Bi(EtXa)_3$ was synthesized by the reported process.[34] For $Sb(EtXa)_3$ preparation, 912 mg $SbCl_3$ was dissolved in 8 mL methanol. Then, 12 mL potassium xanthate solution (1 M) was added to obtain pale yellow precipitation. After the removal of the upper solution, $Sb(EtXa)_3$ was extracted by chloroform from the precipitation. The extracted solution was evaporated to remove excess amount of chloroform before recrystallization. The recrystallization of $Sb(EtXa)_3$ were repeated 2 times to remove contamination. Finally, high purity $Sb(EtXa)_3$ yellow single crystal was obtained (99.99% metal basis, analyzed by EDX).

Film preparation of $A_3M_2X_9$, MSX, $AgMX_4$, DPs and SAPs photoabsorbers

All the materials were dissolved in anhydrous DMSO. For $A_3M_2X_9$, AX and MX_3 were dissolved at 0.75 and 0.5 M, respectively. For MSX, MX_3 and $M(EtXa)_3$ were dissolved at 0.4 and 0.3 M, respectively. The solution was diluted with DMSO for double spin-coating (precursor : DMSO = 1 : 0.5) and pre-deposition (precursor : DMSO = 1 : 3). For $AgMX_4$, AgX and MX_3 were dissolved at 0.5 M. For A_2AgMX_6 (DPs), AX, AgX, and MX_3 were dissolved at 0.5, 0.25, and 0.25 M, respectively. For $AMSX_2$ (SAPs), AX, MX_3, and $M(EtXa)_3$ were dissolved at 0.5, 0.25, and 0.25 M, respectively. Each solution was spin-coated onto a bare quartz or mp-TiO_2 at 2000 rpm for 30 s. The optimum annealing temperatures were 110 °C for $A_3M_2X_9$ and $AgMX_4$, 200–240 ℃ for MSX, 150 ℃ for DP except for $Cs_2AgBiBr_6$ (250 ℃ for $Cs_2AgBiBr_6$), and 150 ℃ for SAP. The annealing time was 10 min for all. 5 vol% of HI aqueous solution (57 wt%) was added into the precursor

solution of $A_3Bi_2I_9$, BiSI, A_2AgBiI_3, and $AgBiI_4$ to increase the solubility and to prevent lack of iodide. Whereas, HI addition to Sb-based materials resulted in deteriorated TRMC signal and device performance. All the procedure was carried out inside a grove box (O_2 < 0 ppm, H_2O < 0 ppm).

5-4-2. Fundamental characterization

PYS, XRD, UV-vis, and EDX

The VBM levels were measured by PYS using a Bunko Keiki Corp. BIP-KV201 (accuracy: ±0.02 eV, extraction voltage = 10 V) in a vacuum (< 10^{-2} Pa). The film was prepared onto an F-doped SnO_2 (FTO) layer on a glass substrate, which was contacted through aluminum tape and an Au-coated electrode. The profiles are provided in Figure 5-8, 5-9. XRD was performed by using a Rigaku Corp. MiniFlex-600 instrument (Cu Kα radiation: λ = 1.54 Å) in the air at room temperature. The photoabsorption spectra were measured using a Jasco Corp. V-730. Tauc plots were also obtained from absorption spectra. The profiles are given in Figure 5-10, 5-11. EDX measurements of power samples

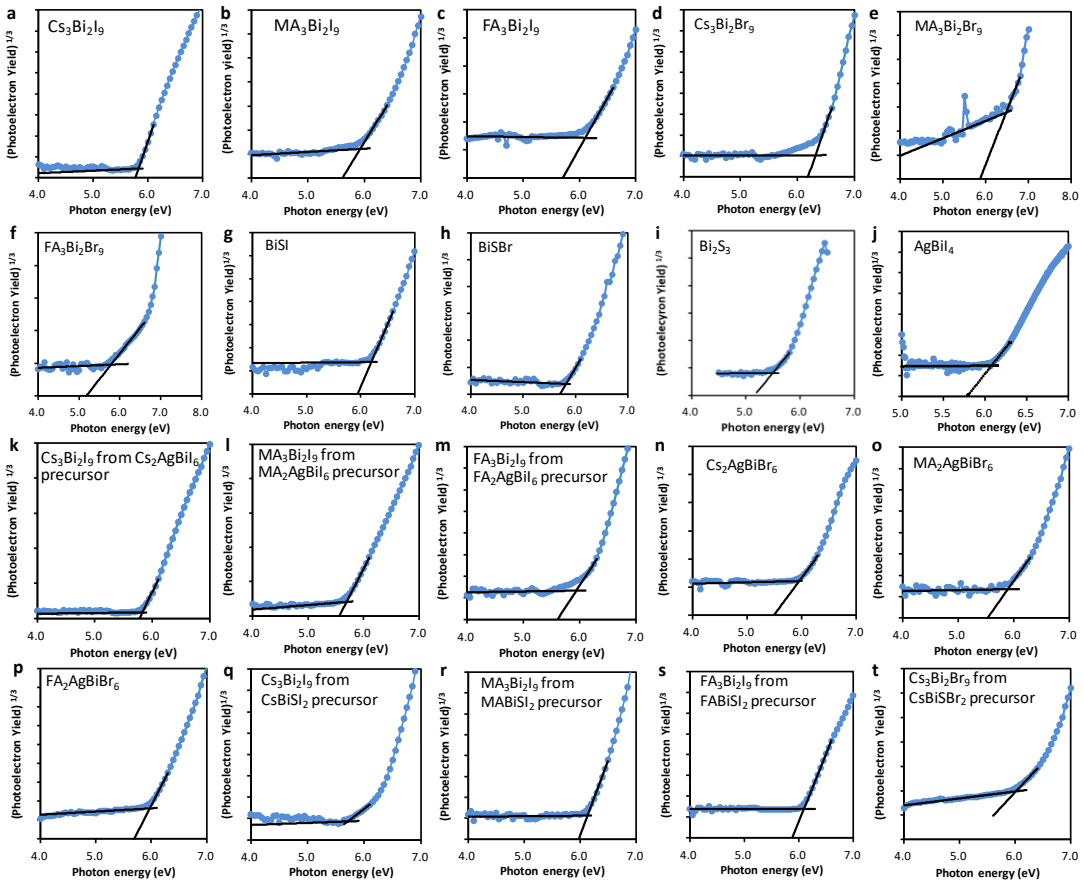

Figure 5-8. PYS spectra of each film. The samples were prepared on FTO substrates.

prepared by drop cast of precursor solution were performed using a Malvern-Panalytical Epsion 1. The film thickness was measured using a Bruker Dektak XT surface profiler.

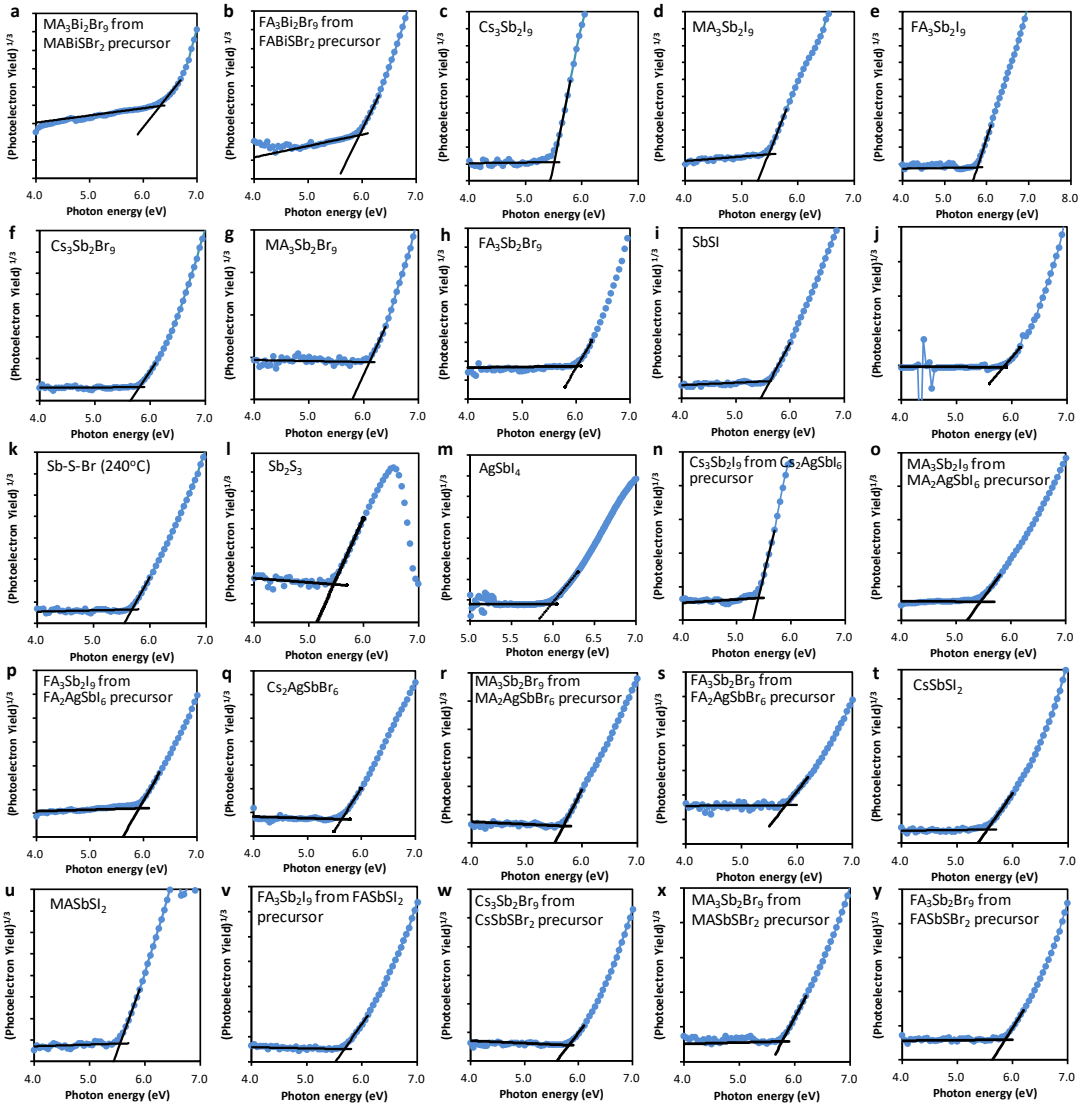

Figure 5-9. PYS spectra of each film. The samples were prepared on FTO substrates.

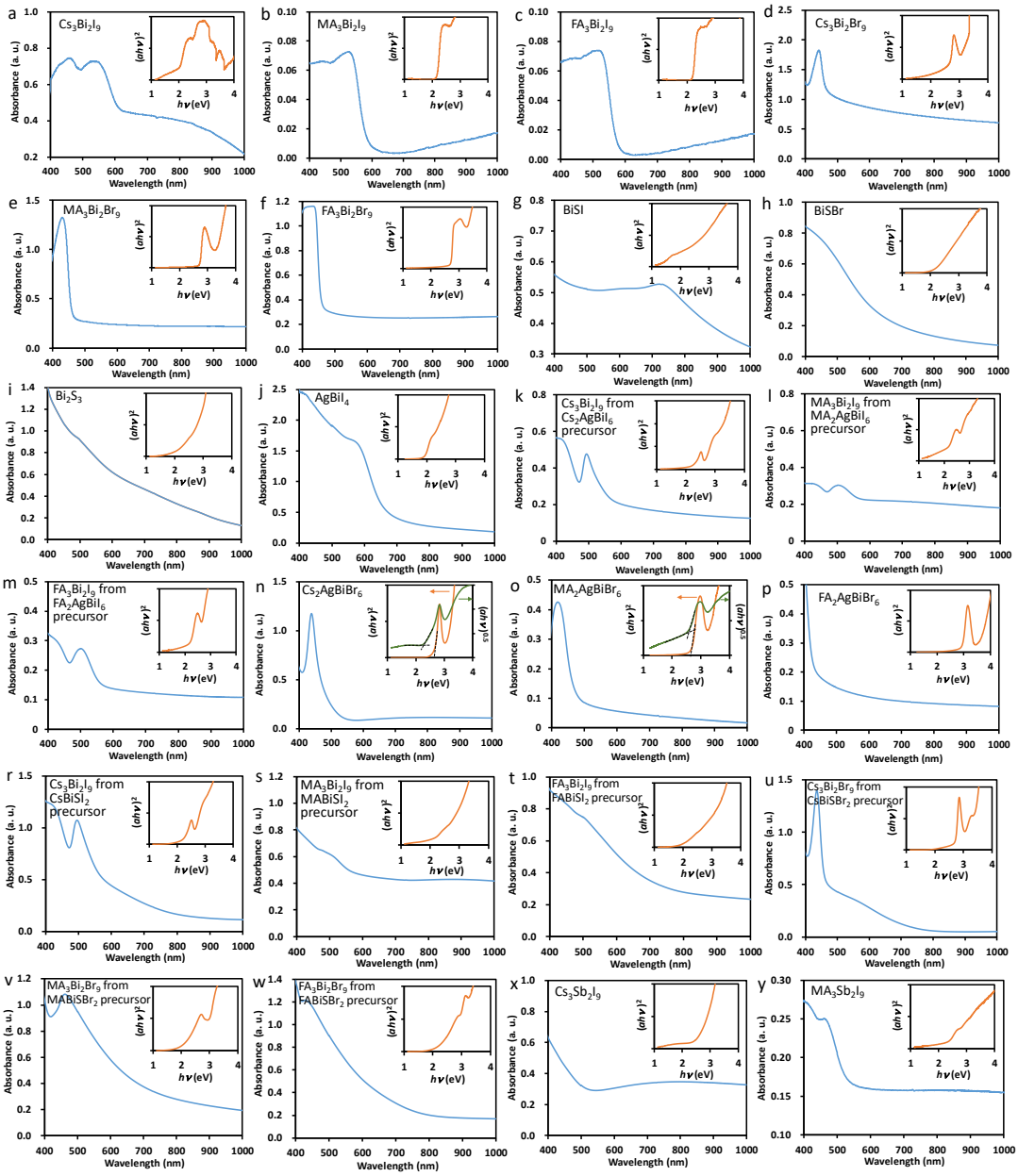

Figure 5-10. Photoabsorption spectra of each film. The samples were prepared on quartz substrate.

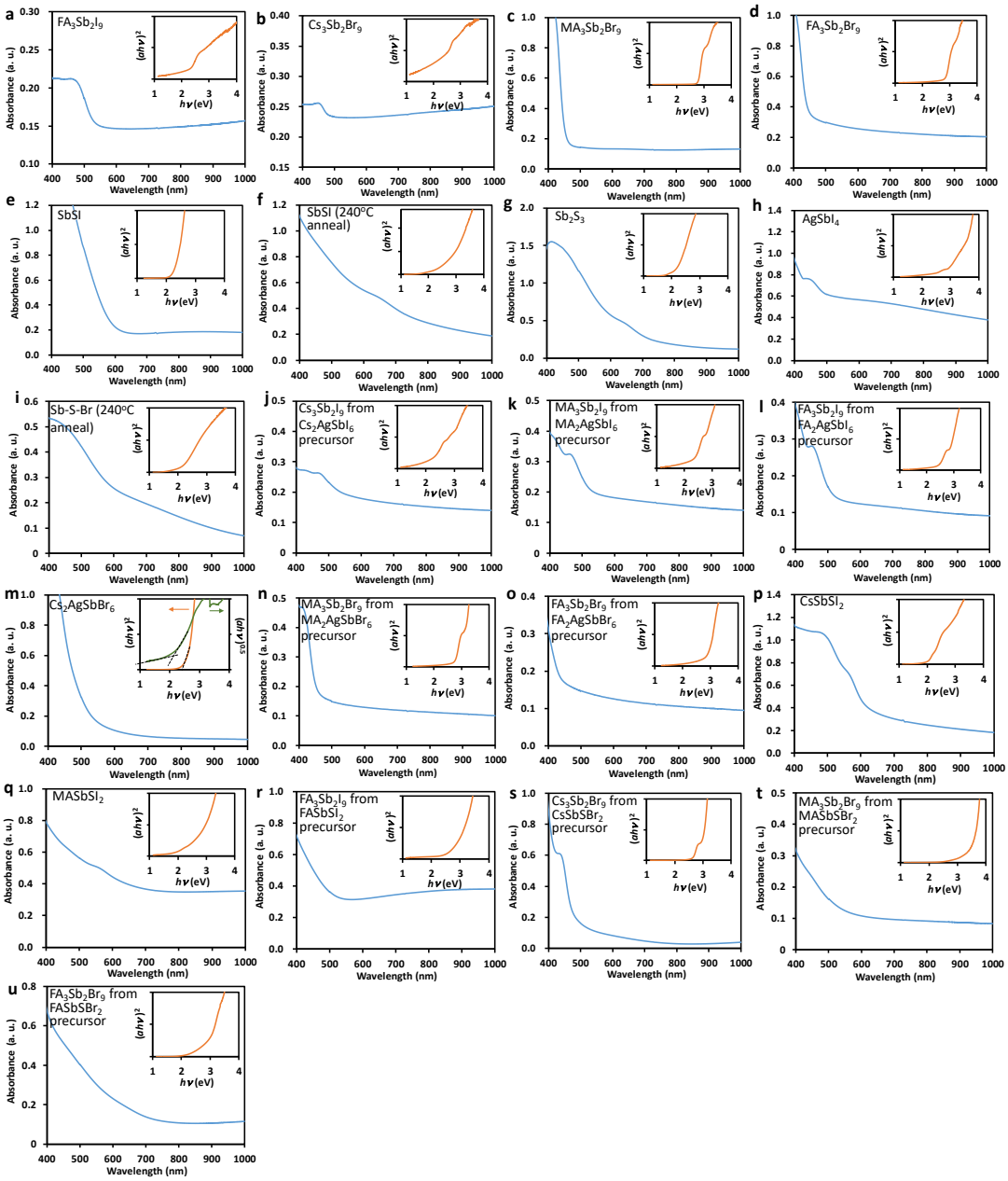

Figure 5-11. Photoabsorption spectra of each film. The samples were prepared on quartz substrate.

TRMC measurement

Thin films were prepared on quartz plates and mp-TiO_2/quartz. The sample was set in a resonant cavity and probed by continuous microwave at ca. 9.1 GHz. A pseudo-sunlight, white light pulse (width ~10 μs) from an in-house Xe-flash lamp was exposed to the sample, and the change in the microwave power reflected from the cavity was amplified by a field effect transistor amplifier, detected by a detector, and recorded by an oscilloscope. The photoconductivity transient $\Delta\sigma$ was calculated by equation 1-5 as described in Chapter 1. All experiments were conducted at room temperature in air. The original decays are provided in Figure 5-12, 5-13.

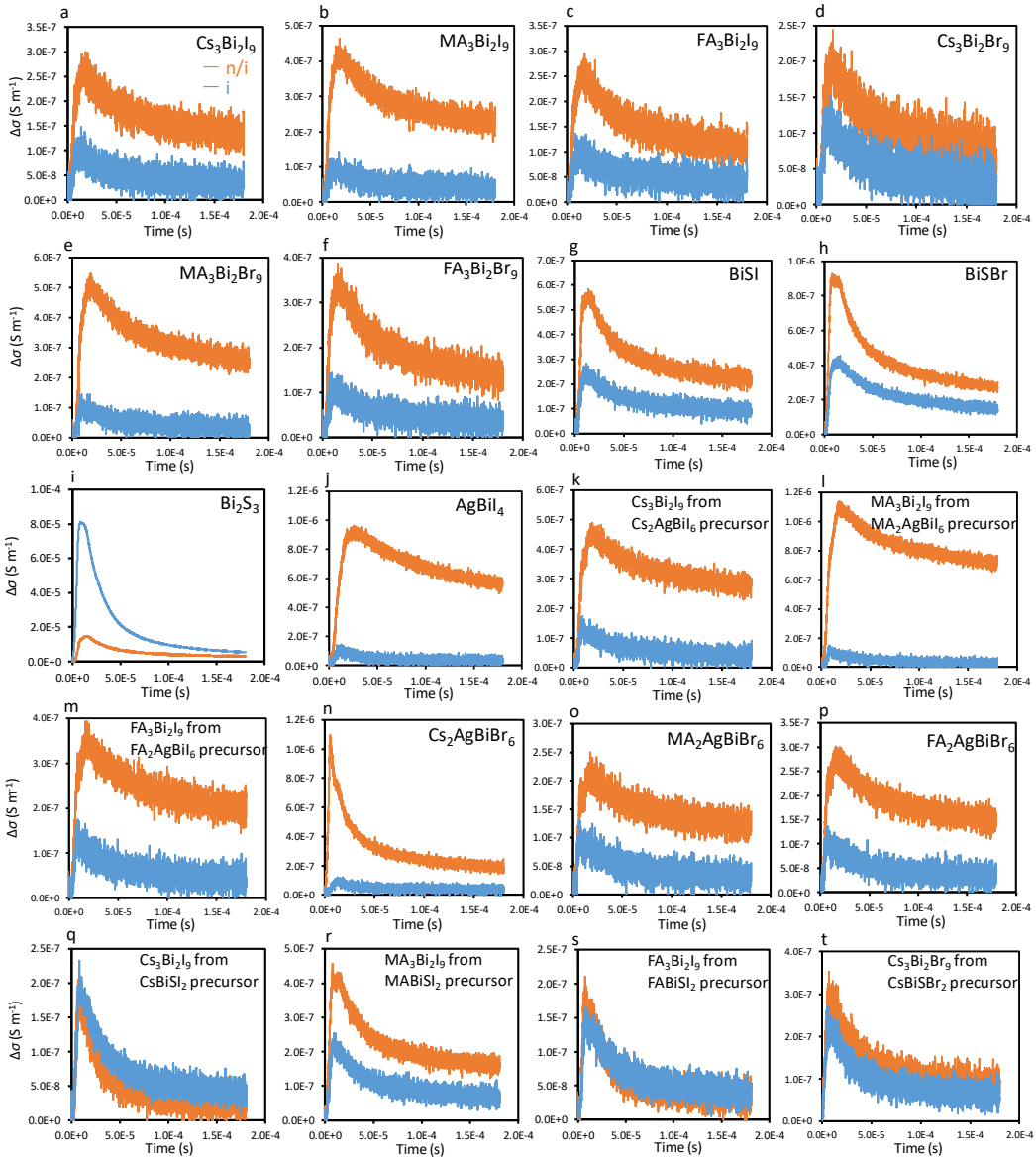

Figure 5-12. Xe-flash TRMC decays of films on mp-TiO_2/quartz and bare quartz. All the measurements were conducted in air.

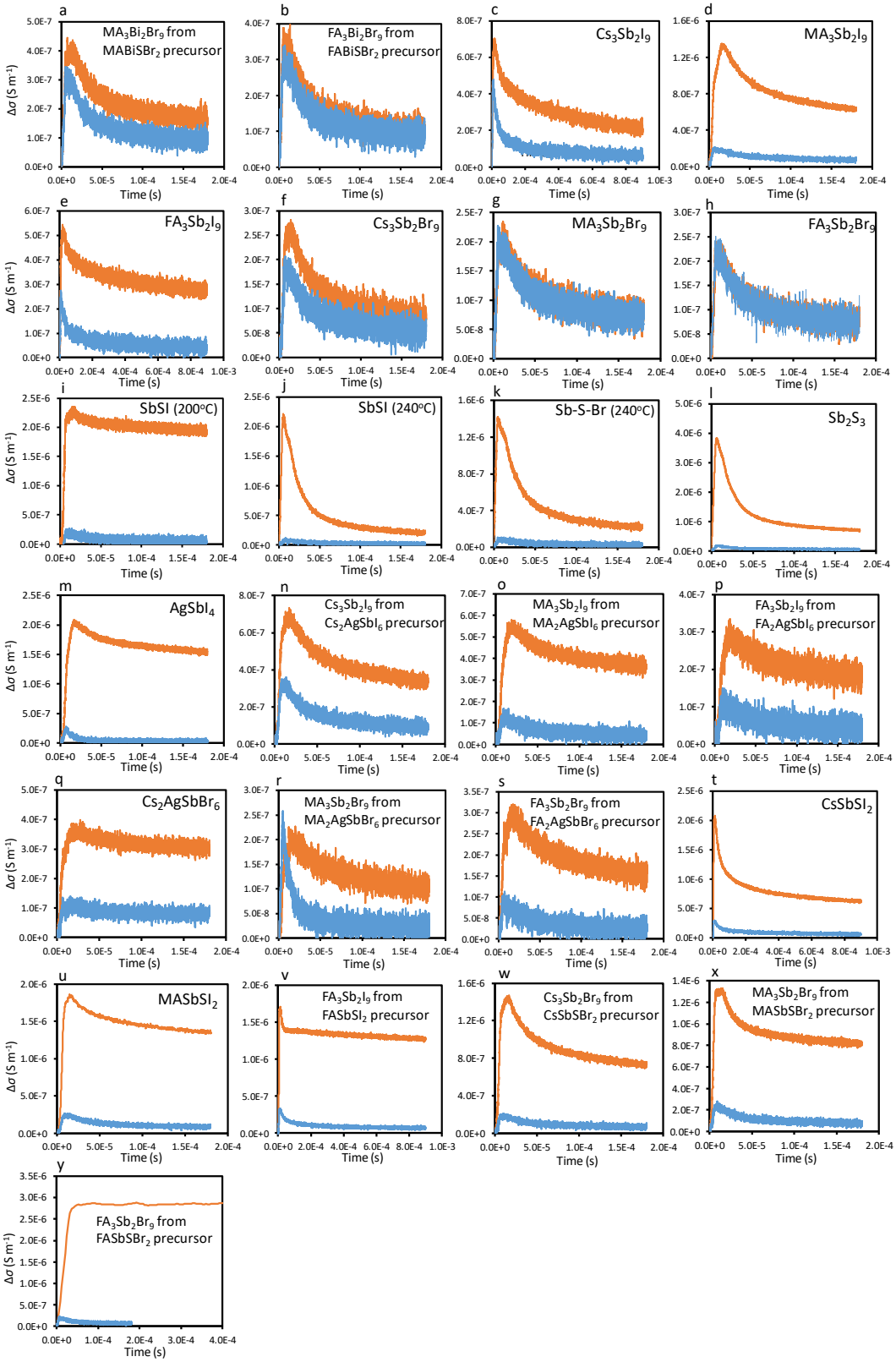

Figure 5-13. Xe-flash TRMC decays of films on mp-TiO_2/quartz and bare quartz. All the measurements were conducted in air.

5-4-3. Device Fabrication

A fluorine-doped tin oxide (FTO) substrate was cleaned with detergent, isopropyl alcohol, and deionized water, and a compact TiO_2 layer was deposited onto the FTO by spray pyrolysis using a solution of titanium diisopropoxide bis(acetylacetonate) (Sigma Aldrich) in ethanol (1:40 v/v) at 450 ℃. A 200 nm-thick mp-TiO_2 layer was deposited onto the compact TiO_2 layer by spin-coating (5000 rpm, 30 s) of a diluted TiO_2 paste (30 NR-D) in ethanol (paste/ethanol = 1:7 w/w), followed by annealing at 125 ℃ for 5–20 min and sintering at 500 ℃ for 20 min. A precursor solution was spin-coated onto the substrates and annealed. For double spin-coating of SbSI, the diluted precursor solution was spin-coated and annealed (150 ℃, 2 min), followed by a second spin-coating and annealing (240 ℃, 10 min). For the pre-deposition of thin SbSI, the diluted precursor solution was spin-coated (4000 rpm, 30 s), and annealed (240 ℃, 10 min) before double spin-coating. The schematics of these process are represented in Figure 5-14. The HTM solution was prepared with following composition: 10 mg/mL PTAA toluene solution with Li-TFSI and 4-tert-butylpyridine (tBP) (PTAA : Li-TFSI : tBP = 1 : 0.15 : 1.4 for weight), 10 mg/mL P3HT and PCPDTBT *o*-dichlorobenzene solution without dopant, Spiro-OMeTAD (70 mM), FDT (100 M), and BTT-3 (30 mM) with Li-TFSI, FK209, and tBP (HTM : Li-TFSI : FK209 : tBP = 1 : 0.12 : 0.06 : 0.35 for weight), and CuSCN (150 mM) propylsulfide solution. P3HT, PCPDTBT, and CuSCN was spin-coated at 2000 rpm for 30 s, while the others were spin-coated at 4000 rpm for 30 s. Li-TFSI and tBP were not used for the $AgBiI_4$ and $AgSbI_4$ solar cells because of dopant-induced degradation. PTAA, P3HT, and PCPDTBT were annealed at 100 ℃ for 10 min. For optimized SbSI solar cell, PEDOT:PSS (Clevious AI 4083) mixed with DMF (PEDOT:PSS : DMF = 1 : 2) was spin-coated onto the HTM and annealed at 130 ℃ for 5 min. Finally, Au electrode was evaporated to form a thickness of 70 nm. The schematics of device structures and the statistics of device performance are provided in Figure 5-15, 5-16.

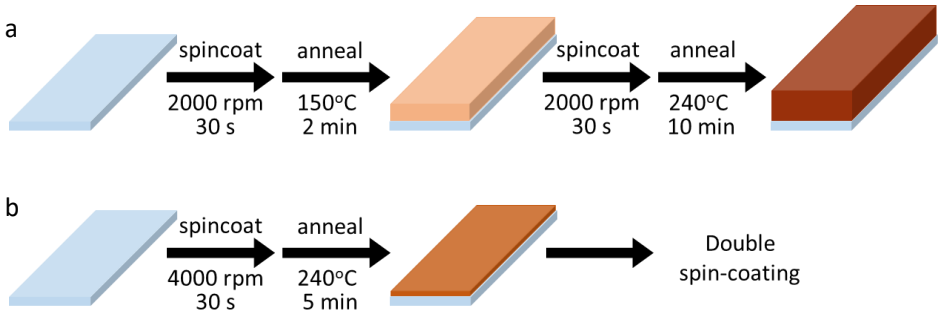

Figure 5-14. Schematic image of (a) double spin-coating and (b) pre-deposition of thin SbSI. The original precursor solution (SbI_3 0.4 M, $Sb(EtXa)_3$ 0.3 M) was diluted with DMSO; (a) precursor : DMSO = 1 : 0.5, (b) precursor : DMSO = 1 : 3. The detail is as follows: (a) the diluted solution was spin-coated onto the substrate (2000 rpm, 30 s), followed by annealing (150 ℃, 2 min). After cooling the substrate to room temperature, the precursor solution was spin-coated again (2000 rpm, 30 s), and annealed (240 ℃, 10 min). (b) The diluted solution was spin-coated (4000 rpm, 30 s) followed by annealing (240 ℃, 5 min). Then, SbSI was spin-coated again in the same manner with the process (a).

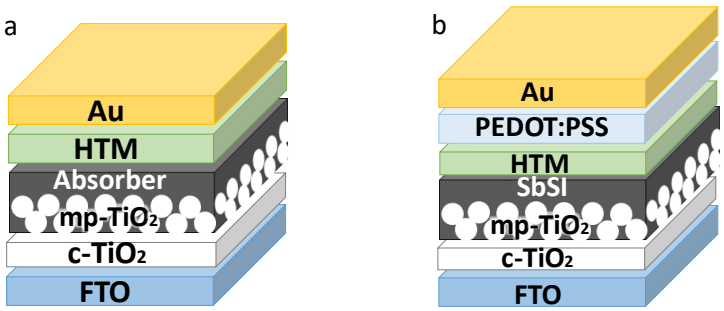

Figure 5-15. (a) Device structure used for the initial screening. (b) Optimized device structure of Sb_2S_3-containing SbSI device.

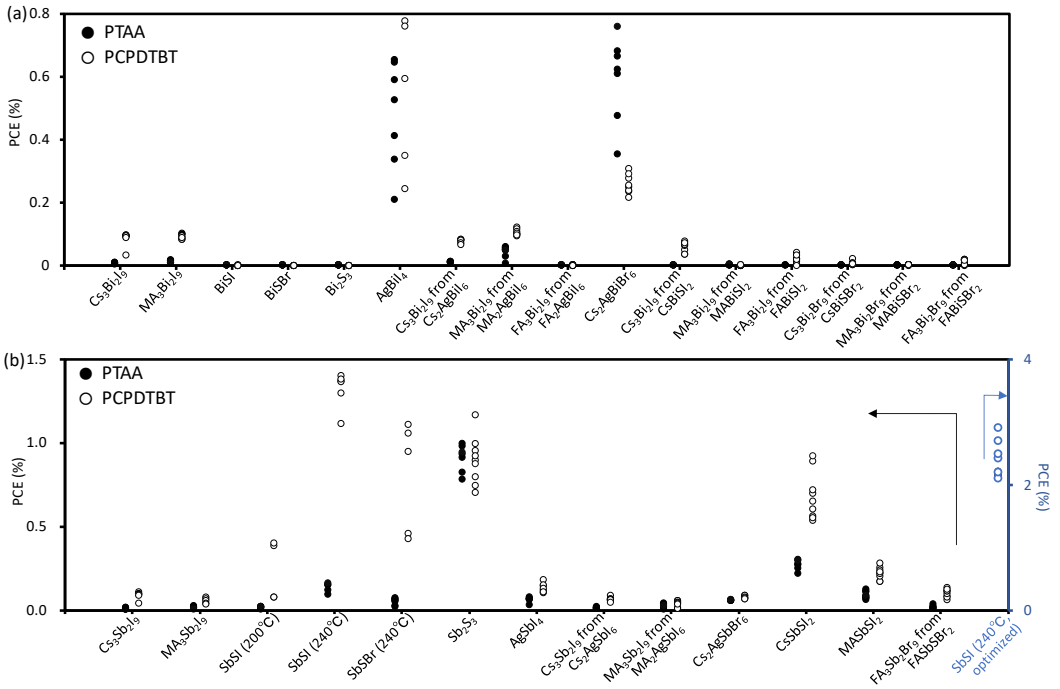

Figure 5-16. The statistics of solar cell performance of (a) Bi- and (b) Sb-based materials, which are corresponding to Table 4. The optimized Sb_2S_3-containing SbSI (at 240 °C), prepared by pre-deposition and double spin-coating, are described with blue circles in (b). For each device structure, 5~9 cells were measured.

5-5. Reference

[1] Park, B.-W.; Philippe, B.; Zhang, X.; Rensmo, H.; Boschloo, G.; Johansson, E. M. J. *Adv. Mater.* **2015**, *27*, 6806–6813.

[2] Shin, S. S.; Baena, J. P. C.; Kurchin, R. C.; Polizzotti, A.; Yoo, J. J.; Wieghold, S.; Bawendi, M. G.; Buonassisi, T. *Chem. Mater.* **2018**, *30*, 336–343.

[3] Boopathi, K. M.; Karuppuswamy, P.; Singh, A.; Hanmandlu, C.; Lin, L.; Abbas, S. A.; Chang, C. C.; Wang, P. C.; Li, G.; Chu, C. W. *J. Mater. Chem. A* **2017**, *5*, 20843–20850.

[4] Szklarz, P.; Jakubas, R.; Gagor, A.; Bator, G.; Cichos, J.; Karbowiak, M. *Inorg. Chem. Front.* **2020**, *7*, 1780–1789.

[5] Leng, M.; Chen, Z.; Yang, Y.; Li, Z.; Zeng, K.; Li, Z.; Niu, G.; He, Y.; Zhou, Q.; Tang, J. *Angew. Chem. Int. Ed.* **2016**, *55*, 15012–15016.

[6] Shen, Y.; Yin, J.; Cai, B.; Wang, Z.; Dong, Y.; Xu, X.; Zeng, H. Lead-Free, *Nanoscale Horizons* **2020**, *5*, 580–585.

[7] Yang, J.-M.; Choi, E.-S.; Kim, S.-Y.; Kim, J.-H.; Park, J.-H.; Park, N.-G. *Nanoscale* **2019**, *11*, 6453–6461.

[8] Li, T.; Wang, Q.; Nichol, G. S.; Morrison, C. A.; Han, H.; Hu, Y.; Robertson, N. *Dalt. Trans.* **2018**, *47*, 7050–7058.

[9] Nishikubo, R.; Saeki, A. *J. Photopolym. Sci. Technol.* **2019**, *32*, 735–740.

[10] Sansom, H. C.; Whitehead, G. F. S.; Dyer, M. S.; Zanella, M.; Manning, T. D.; Pitcher, M. J.; Whittles, T. J.; Dhanak, V. R.; Alaria, J.; Claridge, J. B.; Rosseinsky, M. J. *Chem. Mater.* **2017**, *29*, 1538–1549.

[11] Zhu, H.; Pan, M.; Johansson, M. B.; Johansson, E. M. J. *ChemSusChem* **2017**, *10*, 2592–2596.

[12] Zhang, Q.; Wu, C.; Qi, X.; Lv, F.; Zhang, Z.; Liu, Y.; Wang, S.; Qu, B.; Chen, Z.; Xiao, L. *ACS Appl. Energy Mater.* **2019**, *2*, 3651–3656.

[13] Abate, A. *Joule* **2017**, *1*, 659–664.

[14] Pantaler, M.; Cho, K. T.; Queloz, V. I. E.; García Benito, I.; Fettkenhauer, C.; Anusca, I.; Nazeeruddin, M. K.; Lupascu, D. C.; Grancini, G. *ACS Energy Lett.* **2018**, *3*, 1781–1786.

[15] Wei, F.; Deng, Z.; Sun, S.; Zhang, F.; Evans, D. M.; Kieslich, G.; Tominaka, S.; Carpenter, M. A.; Zhang, J.; Bristowe, P. D.; Cheetham, A. K. *Chem. Mater.* **2017**, *29*, 1089−1094.

[16] García-Espejo, G.; Rodríguez-Padrón, D.; Luque, R.; Camacho, L.; Miguel, G. *Nanoscale* **2019**, *11*, 16650–16657.

[17] Hahn, N. T.; Rettie, A. J. E.; Beal, S. K.; Fullon, R. R.; Mullins, C. B. *J. Phys. Chem. C* **2012**, *116*, 24878–24886.

[18] Peng, B.; Xu, K.; Zhang, H.; Ning, Z.; Shao, H.; Ni, G.; Li, J.; Zhu, Y.; Zhu, H.; Soukoulis, C. M. *Adv. Theory Simulations* **2018**, *1*, 1700005.

[19] Nie, R.; Yun, H. S.; Paik, M. J.; Mehta, A.; Park, B. W.; Choi, Y. C.; Seok, S. Il. *Adv. Energy Mater.* **2018**, *8*, 1701901.

[20] Nie, R.; Im, J.; Seok, S. Il. *Adv. Mater.* **2019**, *31*, 1808344.

[21] Sun, Y. Y.; Shi, J.; Lian, J.; Gao, W.; Agiorgousis, M. L.; Zhang, P.; Zhang, S. *Nanoscale* **2016**, *8*, 6284–6289.

[22] Nie, R.; Mehta, A.; Park, B. W.; Kwon, H. W.; Im, J.; Seok, S. Il. *J. Am. Chem. Soc.* **2018**, *140*, 872–875.

[23] Li, T.; Wang, X.; Yan, Y.; Mitzi, D. B. *J. Phys. Chem. Lett.* **2018**, *9*, 3829–3833.

[24] Martinez, L.; Bernechea, M.; De Arquer, F. P. G.; Konstantatos, G. *Adv. Energy Mater.* **2011**, *1*, 1029–1035.

[25] Chang, J. A.; Rhee, J. H.; Im, S. H.; Lee, Y. H.; Kim, H. J.; Seok, S. Il; Nazeeruddin, M. K.; Gratzel, M. *Nano Lett.* **2010**, *10*, 2609–2612.

[26] Tsujimoto, K.; Nguyen, D. C.; Ito, S.; Nishino, H.; Matsuyoshi, H.; Konno, A.; Kumara, G. R. A.; Tennakone, K. *J. Phys. Chem. C* **2012**, *116*, 13465–13471.

[27] Choi, Y. C.; Seok, S. Il. *Adv. Funct. Mater.* **2015**, *25*, 2892–2898.

[28] Saeki, A.; Koizumi, Y.; Aida, T.; Seki, S. *Acc. Chem. Res.* **2012**, *45*, 1193–1202.

[29] Yoshikawa, S.; Saeki, A.; Saito, M.; Osaka, I.; Seki, S. *Phys. Chem. Chem. Phys.* **2015**, *17*, 17778–17784.

[30] Ishida, N.; Wakamiya, A.; Saeki, A. *ACS Photonics* **2016**, *3*, 1678–1688.

[31] Nishikubo, R.; Saeki, A. *J. Phys. Chem. Lett.* **2018**, *9*, 5392–5399.

[32] Shannon, R. D. *Acta Cryst.* **1976**, *32*, 751–767.

[33] Dimesso, L.; Quintilla, A.; Kim, Y. M.; Lemmer, U.; Jaegermann, W. *Mater. Sci. Eng. B Solid-State Mater. Adv. Technol.* **2016**, *204*, 27–33.

[34] Maclachlan, A. J.; O'Mahony, F. T. F.; Sudlow, A. L.; Hill, M. S.; Molloy, K. C.; Nelson, J.; Haque, S. A. *ChemPhysChem* **2014**, *15*, 1019–1023.

[35] Hutter, E. M.; Gélvez-Rueda, M. C.; Osherov, A.; Bulović, V.; Grozema, F. C.; Stranks, S. D.; Savenije, T. J. *Nat. Mater.* **2017**, *16*, 115–120.

[36] Bernechea, M.; Cao, Y.; Konstantatos, G. *J. Mater. Chem. A* **2015**, *3*, 20642–20648.

[37] Oga, H.; Saeki, A.; Ogomi, Y.; Hayase, S.; Seki, S. *J. Am. Chem. Soc.* **2014**, *136*, 13818–13825.

[38] NREL Reference Air Mass 1.5 Spectra https://www.nrel.gov/grid/solar-resource/spectra-am1.5.html

[39] Saliba, M.; Orlandi, S.; Matsui, T.; Aghazada, S.; Cavazzini, M.; Correa-Baena, J. P.; Gao, P.; Scopelliti, R.; Mosconi, E.; Dahmen, K. H.; De Angelis, F.; Abate, A.; Hagfeldt, A.; Pozzi, G.; Graetzel, M.; Nazeeruddin, M. K. *Nat. Energy* **2016**, *1*, 15017.

[40] García-Benito, I.; Zimmermann, I.; Urieta-Mora, J.; Aragó, J.; Molina-Ontoria, A.; Ortí, E.; Martín, N.; Nazeeruddin, M. K. *J. Mater. Chem. A* **2017**, *5*, 8317–8324.

[41] Madhavan, V. E.; Zimmermann, I.; Baloch, A. A. B.; Manekkathodi, A.; Belaidi, A.; Tabet, N.; Nazeeruddin, M. K. *ACS Appl. Energy Mater.* **2020**, *3*, 114–121.

[42] Im, S. H.; Lim, C. S.; Chang, J. A.; Lee, Y. H.; Maiti, N.; Kim, H. J.; Nazeeruddin, M. K.; Grätzel, M.; Seok, S. Il. *Nano Lett.* **2011**, *11*, 4789–4793.

Chapter6: Conclusion of this Dissertation

In this dissertation, the author investigated the mechanism of molecular-induced transformation of LHPs and THPs and developed Bi- and Sb-based materials for optoelectronic application. The effect of oxygen exposure to THP and the detail of LCST behavior of LHP nanoparticles with the addition of CH_3NH_2 were elucidated. Consequently, motivated by the toxicity and the low stability of these materials, various Bi- and Sb-based semiconducting materials were studied as an alternative. The conclusion of these works are as follows.

Chapter 2

The details of molecular-induced transformation of LHP and THP were elucidated. For THP, the effect of air exposure and SnF_2 addition on the electrochemical and optoelectronic properties were investigated. PYS revealed the rapid deepening of VBM level. Whereas, SnF_2 addition suppressed the initial trap formation in $FASnI_3$. TRMC revealed the significant decrease of $\phi\Sigma\mu$ for all the samples. The temporal increase of $\phi\Sigma\mu$ in $MASnI_3$ is explained by the formation of MA_2SnI_6 phase, which has higher mobility and deeper VBM. These results provide the insights into the kinetics of degradation and the compositional effect on optoelectronics.

For LHP, the anomalous LCST behavior was observed in $MAPbBr_3$ nanoparticle colloidal solution with the addition of CH_3NH_2. Based on the control experiment of solution composition, temperature-dependent UV-vis, and single crystal XRD analysis, the transformation mechanism was revealed. This LCST system suggests a new application of halide perovskites as thermoresponsive photonic materials.

Chapter 3

Considering the toxicity and limited stability of LHPs and THPs, the author focused on Bi_2S_3 with extremely high photoconductivity. To obtain high quality thin film, CASC process consisting of facial spin-coating, prethermal annealing, and subsequent crystallization was developed. This process yielded a highly crystallized and pure Bi_2S_3 thin film, with the increased $\phi\Sigma\mu_{max}$ (1.3 $cm^2\ V^{-1}\ s^{-1}$) value. Temperature-dependent TRMC and TPC revealed band-like transport property at room temperature. The CASC-Bi_2S_3 photoresistor demonstrated much higher on/off ratio (~460) and detectivity (10^{11} Jones) than other films prepared by reported process, indicating high applicability of CASC process for metal sulfide-based optoelectronic devices.

Chapter 4

Comparative study of Bi-based dimer ($A_3Bi_2I_9$, A = Cs, MA, FA) and DP ($Cs_2AgBiBr_6$) were conducted by using TRMC. DP single layer showed a relatively high TRMC signal owing to the higher electron and hole mobility. The results of *n*/*i* and *n*/*i*/*p* layer of DP suggests more efficient electron transfer to TiO_2 and higher hole mobility than those of DMs. However, the electron and hole transfer to ETM and HTM were still insufficient, resulting in low current density (1.2 mA cm^{-2}) and PCE (0.72%). This result suggested the requirement for searching other absorbers with higher charge transport property.

Chapter 5

The author conducted a comprehensive survey on 44 different compositions of Bi- and Sb-based solar absorbers, through the evaluation of crystal phase formation (XRD), bandgap (UV-vis), VBM (PYS), and charge transfer (TRMC). Importantly, Sb-based materials including SbSX, Sb_2S_3, and SAP showed efficient electron transfer to mp-TiO_2. This result suggests the high possibility of Sb-based solar absorbers. J_{SC}–J_{SC_max} analysis revealed that internal charge separation and transport property predominate the current density rather than photoabsorption. Consequently, Sb_2S_3-containing SbSI prepared by new solution process exhibited the highest $\Delta\sigma_{max}$ and PCE among the candidates. The author also explored various HTMs for Sb_2S_3-containing SbSI, and found the inclusion of thiophene unit in HTM greatly impact the PCE. These findings provide the key strategy for further development of Bi- and Sb-based solar cells.

Thereafter, this study provides the insight into the mechanism of molecular-induced transformation of LHP and THP, and the optoelectronic properties of various Bi- and Sb-based semiconducting materials. The author hopes this study will contribute to the development of new application of LHP, the improvement of THP solar cells, and the exploration of Bi- and Sb-based solar absorbers.

List of Publications

1. Thermoresponsive Emission Switching via Lower Critical Solution Temperature Behavior of Organic-Inorganic Perovskite Nanoparticles
Ryosuke Nishikubo, Norimitsu Tohnai, Ichiro Hisaki, and Akinori Saeki*
Adv. Mater. **2017**, *29 (23)*, 1700047.

2. Minute-Scale Degradation and Shift of Valence-Band Maxima of $(CH_3NH_3)SnI_3$ and $HC(NH_2)_2SnI_3$ Perovskites upon Air Exposure
Ryosuke Nishikubo, Naoki Ishida, Yukie Katsuki, Atsushi Wakamiya, and Akinori Saeki*
J. Phys. Chem. C **2017**, *121 (36)*, 19650–19656.

3. Solution-Processed Bi_2S_3 Photoresistor Film To Mitigate a Trade-off between Morphology and Electronic Properties
Ryosuke Nishikubo and Akinori Saeki*
J. Phys. Chem. Lett. **2018**, *9 (18)*, 5392–5399.

4. Comparative Study of Charge Carrier Dynamics in Bismuth-based Dimer and Double Perovskites
Ryosuke Nishikubo and Akinori Saeki*
J. Photopolym. Sci. Technol. **2019**, *32 (5)*, 735–740.

5. Optoelectronic and Energy Level Exploration of Bismuth and Antimony-Based Materials for Lead-Free Solar Cells
Ryosuke Nishikubo, Hiroyuki Kanda, Inés García-Benito, Agustín Molina-Ontoria, Gianluca Pozzi, Abdullah M. Asiri, Mohammad Khaja Nazeeruddin*, and Akinori Saeki*
Chem. Mater. **2020**, *32 (15)*, 6416–6424.

List of Supplementary Publications

6. High-Performance Long-Term-Stable Dopant-Free Perovskite Solar Cells and Additive-Free Organic Solar Cells by Employing Newly Designed Multirole π-Conjugated Polymers
Kakaraparthi Kranthiraja, Kumarasamy Gunasekar, Hyunji Kim, An-Na Cho, Nam-Gyu Park, Seonha Kim, Bumjoon J. Kim, **Ryosuke Nishikubo**, Akinori Saeki*, Myungkwan Song*, and Sung-Ho Jin*
Adv. Mater. **2017**, *29 (23)*, 1700183.

7. Solvent-Coordinated Tin Halide Complexes as Purified Precursors for Tin-Based Perovskites
Masashi Ozaki, Yukie Katsuki, Jiewei Liu, Taketo Handa, **Ryosuke Nishikubo**, Shinya Yakumaru, Yoshifumi Hashikawa, Yasujiro Murata, Takashi Saito, Yuichi Shimakawa, Yoshihiko Kanemitsu, Akinori Saeki, and Atsushi Wakamiya*
ACS Omega **2017**, *2 (10)*, 7016–7021.

8. Accomplishment of Multifunctional π-Conjugated Polymers by Regulating the Degree of Side-Chain Fluorination for Efficient Dopant-Free Ambient-Stable Perovskite Solar Cells and Organic Solar Cells
Kakaraparthi Kranthiraja, Sang Ho Park, Hyunji Kim, Kumarasamy Gunasekar, Gibok Han, Bumjoon J. Kim, Chang Su Kim, Soohyun Kim, Hyunjung Lee*, **Ryosuke Nishikubo**, Akinori Saeki*, Sung-Ho Jin*, and Myungkwan Song*
ACS Appl. Mater. Interfaces **2017**, *9 (41)*, 36053–36060.

9. Highly efficient air-stable/hysteresis-free flexible inverted-type planar perovskite and organic solar cells employing a small molecular organic hole transporting material
Saripally Sudhaker Reddy, Sungmin Shin, Um Kanta Aryal, **Ryosuke Nishikubo**, Akinori Saeki*, Myungkwan Song*, and Sung-Ho Jin*
Nano Energy **2017**, *41*, 10–17.

10. Lithium-Ion Endohedral Fullerene (Li+@C60) Dopants in Stable Perovskite Solar Cells Induce Instant Doping and Anti-Oxidation
Il Jeon, Hiroshi Ueno, Seungju Seo, Kerttu Aitola, **Ryosuke Nishikubo**, Akinori Saeki, Hiroshi Okada, Gerrit Boschloo, Shigeo Maruyama, and Yutaka Matsuo*
Angew. Chem. Int. Ed. **2018**, *57 (17)*, 4607–4611.

11. Photon Upconversion through a Cascade Process of Two-Photon Absorption in $CsPbBr_3$ and Triplet–Triplet Annihilation in Porphyrin/Diphenylanthracene
Shogo Izakura, Wenting Gu, **Ryosuke Nishikubo**, and Akinori Saeki*
J. Phys. Chem. C **2018**, *122 (26)*, 14425–14433.

12. Anomalous Dielectric Behavior of a Pb/Sn Perovskite: Effect of Trapped Charges on Complex Photoconductivity
Kento Yamada, **Ryosuke Nishikubo**, Hikaru Oga, Yuhei Ogomi, Shuzi Hayase, Shohei Kanno, Yutaka Imamura, Masahiko Hada, and Akinori Saeki*
ACS Photonics **2018**, *5 (8)*, 3189–3197.

13. Lead-Free Solar Cells based on Tin Halide Perovskite Films with High Coverage and Improved Aggregation
Jiewei Liu, Masashi Ozaki, Shinya Yakumaru, Taketo Handa, **Ryosuke Nishikubo**, Yoshihiko Kanemitsu, Akinori Saeki, Yasujiro Murata, RichardMurdey, and Atsushi Wakamiya*
Angew. Chem. Int. Ed. **2018**, *57 (40)*, 13221–13225.

14. Semiconducting carbon nanotubes as crystal growth templates and grain bridges in perovskite solar cells
Seungju Seo, Il Jeon*, Rong Xiang, Changsoo Lee, Hao Zhang, Takeshi Tanaka, Jin-Wook Lee, Donguk Suh, Tatsuro Ogamoto, **Ryosuke Nishikubo**, Akinori Saeki, Shohei Chiashi, Junichiro Shiomi, Hiromichi Kataura, Hyuck Mo Lee, Yang Yang, Yutaka Matsuo*, and Shigeo Maruyama*
J. Mater. Chem. A **2019**, *7 (21)*, 12987–12992.

15. Molecular Orientation Change in Naphthalene Diimide Thin Films Induced by Removal of Thermally Cleavable Substituents
Tomoya Nakamura, Nobutaka Shioya, Takafumi Shimoaka, **Ryosuke Nishikubo**, Takeshi Hasegawa*, Akinori Saeki, Yasujiro Murata, Richard Murdey, and Atsushi Wakamiya*
Chem. Mater. **2019**, *31 (5)*, 1729–1737.

16. How the Mixed Cations (Guanidium, Formamidinium, and Phenylethylamine) in Tin Iodide Perovskites Affect Their Charge Carrier Dynamics and Solar Cell Characteristics
Eita Nakanishi, **Ryosuke Nishikubo**, Atsushi Wakamiya, and Akinori Saeki*
J. Phys. Chem. Lett. **2020**, *11 (10)*, 4043–4051.

17. Coordination of NH_2- or COOH-Appended Pt-Porphyrins with $CsPbBr_3$ Perovskite Quantum Dots to Improve a Cascade Process of Two-Photon Absorption and Triplet–Triplet Annihilation
Wenting Gu, **Ryosuke Nishikubo**, and Akinori Saeki*
J. Phys. Chem. C **2020**, *124 (27)*, 14439–14445.

18. Anisotropic Photoconductivity and Long-Lived Charge Carriers in Bismuth-Based One-Dimensional Perovskite with Type-IIa Band Alignment
Johnpaul K. Pious, Manasa G. Basavarajappa, Chinnadurai Muthu, Nayana Krishna, **Ryosuke Nishikubo**, Akinori Saeki, Sudip Chakraborty*, and Vijayakumar C. Nair*
J. Phys. Chem. Lett. **2020**, *11 (16)*, 6757–6762.

19. Ag-(Bi, Sb, In, Ga)-I Solar Cells: Impacts of Elemental Composition and Additives on the Charge Carrier Dynamics and Crystal Structures
Fumiya Iyoda, **Ryosuke Nishikubo**, Atsushi Wakamiya, and Akinori Saeki*
ACS Appl. Energy Mater. **2020**, *3 (9)*, 8224–8232.

20. High Current Density Sn-Based Perovskite Solar Cells via Enhanced Electron Extraction in Nanoporous Electron-Transport Layers
Yumi Miyamoto*, Shohei Kusumoto, Tomoyasu Yokoyama, Yu Nishitani, Taisuke Matsui, Takeshi Kouzaki, **Ryosuke Nishikubo**, Akinori Saeki, Yukihiro Kaneko
ACS Appl. Nano Mater. **2020**, *3 (11)*, 11650–11657.

Acknowledgement

The study presented in this dissertation was carried out under the direction of Professor Akinori Saeki at the Department of Applied Chemistry, Graduate School of Engineering, Osaka University.

This study was supported by many people. Foremost, the author wishes to express his sincerest gratitude to Professor Akinori Saeki for his insightful suggestion, valuable discussions, teaching, encouragement, and extensive supports throughout this work. Under his direction, the author got the great chance to proceed his work on the way he desired, along with acquiring the important knowledge and skills. The author wishes his deep gratitude to Associate Professor Fumitaka Ishiwari at the Department of Applied Chemistry, Graduate School of Engineering, Osaka University for his insightful suggestions, valuable discussions, teaching, encouragement, and many supports.

The author would like to give heartfelt thanks to Professor Mohammad Khaja Nazeeruddin at École polytechnique fédérale de Lausanne (EPFL), Switzerland for giving a precious opportunity to work in his exciting research group from September to December, 2019. The author is grateful to Dr. Hiroyuki Kanda at EPFL for his insightful suggestion, and many supports during stay. He is also grateful to other Nazeeruddin group members for their kind assistance and warm friendship throughout the stay.

The author expresses his sincere thanks to Professor Susumu Kuwabata and Professor Ken-ichi Nakayama at the Department of Applied Chemistry, Graduate School of Engineering, Osaka University, for reviewing this dissertation and providing critical comments.

The author expresses his sincere thanks to the following people for their assistance with sample preparation, measurement, analysis, and device fabrication throughout his doctoral research:

- Professor Norimitsu Tohnai at the Department of Applied Chemistry, Graduate School of Engineering, Osaka University and Professor Ichiro Hisaki at the Department of Chemical Science and Engineering, Graduate School of Engineering Science, Osaka University for single crystal XRD measurement.
- Professor Atsushi Wakamiya and Ms. Yukie Katsuki at Kyoto University for

providing Sn perovskite sample and showing the preparation method.

- Professor Itaru Osaka and Assistant Professor Masahiko Saito at Hiroshima University and Dr. Tomoyuki Koganezawa at Japan Synchrotron Radiation Research Institute (JASRI) for 2D-GIXRD measurements.
- Dr. Inés García-Benito at Universidad Complutense de Madrid, Dr. Agustín Molina-Ontoria at IMDEA-Nanociencia, Dr. Gianluca Pozzi at Italian National Research Council, and Professor Abdullah M. Asiri at King Abdulaziz University for giving the opportunity of corroboration for the development of Bi- and Sb-based solar cells.

Warm thanks to all Saeki laboratry members, Dr. Kakaraparthi Kranthiraja, Ms. Karin Fujino, Mr. Shaoxian Li, Ms. Mayuka Nomura, Mr. Fumiya Hamada, Ms. Chinatsu Sakura, Mr. Eita Nakanishi, Mr. Yuta Miyake, Mr. Yoshiyuki Murakami, Mr. Kazuki Omote, Mr. Rei Shimono, Ms. Chisato Nishikawa, Ms. Sayuri Miyake, Mr. Kazuharu Murotani, Dr. Hajime Suzuki, Dr. Marina Ide, Dr. Eman Rashid Said Al-Naamani, Mr. Hikaru Oga, Mr. Masataka Kumano, Mr. Naoki Ishida, Mr. Yoshiki Shimata, Mr. Shinji Nagasawa, Mr. Frank Elias Caraballo Hidalgo, Mr. Yihe Miao, Mr. Kento Yamada, Mr. Kenta Aoshima, Ms. Misuzu Kita, Mr. Shogo Izakura, Mr. Fumiya Iyoda, Ms. Wenting Gu, Ms. Pimpisut Worakajit, and Ms. Jidapa Chaopaknam.

The author acknowledges financial support from Japan Society for the Promotion of Science (JSPS) scholarship (No. 201820108) and JSPS Overseas Challenge Program for Young Researchers during his Ph.D course.

Finally, the author is thankful for his parents Mr. Tadahiro Nishikubo, Ms. Junko Nishikubo, and his younger brother Mr. Naruki Nishikubo for their continuous support and encouragement.

Ryosuke Nishikubo

Department of Applied Chemistry
Graduate School of Engineering
Osaka University
2021